

Investigation of Carbon Nanotube Quantum Dots Connected to Ferromagnetic Leads

Inauguraldissertation

zur
Erlangung der Würde eines Doktors der Philosophie
vorgelegt der
Philosophisch-Naturwissenschaftlichen Fakultät
der Universität Basel

VON

Julia Samm
aus Aachen, Deutschland



Basel, 2015
Originaldokument gespeichert auf dem Dokumentenserver der
Universität Basel
edoc.unibas.ch

Genehmigt von der Philosophisch-Naturwissenschaftlichen Fakultät
auf Antrag von
Prof. Dr. C. Schönenberger
Prof. Dr. C. Strunk
Prof. Dr. B. Hickey

Basel, 24.06.2014

Prof. Dr. Jörg Schibler
Dekan

CONTENTS

| | |
|--|-----------|
| Contents | 1 |
| 1 Introduction | 3 |
| 2 Theoretical Background | 5 |
| 2.1 Conventional Spin Valve | 5 |
| 2.2 Carbon Nanotube Quantum Dots | 13 |
| 2.3 Spintransport in CNT Quantum Dots | 22 |
| 3 Basics of Device Fabrication and Experimental Set-up | 29 |
| 3.1 Sample Fabrication | 29 |
| 3.2 Measurement Set-Up | 33 |
| 4 The origin of instabilities in MR measurements | 35 |
| 4.1 The Necessity for an Extended MR Measurement Scheme | 36 |
| 4.2 Optimized E-Beam Lithography | 41 |
| 4.3 MR Measurements on Devices with Sputtered Py Strips | 44 |
| 4.4 Optimized UHV Magnetron Sputter Deposition | 49 |
| 5 MR Experiments on Stable Devices | 55 |
| 5.1 Negative Magneto Resistance over Set of Four Coulomb Peaks | 55 |
| 5.2 Stability Diagrams for Different Magnetic Configurations | 63 |
| 5.3 Indications for a MR depended on the Occupation of the QD | 68 |
| 6 Beyond collinear MR measurements | 71 |
| 7 Summary | 73 |
| Bibliography | 75 |
| A Fabrication Recipes | 85 |
| B Additional Data to chapter 5.1 | 89 |
| C Additional Data to chapter 5.2 | 91 |
| D Additional Data to chapter 5.3 | 93 |
| Curriculum Vitae | 95 |
| Publications | 97 |

CHAPTER 1

INTRODUCTION

* * *

The implementation of ferromagnetic contacts in complex nanoelectronic devices, e.g. in spin-valves bears great potential for applications and fundamental investigations. Spin-valves are structures with two magnetic contacts and a non-magnetic medium (M) in-between, where a step-like change in magnetoresistance (MR) is observed when the relative orientation of the strip magnetization is changed by an external magnetic field. There is already a very successful use of the electron spin in electronic devices for magnetic field sensing for example in read-and-write heads of computer hard discs. Another upcoming application of spin valves are for example non-volatile random-access memories (MRAMs) for data storage.

However, electronic devices which use the electron spin directly, like in a spin-transistor [1] or as quantum bits [2] requires materials for the non-magnetic medium exhibiting long coherence times and electrical tunability. Carbon based materials like graphene or carbon nanotubes are due to their intrinsic large coherence times in principle ideal candidates for spintronic devices, as demonstrated in nonlocal spin-accumulation experiments on graphene[3] or in electrically tunable spin valves on carbon nanotubes. [4, 5]

Especially the observation of a gate dependent magneto-resistance in carbon nanotube quantum dots contacted with ferromagnetic leads in 2005 by S. Sahoo [4] promises an electrical control over spin transport. These devices analog to field-effect transistors might pave the way for multi-functional spintronic devices. However, the implementation of ferromagnetic contacts in nanoelectronic devices has been a proven challenging task due to the complex nature of ferromagnets and interfaces, where oxidation, surface roughness and mesoscopic details may induce uncontrolled instabilities in transport measurements.

Spintransport experiments on carbon nanotube quantum dots suffer mainly from irreproducibilities in the magneto resistance and from the low yield of electrical contacts to the nanotube. Therefore in this thesis carbon nanotube quantum dots connected to ferromagnetic leads are investigated, focusing on the fabrication of stable devices with higher contact yields and first experiments on stable devices. This allows for further investigations of the not well understood gate dependence of the magneto resistance in such devices. Moreover with such stable devices, even more complex experiments or applications

like detectors for spin entanglement can become possible [6].

This thesis is organized as follows.

- **Chapter 2** introduces the theoretical background, starting with conventional spin valves followed by the basics of carbon nanotubes and quantum dots before going on with spin transport on carbon nanotube quantum dots.
- **Chapter 3** presents the basics about the sample fabrication and describes the experimental set-up.
- **Chapter 4** reports an improved fabrication process and motivates the necessity for an extended measurement scheme.
- **Chapter 5** show magneto resistance experiments on carbon nanotube quantum dots exhibiting a clear four-fold conductance pattern consistent with the spin and orbital degeneracy of a carbon nanotube. In addition preliminary results on energy stability diagrams for different magnetic orientations are presented.
- **Chapter 6** shows first test devices for non-collinear magneto resistance measurements.
- **Chapter 7** summarizes the results of this thesis and give suggestions for further experiments.

THEORETICAL BACKGROUND

* * *

Spin transport through carbon nanotube (CNT) quantum dots merges two independent topics: spin valves and quantum dots. This chapter discusses the fundamental mechanisms which are relevant for electron transport in such complex nano-electronic devices. The theoretical concepts of conventional spin valves and of CNT quantum dots will be introduced consecutively, before the more complex theory of spin transport in CNT quantum dots is introduced in the last part of this chapter

2.1 Conventional Spin Valve

A conventional vertical spin valve consists of two ferromagnetic (F) layers separated by a non-magnetic (N) spacing layer, see fig.2.1a. The relative magnetic orientation of the F layers lead to two electrical conductances G when a current is driven perpendicular to this sandwich structure. To set the relative orientation by an external magnetic field, different coercive fields B_c are needed. The free layer, with smaller B_c , changes its magnetization orientation at lower external magnetic fields than the pinned layer with higher B_c . A schematic of the conductance versus external magnetic field is depicted in fig.2.1b. A step like change in the conductance occurs when the magnetization changes from parallel to anti-parallel alignment and vice versa. The normalized difference between the conductance in the parallel, G_P , and the anti-parallel case, G_{AP} , is called magneto-resistance (MR)¹ and defined as:

$$MR = \frac{G_P - G_{AP}}{G_P + G_{AP}} \quad (2.1)$$

The origin of these two conductances can be found primarily on a population imbalance between the spin-subbands in a Stoner-ferromagnet and in addition on the choice of the spacing layer material (e.g an insulating or conducting material).

In the Stoner-model of a ferromagnet the band structure is supposed to be separated in two subbands, one for spin up electrons and one for spin down [7]. Considering the ferromagnetic ordering these two subbands are split due to exchange interactions of the electrons which shifts the band with respect to each other by the exchange energy ΔE_{ex} . As a result the densities of states

¹Other definitions of the MR can be found in literature. See chapter 2.3 for the rationale of this choice.

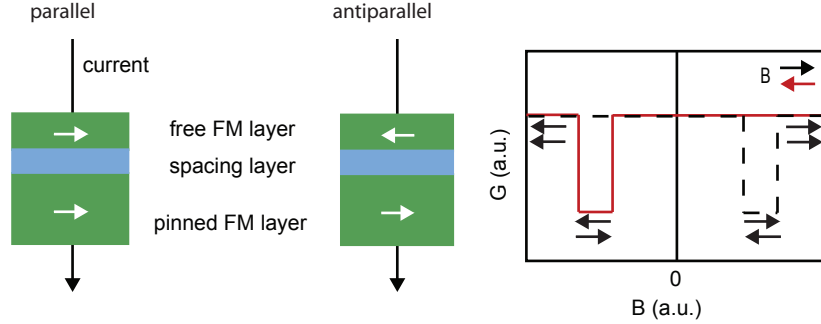


Figure 2.1: a) Schematic of a conventional spin valve: two F layers are separated by a non-magnetic spacing layer. Depending on the relative magnetization of these two layers, two conductance conductances can be obtained. b) Conductance G vs external magnetic field B

(DOS) at the Fermi-level E_F are not equal for spin up $N_{\uparrow}(E)$ and spin down $N_{\downarrow}(E)$ electrons (see e.g. fig.2.2 left), which leads to a spin polarization P of the conduction electrons at the Fermi-level:

$$P = \frac{N_{\uparrow}(E_F) - N_{\downarrow}(E_F)}{N_{\uparrow}(E_F) + N_{\downarrow}(E_F)}. \quad (2.2)$$

A direct consequence of this spin polarization is that a current \vec{j} driven through a ferromagnet is spin polarized, too. In the two-current-model, theoretically proposed by Mott [8] and experimentally verified by Fert and Campbell [9, 10], the total current \vec{j} can be decomposed into two independent currents $\vec{j}_{\uparrow}, \vec{j}_{\downarrow}$ for each spin species. The spin polarization can then be rewritten as

$$P_{\vec{j}} = \frac{\vec{j}_{\uparrow} - \vec{j}_{\downarrow}}{\vec{j}_{\uparrow} + \vec{j}_{\downarrow}}. \quad (2.3)$$

In addition to the spin polarization as a basic requirement, the choice of the spacing layer material plays an important role as well for the fundamental mechanism leading to magneto-resistance. In particular, one has to distinguish between an insulating and a conducting material. However, due to the different underlying mechanisms the corresponding magneto-resistance effects are called more specific: tunnel magneto-resistance (TMR) for insulating spacing layers and giant magneto-resistance (GMR) for conducting ones. The following will explain TMR and GMR, respectively.

Tunnel Magneto Resistance

A typical tunnel magneto-resistance device consists of a ferromagnetic-insulator-ferromagnetic (F/I/F) sandwich structure. In such magnetic tunnel junctions (MTJ) the electron transport is dominated by tunneling processes. According to the simple model by Jullière [11] and considering the two current model,

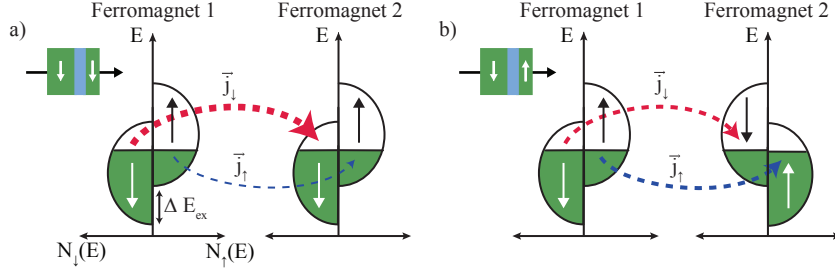


Figure 2.2: Schematic of the tunnel magneto-resistance according to the Jullières model. The density of states for spin up $N_{\uparrow}(E)$ and spin down $N_{\downarrow}(E)$ are representative depicted for the Stoner ferromagnets. Since the tunneling current in each spin channel is proportional to the density of states a higher conductance is expected for a) the parallel alignment than for b) the antiparallel alignment.

the conductance in each spin channel is proportional to the density of states at the corresponding Fermi-level. In the linear response regime the conductance in the parallel G_P and the antiparallel G_{AP} magnetic configuration is then given by

$$G_P \propto N_{\uparrow}^1(E_F)N_{\uparrow}^2(E_F) + N_{\downarrow}^1(E_F)N_{\downarrow}^2(E_F), \quad (2.4)$$

$$G_{AP} \propto N_{\uparrow}^1(E_F)N_{\downarrow}^2(E_F) + N_{\downarrow}^1(E_F)N_{\uparrow}^2(E_F),$$

including the assumption that the spin of the electron is conserved during the tunneling process. The indices 1, 2 correspond to the two ferromagnetic layers.

With the definition of the MR eq.2.1 and eq.2.4, the tunnel magneto-resistance can be expressed as:

$$TMR = \frac{G_P - G_{AP}}{G_P + G_{AP}} = \frac{N_{\uparrow}^1 N_{\uparrow}^2 + N_{\downarrow}^1 N_{\downarrow}^2 - N_{\uparrow}^1 N_{\downarrow}^2 - N_{\downarrow}^1 N_{\uparrow}^2}{N_{\uparrow}^1 N_{\uparrow}^2 + N_{\downarrow}^1 N_{\downarrow}^2 + N_{\uparrow}^1 N_{\downarrow}^2 + N_{\downarrow}^1 N_{\uparrow}^2} \quad (2.5)$$

By using the definition of the polarization in eq. 2.2 this can be simplified to:

$$TMR = P_1 P_2 \quad (2.6)$$

A schematic of the tunnel currents from one ferromagnet to another is given in fig.2.2. Here the ferromagnets are represented by the DOS $N_{\uparrow}, N_{\downarrow}$ and the current is depicted as dotted lines ². In the parallel case (fig.2.2a), many majority-spins \downarrow of the first F_1 are accepted by many empty states in the second F_2 . A high conductance for the majority-spin electrons is the result. This is in contrast to the situation of the minority-spins \uparrow . In the antiparallel

²The thickness of these lines corresponds to the value of the current.

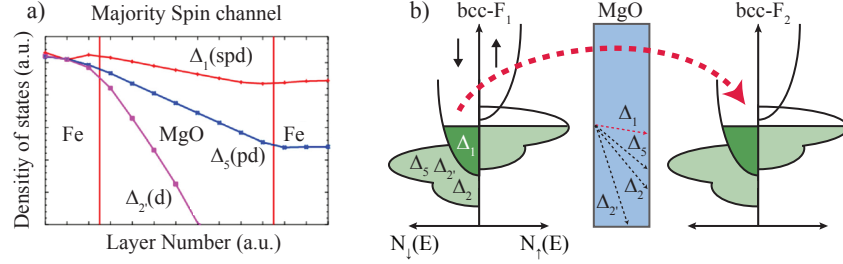
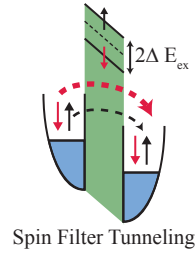


Figure 2.3: a) Calculated density of states of the majority spin channel for a Fe/MgO/Fe tunnel junction. Bloch states of different symmetries decay with varying rates in the tunnel barrier. b) Extended MTJ scheme for a symmetry filtering tunnel barrier in contrast to a simple energy barrier like in fig.2.2. (adapted from [18, 17])

case (fig.2.2b) majority and minority-spins are reversed in the second F_2 . Now majority-spins have to tunnel to empty minority-spin states and vice versa. Therefore the current in the spin \uparrow channel is equal to the current in the spin \downarrow channel. In total, a higher conductance is observed for the parallel alignment than for the antiparallel one.

Jullières model is quite sufficient to explain the spin dependent tunneling process for incoherent tunneling, applicable for example to amorphous tunnel barriers like Al_2O_3 [12, 13]. The predicted and measured TMR values for tunnel junctions with amorphous tunnel barriers correspond well. For the large TMR values obtained in epitaxial junctions with, e.g., single crystalline MgO tunnel barriers [14, 15], this model collapses. For a crystalline barrier the electron transport is based on coherent tunneling and the two ferromagnetic electrodes can no longer be considered as independent from each other. Indeed, the F/I/F sandwich has to be treated as one system due to the overlap of the electron wave-functions in both ferromagnetic electrodes. In particular, evanescent wave functions in the MgO barrier couple to Bloch functions in the ferromagnets of the same symmetry. The high TMR values are then obtained due to the symmetry selection of the tunneling wavefunction. Typical Bloch states available in 3d transition metals along the (100) direction are $\Delta_1(\text{spd})$, $\Delta_2(\text{d})$, $\Delta_2'(\text{d})$ and $\Delta_5(\text{p,d})$. Especially in certain metals with bcc structure like Fe, Co and FeCo, the Δ_1 state exists only in their majority spin channel but not in their minority one. As an example, the calculated DOS of the majority spin channel for a Fe/MgO/Fe tunnel junction in parallel configuration is shown in fig.2.3a. The different Bloch states decay with varying rates in the tunnel barrier due to the symmetry matching of the wave functions between the barrier and the electrodes. Since the conductance is dominated by Δ_1 electrons, very high TMR values are expected [16, 17]. However, these first-principles theories predict considerably larger TMR values than measured so far. This is because scattering processes at a real F/I interface have also to be taken into account.

Figure 2.4: The conductance band of the tunnel barrier is exchange split, which results in different tunnel probabilities for each spin species [18]



Spin Filter Tunneling

A different kind of MTJ has to be mentioned: spin filter tunnel junctions. In these devices a ferro-/ferrimagnetic insulator separates two nonmagnetic electrodes from each other and the total conductance is determined by the tunnel probability for each spin species. In such tunnel barriers the conductance band is exchange split and different barrier heights for the spin-up and spin-down electrons are the result (see fig.2.4). Commonly used spin filter materials are europium chalcogenides (EuO, EuS, EuSe)[19, 20] and ferrites (CoFe₂O₄, NiFe₂O₄, Fe₃O₄, γ-Fe₂O₃) [21, 22, 23]. For later use it is stressed here that NiFe₂O₄ and γ-Fe₂O₃ forms the dominant natural oxides on the surface of Permalloy (Ni₈₀Fe₂₀) when exposed to air [24]. It is important to keep this in mind since in this thesis Permalloy (Py) is used as ferromagnetic electrodes for spin transport experiments.

Giant Magneto Resistance

Replacing the tunnel barrier in MTJs by a conducting material, e.g., Cr, Cu or Ru, leads to the giant magneto-resistance (GMR), discovered in 1988 by Peter Grünberg and Albert Fert [25, 26] and awarded with the Nobel prize in 2007. Two types of GMR-devices exist: the "current in plane" (CIP) and the "current perpendicular to the plane (CPP)" geometry. In both cases the underlying physical mechanism to observe GMR is based on spin-dependent scattering rates in the ferromagnetic contacts, schematically illustrated in fig. 2.5. Considering the two-current model and using the Drude formula for free electrons, a simple expression for the conductivity $\sigma_{\uparrow,\downarrow}$ in each spin-channel can be found

$$\sigma_{\uparrow,\downarrow} = \frac{e^2 n_{\uparrow,\downarrow} \tau_{\uparrow,\downarrow}}{m^*}, \quad (2.7)$$

where e is the electron charge, n the conduction electron density, τ the electron momentum relaxation time for the two spin species and m^* the mass of the electrons. This expression is only valid for free electrons, but it is useful

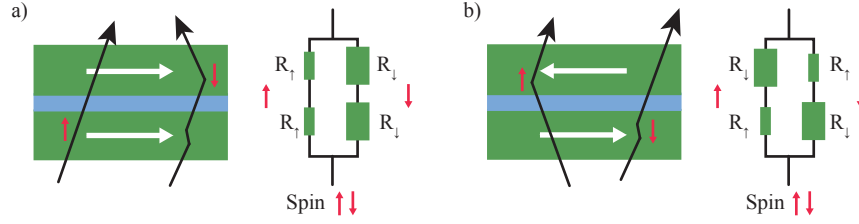


Figure 2.5: Schematic illustration of the mechanism of GMR. Spin-dependent scattering rates in the ferromagnets cause different conductivities for majority- and minority spin channel. a) Parallel configuration: scattering takes only place in one spin channel leading to different resistances for spin up and spin down electrons. b) Antiparallel configuration: now in both spin channels scattering events are possible. The resistance is equal for both spin channels. In total a higher resistance in the antiparallel case is the result.

for understanding qualitatively the factors leading to a spin-dependent conductivity. The relaxation time τ can be estimated from Fermis golden rules:

$$\frac{1}{\tau_{\uparrow,\downarrow}} = \frac{2\pi}{\hbar} \langle V_{scat}^2 \rangle N_{\uparrow,\downarrow}(E_F). \quad (2.8)$$

Here $\langle V_{scat}^2 \rangle$ describes an average scattering potential. In principle, all quantities in eq. 2.7 and eq. 2.8 depend on spin, but the origin of the spin-dependent conductivity leading to GMR can be understood as follows. On the one hand, the intrinsic properties n , m and $N_{\uparrow,\downarrow}(E_F)$ are entirely determined by the band-structure. The important quantity is the density of states which can be described as the superposition of a wide sp-band and a narrow d-band (the Δ_1 state in the previous section). Electrons from the sp-band provide the dominant contribution to the conductivity. The conductivity is mainly reduced by electron-scattering from the sp-band to empty states in the d-band. Since the d-band is spin split the reduction of the conductivity due to this scattering events is different for the majority- and minority-spin channel. On the other hand the scattering potential is an extrinsic property and can be either spin-dependent or spin-independent. Especially in diluted magnetic alloys, a spin asymmetry can be created by spin-dependent scattering potentials due to magnetic impurities [27], which could also play a role in alloys like Py. However, real GMR devices are far away from being perfect and defects like dislocations, stacking faults, or grain boundaries dominate and usually lead to spin independent average scattering potentials $\langle V_{scat}^2 \rangle$. Thus, the conductivity and the mean free path is mostly influenced by the spin polarized band structure. But with increasing material-quality spin-dependent scattering potentials can play a more important role. A direct consequence for the CIP geometry, where the current flows parallel to the layer structure, is the thickness limitation of the intermediate nonmagnetic layer. GMR is only observable when the majority of scattering events mainly take place in the ferromagnets, which requires that intermediate layer is thinner than the mean free path of the chosen material,

which is usually a few nm. In contrast to CIP, the CPP geometry, where the current flows perpendicular to the layer structure, not only larger GMR values are observed and devices with μm thick nonmagnetic layers are also possible [28, 29]. Further phenomena of spin-injection and accumulation come into play and the thickness of the intermediate layer is no longer limited by the mean free path, but by the much longer spin-diffusion length λ .

Spin Injection

The basic principle of spin injection is that a current flowing from a ferromagnetic metal into a nonmagnetic metal (NM) generates a spin polarized current in the nonmagnetic material, first observed by Johnson and Silsbee [30]. The spin polarization in the NM is induced by a spin accumulation at the interface between F and NM, depicted in fig.2.6a. The spin accumulation is defined as a local difference at the interface between the chemical potentials $\Delta\mu = \mu_{\uparrow} - \mu_{\downarrow}$ of the spin up and spin down electrons near the Fermi-level (see fig. 2.6b) and an imbalance of the chemical potential inside the NM is the result. Therefore the spin accumulation diffuses from the interface in all directions. The spin accumulation decays exponentially due to spin-flip processes with distance x from the interface, described by the diffusion equation [31]

$$\frac{\partial^2 \Delta\mu}{\partial x^2} = \frac{\Delta\mu}{\lambda^2}, \quad \text{with } \lambda = \sqrt{D\tau_s} \quad (2.9)$$

Here D is the diffusion constant and τ_s the spin relaxation time. One handicap arises in spin injection experiments when the nonmagnetic metal is replaced by a nonmagnetic semiconductor or carbon based materials like graphene or carbon nanotubes. In general spin injection is reduced by the so-called conductivity mismatch when a ferromagnet is connected to a nonmagnetic material

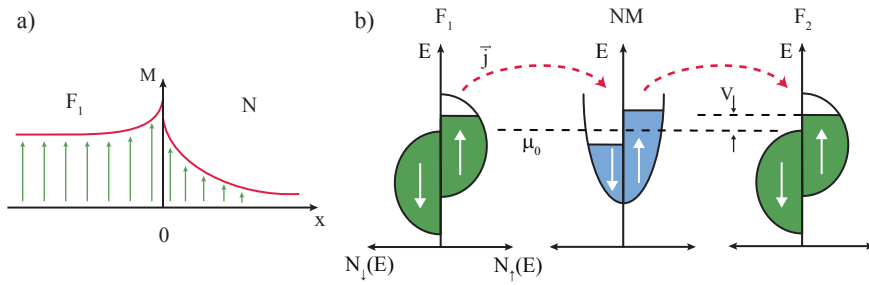


Figure 2.6: Basic principle of spin injection: a) A current flowing from a F into a NM induces a spin accumulation at the F/NM interface. The spin accumulation decays exponentially in a diffusive material. b) The spin accumulation in the NM leads to a local splitting of the chemical potentials for spin up and spin down electrons. With a second F connected to the NM the detection of the remaining spin polarized current is possible. This schematic has been adapted from [30].

with significant larger resistivity. [32]. The much larger density of states in the metal causes spin accumulation on both sides of the interface. Since the spin density accumulation in the metal is much larger and therefore a higher number of spin flips takes place. As a result the current becomes already depolarized before passing the interface. Adding a tunnel barrier between F and NM decouples the two materials and the resistance is dominated by the tunnel barrier and can solve therefore this problem [33, 34]. In principle the tunnel barrier induces a discontinuity in the spin accumulation and shifts the depolarization from the F side to the NM one.

2.2 Carbon Nanotube Quantum Dots

Carbon-based materials, like graphene or carbon nanotubes, are the perfect candidates to investigate spin transport, because of their potentially long spin lifetimes [35]. Carbon with four valence electrons exists in two different hybridizations:

- sp^3 , all four electrons are involved in the chemical bonding. This hybridization type forms the insulating material diamond.
- sp^2 , only three electrons form planar σ -bonds. The residual π -electron in the p_z orbital is free to move along the xy -plane and entirely determines the electronic band structure. Thus, the layered material graphite is the result.
- sp^1 , The 2s orbital mixes with only one of the three p-orbitals by forming linear chains like for example in Acetylen.

The weak binding between stacked layers in graphite provides the possibility to isolate one single sheet sufficiently from its environment, forming so called graphene [36, 37]. A carbon nanotube can then be imagined as graphene rolled-up into a seamless cylinder.

Carbon nanotubes

As the structures of graphene and carbon nanotubes (CNT) are related, the most convenient way of explaining the electronic structure of CNTs is starting with the one of graphene.

The sp^2 -hybridized carbon atoms of graphene form a 2-dimensional hexagonal honeycomb lattice with two sub-lattices A and B, depicted schematically in fig.2.7a. The delocalized π -electron can hop between the two sub lattices and the overlapping wavefunctions of neighboring π -electrons form the bonding

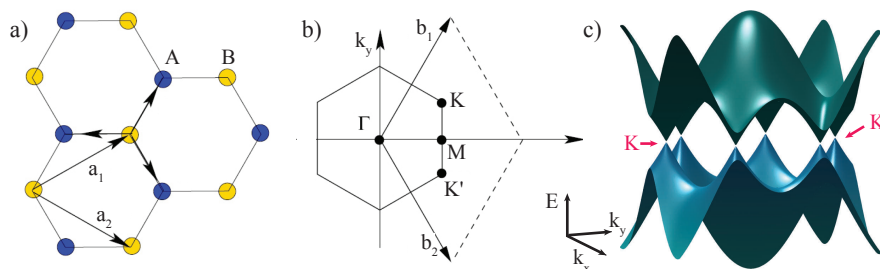


Figure 2.7: a) Hexagonal honeycomb lattice of graphene with sub lattice A (blue) and B (yellow). b) Corresponding first Brillouin zone. Only two of the six corners labeled K and K' are inequivalent. (Pictures taken from [38].) c) Band structure of graphene from the tight binding approximation. The conduction- and valence-band touch only at the K , K' points. Adapted from [39].

and antibonding orbitals. The corresponding dispersion relation can be calculated by applying the tight binding method [40] (see fig.2.7c). The Conducance and valence bands touch each other only at 6 specific points, according to the 6 corners of the first Brillouin-zone (fig.2.7b). Each corner belongs only about 1/3 to the Brillouin zone and therefore two of these 6 corners, labeled K and K' , are inequivalent. In a first approximation the dispersion relation close to the K, K' points is linear and can be expressed as:

$$E(\vec{\kappa}) = \pm \hbar v_F |\vec{\kappa}|, \quad \text{with } \vec{\kappa} = \vec{k} - \vec{K}, \quad (2.10)$$

with the Fermi velocity $v_F \sim 10^6$ m/s [41]. The linear dispersion relation close to the K, K' points is one of the remarkable characteristics of graphene, leading to zero effective mass for electrons and holes. Due to this dispersion relation, electrons and holes can be described as relativistic particles by the Dirac-equation. Therefor the K, K' points are often called Dirac-points. In undoped graphene the Fermi-energy lies at the Dirac-points, resulting in a completely filled/empty valence/conducance band respectively. Since the Fermi-energy is tunable by applying a gate-voltage, the carrier type and density can be seamlessly adjusted.

A carbon nanotube can be thought of as a rolled-up sheet of graphene the electronic properties of CNTs can be obtained from those of graphene by imposing periodic boundary conditions. On the one hand, the diameter d of a typical nanotube is in the range of a few nanometers, while the length can achieve several micrometers. Consequently, the circumferential momentum component $\vec{\kappa}_\perp$ becomes quantized while the one along the tube $\vec{\kappa}_\parallel$ is continuous. Owing to this, carbon nanotubes are often considered as prime example of a 1-dimensional system. The circumferential component $\vec{\kappa}_\perp$ can only increase stepwise described by the quantization condition

$$\Delta \kappa_\perp \pi d = 2\pi. \quad (2.11)$$

This condition corresponds to cross sections in the graphene bandstructure leading to 1-dimensional subbands:

$$E(\kappa_\parallel) = \pm \hbar v_F \sqrt{(\kappa_\parallel)^2 + (\kappa_\perp)^2}. \quad (2.12)$$

There are many ways to roll up graphene into a tube, the introduction of a chiral vector C is useful. The chiral vector points in the direction along the sheet is rolled up. All atoms of the graphene sheet have to fold onto the CNT atoms, the atoms on the seam have to be integer multiples of the lattice vectors (\vec{a}_1, \vec{a}_2) . Therefore the chiral vector \vec{C} is given by

$$\vec{C} = n\vec{a}_1 + m\vec{a}_2, \quad n, m \in \mathbf{Z}. \quad (2.13)$$

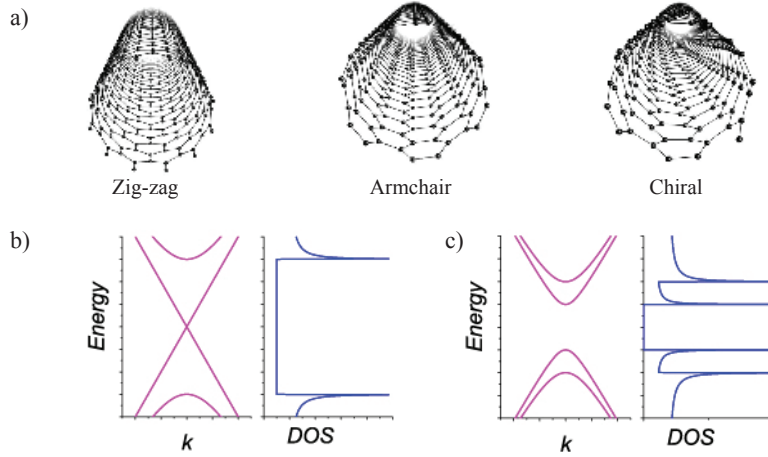


Figure 2.8: a) Schematic of the different types of carbon nanotubes depending on the chiral vector $\vec{C} = n\vec{a}_1 + m\vec{a}_2$. [42]. The quantization of the circumferential momentum component κ_{\perp} leads to 1-dimensional subbands represented by cross sections (pink lines) of the bandstructure of graphene. b) If the cross section meets the Dirac-point a metallic CNT is the result. The dispersion relation $E(\kappa_{\parallel})$ shows no energy bandgap. c) In the case of a semiconducting CNT the cross sections does not include the Dirac-point leading to an energy bandgap in the dispersion relation. Adapted from [43].

Nanotubes with $n = m$ are called armchair, those with $n = 0$ or $m = 0$ zig-zag and all others are named chiral, see fig.2.8a. With the help of the chiral vector the boundary conditions can be specified such that a distinction into two types of CNTs occur: metallic- and semiconducting-nanotubes. If $\vec{C} \cdot \vec{K}$ becomes zero, then the cross section in the graphene bandstructure includes the Dirac-point and $\kappa_{\perp} = 0$ is a solution to the boundary condition. Therefore the nanotube becomes metallic [42]. This is shown in fig.2.8b (pink lines represent the cross sections).

In contrast, the cross section for a semiconducting nanotube does not include the Dirac-point resulting in an energy gap in the dispersion relation $E(\kappa_{\parallel})$ (fig.2.8c). The displacement of the cross section from the Dirac-point is given by:

$$\pi d\kappa_{\perp} = \pm \frac{2\pi}{3}. \quad (2.14)$$

From this it follows that the energy gap is inversely proportional to the tube diameter d . In contrast to 3-dimensional materials where electron-scattering is possible in all directions, the 1-dimensionality of a carbon nanotube restricts scattering to only backward or forward scattering events [44]. This leads to a much lower scattering probability in CNTs and thus an increased mean free path of $\sim 10 \mu\text{m}$ [45]. The results in this thesis were obtained in devices with rather short ($\sim 300\text{nm}$) CNT channels, therefore the electron transport

can be assumed ballistic.

For achieving a confinement in the last dimension eventually resulting in quantum dot in a CNT one common approach is to connect the nanotube to metal electrodes acting as source (S) and drain (D) contacts (see fig.2.9a). For transparent contacts a two terminal conductance of $\frac{4e^2}{h}$ is expected, since the conductance channel is fourfold degenerated ($\uparrow, \downarrow, K, K'$). In real devices the contact resistance is mostly not fully transparent due to the formation of tunnel barriers at the metal/CNT interface. These tunnel barriers cause an additional lateral confinement along the tube axis and enable the formation of a quantum dot (0-dimensional electronic structure) in the CNT between the two contacts at low temperatures. The QD will be explained in more detail in the following.

Quantum dots

Quantum dots (QDs) can be thought of as small islands where electrons or holes are confined in all three spatial dimensions. This confinement leads to a quantized energy spectrum similar to atoms, therefore a quantum dot is often called artificial atom. The big advantage of a QD in comparison to an atom is the much larger size, ranging, from a few nanometers up to micrometers which allows the addition of capacitively coupled electrical contacts for the investigation of electron transport through such a structure.

A quantum dot is a very general system and can be realized in many different materials: For instance, self-assembled quantum dots [46], lateral or vertical QDs in 2-dimensional electron gases (2-DEGs) [47], semiconducting nanowires [48] or carbon nanotubes [49]. However, the major underlying physics that describes such systems are universal for all QD systems, like the discrete energy spectrum or the Coulomb blockade, where due to Coulomb repulsion a charging energy is required to add an electron/hole to the island. In contrast, shell filling or spin-orbit interactions for example are material dependent.

In a carbon nanotube electrons are confined naturally to 1-dimension. By introducing tunnel barriers, an additional longitudinal confinement can be achieved. These tunnel barriers can be generated for example by modifying the electrostatic potential using gate voltages [50] or by adding metallic electrodes which may induce Schottky barriers at the metal/CNT interface [51]. A schematic of a carbon nanotube device with two metallic electrodes is shown in fig.2.9a. Between these two electrodes, which can also act as source (S) and drain (D) contacts, a quantum dot forms at low temperatures (typically from ~ 10 mK to ~ 10 K, depending on the dot size). The tunnel barriers can be characterized by the tunnel coupling strengths $\Gamma_{S,D}$ and the capacitances $C_{S,D}$ of source and drain. In typical devices additional capacitively coupled gates allow for the control of the number of electrons/holes on the dot by tuning

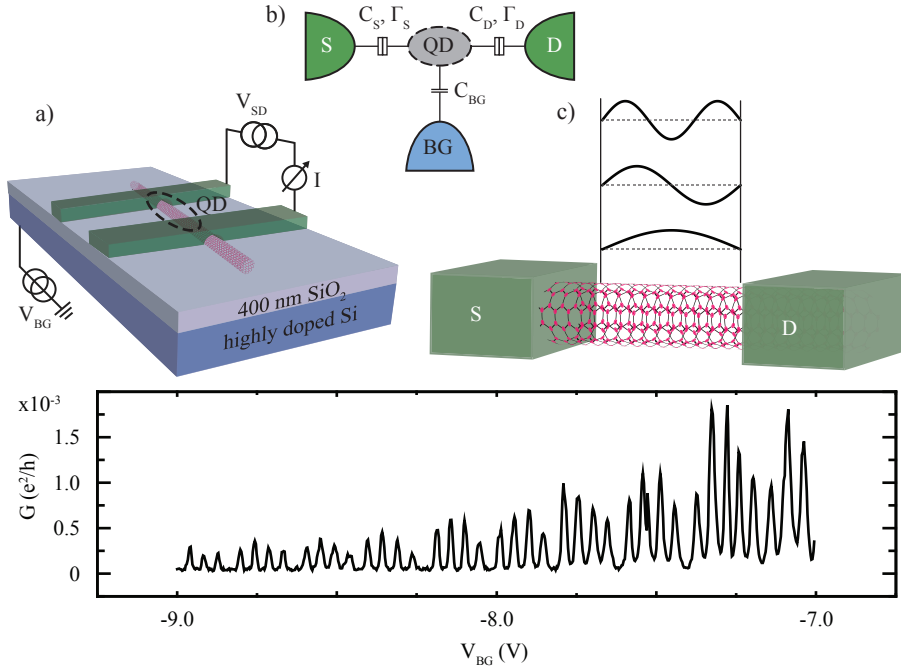


Figure 2.9: a) Schematic of a carbon nanotube device with nano patterned metal contacts on top. The highly doped silicon substrate serves as a backgate (BG). b) Capacitance model of a QD. Source (S), drain (D) and backgate are capacitively coupled to the CNT QD. In addition the electron transport across the CNT QD is determined by the tunnel coupling Γ_S, Γ_D of S and D respectively. c) The metal electrodes cause a longitudinal confinement leading to a quantized momentum component $\vec{k}_{||}$ separated by the level spacing δE . d) Measured differential conductance vs backgate. A clear 4-fold pattern of Coulomb blockade oscillations is visible.

the dot energy level positions. A simple capacitance model to describes such a system is given in fig.2.9b.

Due to the longitudinal confinement the parallel momentum component in the CNT $\vec{k}_{||}$ becomes quantized,

$$\vec{k}_{||} = \frac{n\pi}{L} \quad n \in \{1, 2, 3, \dots\}. \quad (2.15)$$

L is the distance between the two contacts and thus approximately the size of the quantum dot. In simpler words the nanotube quantum dot can be treated as a 1-dimensional particle-in-a-box system, where the longitudinal wave vector fulfills the boundary condition for a standing wave. A discrete energy spectrum is the result, see fig.2.9c. The spacing between two energy levels δE is approximately

$$\delta E = \hbar v_F \frac{\pi}{L}. \quad (2.16)$$

Each energy level can be filled with four electrons due to the spin (\uparrow, \downarrow) and orbital (K, K') degeneracy. Fig.2.9d shows an example for the gate dependence of the measured differential conductance $G = \frac{dI}{dV}$ across such a carbon nanotube quantum dot. The typical pattern of conductance peaks is visible, so called Coulomb blockade resonances, at certain backgate voltages V_{BG} . The occurrence of these Coulomb peaks in sets of four is referred as the 4-fold degeneracy of each energy level.

Following ref. [47] a common simplified model to describe electron transport through a QD with capacitively coupled S, D and BG is the constant interaction model (CIM). This model is based on two main assumptions:

- The discrete energy level spectrum of the QD is independent of the number of electrons (N) on the dot.
- The interactions of the electrons on the QD with the environment is covered by a single constant capacitance $C = C_S + C_D + C_{BG}$.

With these two assumptions the total energy E_{tot} of a QD containing N electrons is given in the CIM by

$$E_{tot} = \frac{(-|e|(N - N_0) + C_S V_S + C_D V_D + C_{BG} V_{BG})^2}{2C} + \sum_{n=1}^N E_n. \quad (2.17)$$

V_S, V_D and V_{BG} are the source, drain and backgate voltages, N_0 is the number of electrons on the dot at zero applied voltages and E_n is the n th energy level. The first term refers to the electrostatic potential of a capacitor. The terms $C_S V_S, C_D V_D$ and $C_{BG} V_{BG}$ describe the charges induced onto the island (gating-effect), which change continuously the electrostatic potential of the QD. Since the total energy E_{tot} depends quadratic on the backgate voltage it is more convenient to think in terms of electrochemical potentials μ_{dot} with linear dependence. The electrochemical potential of the dot is defined as:

$$\begin{aligned} \mu_{dot}(N) &= E_{tot}(N) - E_{tot}(N - 1) \\ &\propto NU - \frac{|e|}{C}(C_S V_S + C_D V_D + C_{BG} V_{BG}) + E_n. \end{aligned} \quad (2.18)$$

$U = e^2/C$ is the charging energy referring to the energy required to overcome the Coulomb repulsion. Two electrochemical potential levels are spaced by the addition energy E_{add} :

$$E_{add}(N) = \mu_{dot}(N + 1) - \mu_{dot}(N) = U + \delta E. \quad (2.19)$$

δE is the energy level spacing given in eq. 2.16. The resulting "ladder" of the electrochemical potential levels is depicted in fig.2.10. The continuous pink lines represent occupied states while the dashed pink lines correspond to empty states. The tunnel coupling to S and D is described by the rates Γ_S and Γ_D . In fig. 2.10a the off-resonance situation is depicted, where the electrochemical potential levels of the leads (μ_S, μ_D) are positioned between an occupied and empty level of the dot. Thus electrons from source or drain have not enough energy to enter the empty level of the dot. No electron transport is possible, resulting in a conductance G equal to zero. This situation is called Coulomb blockade. Since the electrostatic potential of the QD can be changed by applying a gate voltage V_{BG} , the whole electrochemical potential "ladder" can be shifted linearly according to αV_{BG} . The lever arm $\alpha = -|e| \frac{C_{BG}}{C}$ is just an efficiency factor of the gate coupling. This allows one to align an empty dot level μ_{dot} with μ_S and μ_D by changing the gate voltage V_{BG} , see fig.2.10b. Now electron transport is possible, resulting in a conductance peak. Recording the differential conductance G while sweeping the gate voltage V_{BG} leads to the characteristic Coulomb-blockade-oscillation pattern shown in fig.2.9d. Each peak in the measurement corresponds to an alignment of the electrochemical potentials. The four-fold pattern of the Coulomb peaks can be understood in the following way: all energy levels E_n are four-fold degenerated ($\uparrow, \downarrow, K, K'$) and therefore every energy level corresponds to 4 electrochemical levels. The spacing of these levels determined by the addition energy E_{add} (see eq. 2.19) becomes equal to the charging energy U since the energy level spacing δE is zero. Two sets of four electrochemical potential levels correspond to two different energy levels E_n, E_{n+1} are then spaced by the charging energy U plus the energy level spacing δE .

Every Coulomb peak can be described by Lorentzian profiles with a full-width half-maximum of $\Gamma = \Gamma_S + \Gamma_D$ at low temperatures ($\Gamma \gg k_B T$) [52]. According to Heisenbergs uncertainty relation $\Delta E \Delta t \geq \hbar$ the intrinsic lifetime

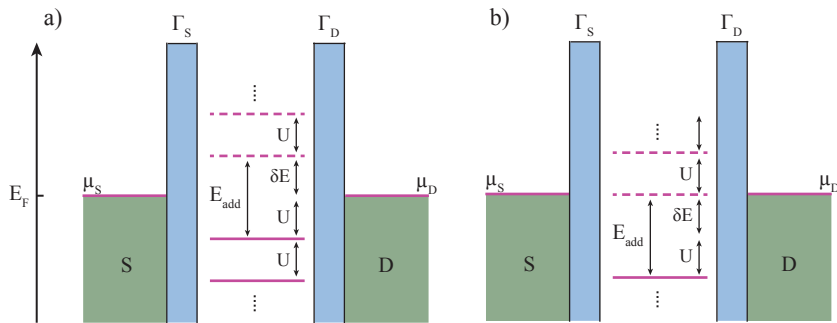


Figure 2.10: Energy diagram of a quantum dot. a) Off-resonant situation. The QD is in Coulomb blockade and no electron transport is possible. b) In resonance all three electrochemical potential levels are aligned (μ_S, μ_D and μ_{dot}), resulting in electron transport.

broadening is approximately given by the average dwell time $\Delta t \approx h/\Gamma$ of an electron on the dot.

The application of a DC bias voltage V_{SD} between the source and the drain contacts can also generate electron transport across the QD (see fig.2.11a). In common measurements D is kept on ground leading to $\mu_D = 0$ and the voltage is applied on the S. Since $\mu_S = -|e|V_{SD}$ a positive applied voltage V_{SD} decreases the electrochemical potential of the S and opens a so called bias window: $\mu_S \leq \mu_{dot}(N) \leq \mu_D$. Due to the capacitive coupling of S and D to the QD the electrochemical level of the QD decreases by $\Delta\mu_{dot} = eV_{SD}\frac{C_S}{C}$ and has to be compensated by the gate voltage, $\Delta V_{BG}\frac{C_{BG}}{C} = -\Delta V_{SD}\frac{C_S}{C}$. Whenever a chemical potential level enters the bias window an electron can tunnel on and off the dot. Therefore the conductance changes abruptly resulting in a measured peak in the differential conductance. Typical measurements to characterize a QD is the mapping of the conductance G as function of V_{BG} and V_{SD} . In fig.2.11b such a so called stability diagram is schematically drawn and shaded with data from a typical measurement of a CNT QD at 230 mK. In such a color scale plot where the color refers to the conductance G , a diamond-shaped pattern is visible (pink lines and bright background). These lines corresponds to situations where the dot level is either aligned with μ_S, μ_D or both. At the top of a diamond two lines crosses, corresponding to $V_{SD} = E_{add}$ and two chemical potentials are within the bias window. The pattern of three smaller diamonds enclosed by two big diamonds reflects the 4-fold degeneracy

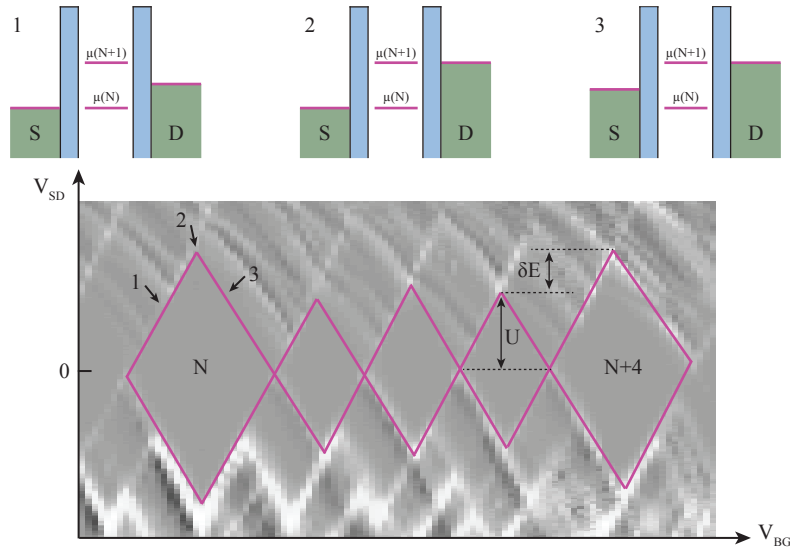


Figure 2.11: a) Schematic of the energy diagram at finite bias V_{SD} . b) Measurement of the conductance G (color) as a function of bias and backgate. The typical coulomb diamond pattern is highlighted with pink lines.

of the CNT QD levels. In the space of such a Coulomb diamond the number N of the electrons on the dot is fixed and the dot is in Coulomb blockade. From the stability diagram the following information for the characterization of the QD can be extracted:

- Charging energy U and energy level spacing δE . Points in the stability diagram where two pink lines crosses denote situations wherever $-|e|VSD = E_{add}$.
- C_S, C_D and C_{BG} . The slopes of the Coulomb diamonds are given by $\beta = \frac{\Delta V_{SD}}{\Delta V_{BG}} = \frac{C_{BG}}{C - C_S}$ and $\gamma = \frac{\Delta V_{SD}}{\Delta V_{BG}} = -\frac{C_{BG}}{C_S}$. Together with the charging energy $U = \frac{e^2}{C}$ one can calculate the important capacitances.
- The lever arm $\alpha = \frac{\beta|\gamma|}{\beta+|\gamma|}$ follows from the slopes as well. The lever arm is needed to convert applied voltages into energy.
- The lifetime broadening Γ one gets from a Lorentzian fit to a single Coulomb peak.

For achieving spin transport phenomenas in CNT QD one has to replace the nano patterned source and drain metal electrodes by ferromagnetic metals. The arising possibility for controlling the electron transport across a QD not only by applying a gate or bias voltage but additionally by the alignment of the magnetization (parallel or antiparallel) of the ferromagnetic electrodes results e.g. in a gate dependence of the magneto resistance and will be explained more detailed in the following section.

2.3 Spintransport in CNT Quantum Dots

Replacing the normal metal electrodes in CNT QD devices, described in chapter 2.2, with ferromagnetic materials like Fe, Co, PdNi or Py lateral spin-transport experiments on carbon nanotube quantum dots become possible. The ferromagnetic contacts are shaped into long rectangular strips with two different widths. As a consequence of the shape anisotropy, the coercive fields H_c of the two strips are different³ and the direction of the magnetization can be set by an external magnetic field. Recent experiments on devices with PdNi contacts in the sequential tunneling regime demonstrated a gate dependence of the magneto-resistance. This includes the observation of a negative MR [4]. Finding an explanation for the underlying mechanisms is still ongoing research and two qualitatively different approaches [53, 54] coexist so far. This chapter discusses the observed negative MR and introduces the two theoretical approaches.

Negative Magneto-Resistance

Common spin-transport experiments on a CNT QD tune the QD to a fixed backgate voltage and sweep the magnetic field (applied parallel to the F strips) while mapping the conductance. In ref.[4] a MR depending on the backgate voltage was observed and can be either positive ($G_P > G_{AP}$) or negative ($G_P < G_{AP}$). This is schematically illustrated in fig.2.12a for two different backgate voltages V_{BG} . The measured linear conductance G_P and the corresponding MR for several V_{BG} is shown in fig.2.12b [4]. The MR oscillates with V_{BG} and maxima/minima in the MR occur if the V_{BG} is fixed at the right/left slope of a Coulomb peak respectively. The definition $MR = \frac{G_P - G_{AP}}{G_{AP}}$ is used for calculating the MR in fig.2.12. Since the MR can become positive and negative the more symmetric definition

$$MR = \frac{G_P - G_{AP}}{G_P + G_{AP}} \quad (2.20)$$

is used in this thesis and provides an equal measure for positive and negative MR values. One reason for the oscillating MR could be shifts of the Coulomb peak position sketched in fig.2.12c. Another possibility for the observation of negative MR is depicted in fig.2.12d. Here a larger amplitude of the Coulomb peak in the antiparallel alignment can cause negative MR as well. Two approaches for explaining the observation of negative MR by spin-dependent energy level shifts exist. Both approaches trace back the underlying mechanism to an effective Zeeman shift of the QD energy levels. But they differ in the origin of this Zeeman shift: In the first approach spin dependent interfacial phase shifts are assumed while the second approach uses a renormalization of the energy levels induced by charge fluctuations .

³details explained in chapter (4.3)

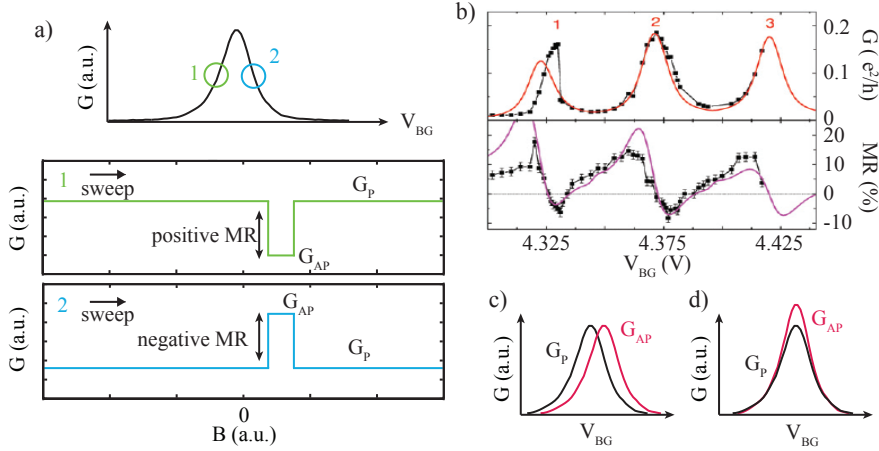


Figure 2.12: a) Schematic of the observed MR for two different V_{BG} . The MR can be either positive ($G_P > G_{AP}$) or negative ($G_P < G_{AP}$) if the backgate voltage is tuned to the right or left slope of a Coulomb blockade peak respectively. b) Measurements of the conductance G (parallel alignment) and corresponding $MR = \frac{G_P - G_{AP}}{G_{AP}}$ as a function of V_{BG} (taken from [4]). A shift of the Coulomb peak position c) or a change of the amplitude of a Coulomb peak d) can lead to negative MR.

Spin Dependent Interfacial Phase Shifts (SDIPS)

For the understanding of spin dependent interfacial phase shifts it is useful to start with the non-interacting model. In the non-interacting case the nanotube can be treated as a one-dimensional ballistic wire contacted by ferromagnetic leads [53]. The ballistic nature of the nanotube allows for coherent multiple reflections between the two F contacts. Therefore transport properties are mainly determined by quantum interferences leading to Fabry-Perot like resonances of discrete energies E_{res} . Electron transport in the non-interacting limit can be described by using a scattering approach [55]. Scattering events at the interface F/CNT can be spin dependent since electrons with spin parallel or antiparallel to the magnetization of the F scatter with different phase shifts. This is due to different scattering potentials at the interface caused by the exchange fields of the F leads. This spin dependence of interfacial phase shifts (SDIPS) modifies the resonant energy levels and therefore the conductance of such mesoscopic devices. In particular, SDIPS can cause a Zeeman like spin splitting

$$g\mu_B h_{SDIPS}^c = E_{res\downarrow}^c - E_{res\uparrow}^c \quad (2.21)$$

of the resonant energies. Index $c \in \{P, AP\}$ describes the magnetic configuration of the F leads and h_{SDIPS}^c stands for an effective Zeeman field. In contrast to an external magnetic field the effective field depends on the configuration c of the F electrodes. For example for symmetric coupled F contacts the effective field vanishes in the antiparallel configuration. Results in recent

MR measurements on CNTs with transparent PdNi contacts in the Fabry-Perot regime [5] are well described by this approach.

In the interacting case Coulomb interaction is present in the nanotube segment. Instead of a one-dimensional wire one has to consider a QD connected to the F leads. The scattering approach is no longer suitable in the interacting regime but can be replaced by a description based on an effective Anderson Hamiltonian

$$H = H_{dot} + H_{leads} + H_c \quad (2.22)$$

with

$$H_{dot} = \sum_{n,\sigma} E_{n\sigma} c_{n\sigma}^\dagger c_{n\sigma} + \sum_{n,n',\sigma,\sigma'} \frac{U}{2} c_{n\sigma}^\dagger c_{n\sigma} c_{n'\sigma'}^\dagger c_{n'\sigma'} \quad (2.23)$$

$$H_{leads} = \sum_{k,\sigma} E_{k\sigma} c_{k\sigma}^\dagger c_{k\sigma} \quad (2.24)$$

$$H_c = \sum_{n,k,\sigma} (t_{n\sigma}^k c_{n\sigma}^\dagger c_{k\sigma} + (t_{n\sigma}^k)^* c_{k\sigma}^\dagger c_{n\sigma}) \quad (2.25)$$

$E_{n\sigma}$ refers to the n th Energy level of the QD with spin $\sigma \in \{\uparrow, \downarrow\}$. $E_{k\sigma}$ describes the energy state k of the lead for spin σ and $t_{n\sigma}^k$ is a hopping matrix element (from leads to QD) where the spin σ is preserved during the tunnel event. The notion of interfacial scattering phases is less intuitive than by using a scattering approach. However, in the Hamiltonian H_{dot} for the charging energy $U = 0$ each energy level of the quantum dot E_n corresponds to a resonant energy level E_{res} in the scattering approach with $E_{n\downarrow} - E_{n\uparrow} = g\mu_B h_{SDIPS}^c$. Therefore it is possible to incorporate the observed effective Zeeman splitting h_{SDIPS}^c in the Hamiltonian for the interacting case. This is based on the idea to adapt the spin dependent scattering potentials caused by the ferromagnetic exchange field by confinement potentials which are assumed to be spin dependent as well. The spin dependent confinement potentials are illustrated in fig.2.13a,b.

For comparison with the experimental data the corresponding conductance can be calculated by using an equation of motion (EOM) technique [57]. The resulting conductance with corresponding MR is plotted for two different values of h_{SDIPS}^c in fig.2.13c. The orbital (K, K') degeneracy in a carbon nanotube is considered in addition to the spin degeneracy in the Hamiltonian with $n \in \{K, K'\}$ and $E_{K\sigma} = E_{K'\sigma}$ [56]. In doing so high-order quantum processes that couple K and K' orbitals are neglected. For $h_{SDIPS}^P = h_{SDIPS}^{AP} = 0$ the MR remains positive for any backgate voltage as one would expect from conventional spin-valve measurements. For finite h_{SDIPS}^c the MR oscillates and exhibits a negative MR depending on the QD occupation and therefore on

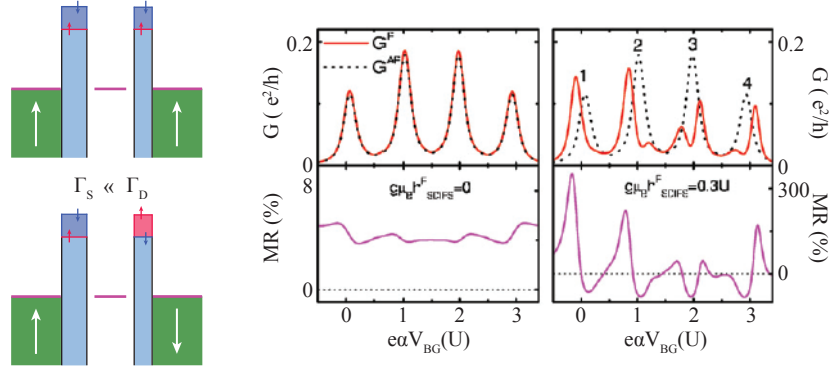


Figure 2.13: Schematic illustration of the spin dependent confinement potentials in the parallel a) and antiparallel case. For symmetrically coupled F contacts $h_{SDIPS}^{AP} = 0$ and therefore the effective Zeeman splitting of the QD energy level is only present in the parallel configuration. c) Calculated conductance and corresponding MR using the interacting model for two different h_{SDIPS}^c values [56].

different energy level shifts. Peak 1 and 2 for example shift to lower backgate voltages while Peak 3 and 4 shift to larger values. In addition, splittings of the conductance peaks in the parallel alignment are visible for peak 3 and 4 (which are double occupied). The splitting is only resolved for large values of h_{SDIPS}^c but even for lower values the effect of SDIPS persists and could be used for fitting the data from reference [4] (pink line in fig.2.12b).

However, the spin dependent energy level shifts in this approach depend only on the spin active interface and are therefore almost gate independent.

Recent experiments on CNTs [58] and InAs nanowires [59] in the Kondo regime showed in contrast that energy level shifts can be partly gate dependent and gate independent. It is possible to explain both contributions by virtual charge fluctuations which is explained in more detail in the following section.

Level Renormalization Induced by Charge Fluctuations

Since the QD is connected to F leads with a difference in the density of states for spin \uparrow and spin \downarrow an asymmetry of the tunnel coupling $\Gamma_{\uparrow,\downarrow}$ to the QD can be induced [60, 61] by charge fluctuations. Due to the hybridization of the dot level with the leads, the spin dependent tunnel coupling generates a spin imbalance on the dot leading to an intrinsic effective Zeeman field h_{int} . This is schematically depicted in fig.2.14a,b where the discrete energy level (not the electrochemical potential) of the QD is shown between two F contacts (arrows in the leads reflect the difference of the DOS).

Following ref. [54] an effective generalized Zeeman field $h^c(V_{BG})$, $c \in \{P, AP\}$

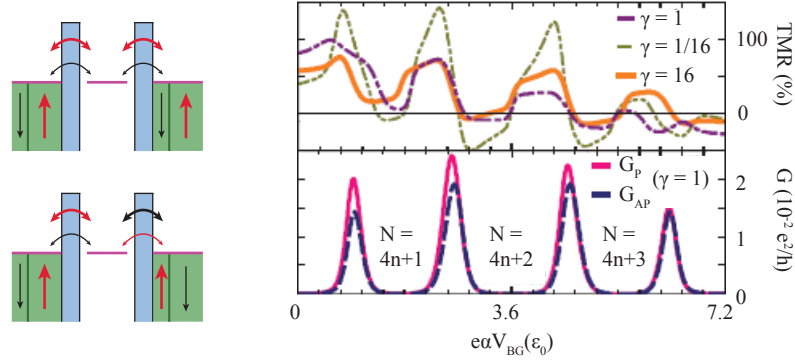


Figure 2.14: Schematic view of the lifted spin degeneracy on the QD energy level by an induced effective Zeeman splitting due to charge fluctuations. The splitting differs for parallel a) and antiparallel b) alignment of the F contacts. c) Calculated linear conductance with corresponding MR from diagrammatic approach to the reduced density matrix [54].

is assumed and leads to a negative MR. In this model the effective field includes extrinsic (stray fields, applied magnetic field) and intrinsic (charge fluctuations) sources. A CNT quantum dot in the sequential tunneling regime is considered with sufficiently small couplings where the Coulomb peak width Γ is determined by the temperature. Then at least two possibilities can lead to negative MR. First, if $|h^P| = |h^{AP}| \approx k_B T$ the effective Zeeman splitting removes the spin degeneracy and can lead to $G_{AP} > G_P$ (see fig.2.12d). In this case the ground state of the QD favors states with total maximum spin. Possible ground states of a CNT in shell n are:

- $N = 4n$ $|\cdot, \cdot\rangle$
- $N = 4n + 1$ $|\uparrow, \cdot\rangle, |\cdot, \uparrow\rangle$
- $N = 4n + 2$ $|\uparrow, \uparrow\rangle$
- $N = 4n + 3$ $|\uparrow\downarrow, \uparrow\rangle, |\uparrow, \uparrow\downarrow\rangle$

For example for the transition between $4n + 2 \leftrightarrow 4n + 3$ electrons on the QD, spin-down electrons have to be transferred. Since in the parallel magnetic configuration spin-down electrons are in the minority, the peak height for antiparallel alignment exceed those for the parallel case. Second, if $|h^P - h^{AP}|$ is on the order of the peak width $\Gamma = k_B T$ the peak positions for the P and AP configuration can shift with respect to each other (see fig.2.12c) This would lead to the situation depicted in fig.2.12a including negative MR values.

In this model electron transport is described by the total Hamiltonian

$$\hat{H}_{tot}^{P/AP} = \hat{H} + \hat{H}_{ext}^{P/AP} + \sum_{l=S,D} \hat{H}_l + \hat{H}_T,$$

where $\hat{H} = \hat{H}_0 - e\alpha V_{BG}\hat{N}$ is the isolated QD (\hat{H}_0) and the effect of an applied gate voltage V_{BG} . \hat{N} is the total number of electrons in one energy level. The Term $\hat{H}_{ext}^{P/AP}$ considers extrinsic gate independent level splittings and contains at least the contribution from the applied magnetic field for controlling the magnetization of the F leads. The leads $\sum_{l=S,D} \hat{H}_l$ are described similar to eq.2.24 where S, D stands for source and drain respectively. \hat{H}_T considers tunnel events between CNT and leads as a perturbative contribution to the total Hamiltonian. The conductance can be calculated within a diagrammatic approach to the reduced density matrix of this nanosystem [62]. Especially the intrinsic level normalization h_{int} caused by charge fluctuations can be expressed more detailed. For the case of a flat bandstructure including a finite Stoner splitting Δ_{St} in the leads one obtains

$$h_{int} = h_0 + \Delta h(\Delta_{St}).$$

h_0 depends on the energy level position of the dot and therefore on the gate voltage. In contrast the contribution of the Stoner splitting described by Δh is almost gate independent. Ref. [54] calculated the conductance and corresponding MR for varying contributions of external shifts $h_{ext}^{P/AP}$, intrinsic shifts h_{int} , Stoner splittings Δ_{St} and coupling asymmetries $\gamma = \frac{\Gamma_S}{\Gamma_D}$. The major result for combining intrinsic shifts (which depend on the dot occupation) with equal extrinsic splittings $|h_{ext}^P| = |h_{ext}^{AP}|$ is plotted in fig.2.14c and may reflect the shape of the measured MR in fig.2.13c.

Both theoretical models describe a $MR(V_{BG})$ pattern depending on the occupation of the QD. Especially due to the four-fold degeneracy of the QD energy level peak shifts are predicted which differ from peak to peak. In addition, situations are described where the amplitude of a Coulomb peak can become larger in the antiparallel configuration than in the parallel one. Up to now, however, no MR experiments on CNT QDs exhibiting a clear four-fold conductance pattern or at least over a backgate range containing four peaks could be performed.

BASICS OF DEVICE FABRICATION AND EXPERIMENTAL
SET-UP

* * *

Devices are the heart of almost every research project in the field of nanoelectronics. The general fabrication procedure used in this thesis is introduced in this chapter and details of each fabrication step can be found in appendix A. Additionally, the set-up for transport measurements at low temperatures is described at the end of this chapter.

3.1 Sample Fabrication

The starting point for all devices are highly p-doped Si wafers covered with a 400 nm thick insulating thermally grown SiO₂ layer cut into 1 × 1 cm² pieces. The use of highly doped silicon wafers enables the possibility for applying a backgate voltage. After growing the CNT on top of the SiO₂, standard electron-beam (e-beam) lithography and metalization processes are used to contact the CNT. The general fabrication process is depicted schematically in fig.3.1.

Carbon Nanotube Growth

After a thorough cleaning procedure of the wafer pieces, the CNTs are grown by using chemical vapor deposition (CVD) [63]. For this the wafer is spin-coated with an iron (Fe)-ruthenium (Ru) based catalyst solution and placed in the quartz tube of a CVD-oven. The FeRu-catalyst is used since recent experiments have shown that this recipe yields single-walled CNTs with diameters ranging from 0.7 nm - 1.8 nm and typical lengths of 2-10 μm [64]. The formation of tunnel barriers at the metal/CNT interface benefits from small CNT diameters and improves the spin transport measurements [65]. The wafer in the CVD-oven is heated up to 850° C under an argon (Ar) flow. At the desired temperature the Ar flow is replaced by methane and hydrogen for 10 min. The methane provides the carbon for the CNT growth and assembles at the catalyst particles. The hydrogen reacts with the excess carbon and helps to avoid the growth of nanotubes in bundles. After the growth process, the wafer is cooled to room temperature under Ar and H₂ flow. A schematic of this fabrication procedure and a corresponding scanning-electron-microscope (SEM) picture of a resulting CNT is shown in fig.3.1a.

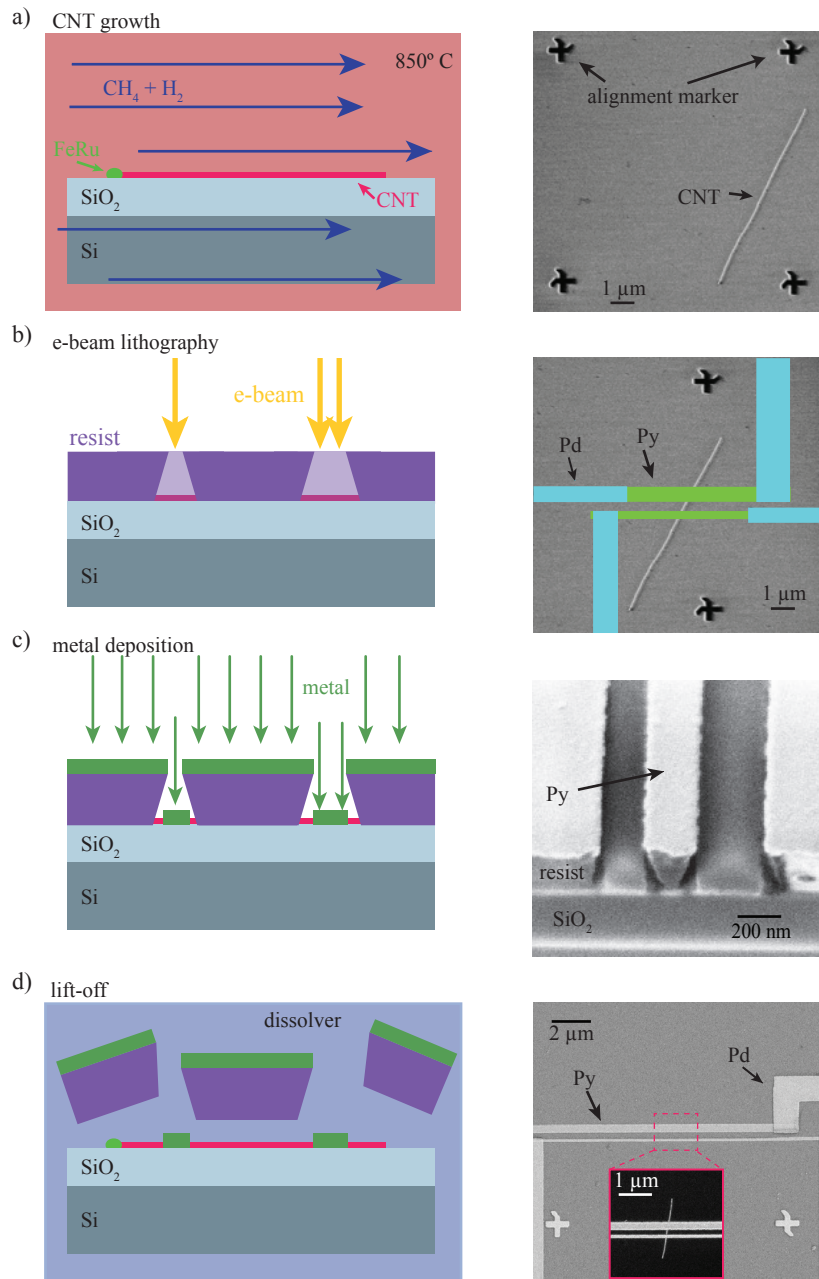


Figure 3.1: Schematic of the fabrication steps. a) Illustration of the CNT growth with corresponding SEM picture of the result. b) E-beam lithography step to transfer the designed structure into the resist layer. c) Metal deposition. The SEM picture shows a cross section of a fabricated test sample after the metal deposition. d) Immersing the sample onto a dissolver, removes the remaining resist with metal on top. SEM: example of a real fabricated device.

E-Beam Lithography and Metalization

For fabricating a grid of alignment markers, contacts to the CNT and contact pads for bonding, three e-beam lithography steps are required, followed by a metalization process after each lithography step (see fig.3.1b, c). The alignment markers are necessary for locating the carbon nanotubes and serve as coordinate system for all following lithography steps, allowing an alignment with an accuracy of < 10 nm. The alignment markers are fabricated directly after the nanotube growth. For this, the wafer is spin-coated with a few 100 nm thick resist layer. In this thesis two different resists, PMMA¹ and ZEP 520 A², are used and details are reported in chapter 4. After hardening the resist on a hot-plate, the desired structure can be transferred into the resist via a highly focused e-beam exposure. Fig.3.2 gives an overview of the structures used. The exposure to an e-beam breaks up the polymer chains of the resist, which are then removed by a developer bath, see fig.3.1d. As developer, a solution of 1 part methyl isobutyl ketone (MIBK) and 3 parts of IPA is used for the PMMA and n-amylacetat for the ZEP. After the lithography step, metal is deposited on top of the remaining resist mask. For the alignment markers a 5 nm thick titanium (Ti) adhesion layer followed by a 45 nm thick gold (Au) layer is deposited by e-beam evaporation in a high vacuum chamber (base pressure $\sim 10^{-7}$ torr).

Removing the remaining resist (covered with metal) in a so-called lift-off procedure completes the lithography step. For the lift-off the device is immersed in hot acetone for PMMA and in hot n-methyl-2-pyrrolidone (NMP) for ZEP. For selecting individual CNTs for further fabrication steps, SEM imaging is used for locating the CNT with respect to the alignment marker grid (SEM picture in fig.3.1a). After transferring the carbon nanotube position to a design file (GDS II-file, CLeWin), see fig.3.2d, the contacts to CNT and the bonding pads can be easily fabricated by following the above described procedure in a repetitive manner. The procedures differ only due to differently deposited materials in the metalization process.

For contacting the carbon nanotubes, Py ($\text{Ni}_8\text{OFe}_2\text{O}$) is the chosen material for this thesis. 25 nm thick Py shaped into long ($\sim 10\mu\text{m}$) rectangular strips of different widths (from 150 nm to 400 nm) provide single-domain contacts with a high control over the magnetic properties [66]. The Py is deposited by e-beam evaporation in an ultra high vacuum (UHV) chamber (base pressure $\sim 10^{-9}$ torr) or with UHV-magnetron-sputtering (base pressure $\sim 10^{-9}$ torr). The Pd (50 nm) for the bond pads is deposited by e-beam evaporation in an UHV chamber. It has to be mentioned that the devices are exposed to

¹polymethyl methacrylat, Ar-P 671.09 950K, Allresist

²ZEP 520A, composed of 11% methyl styrene and chloromethyl acrylate copolymere an 89% anisole (solvent) by ZEON corporation.

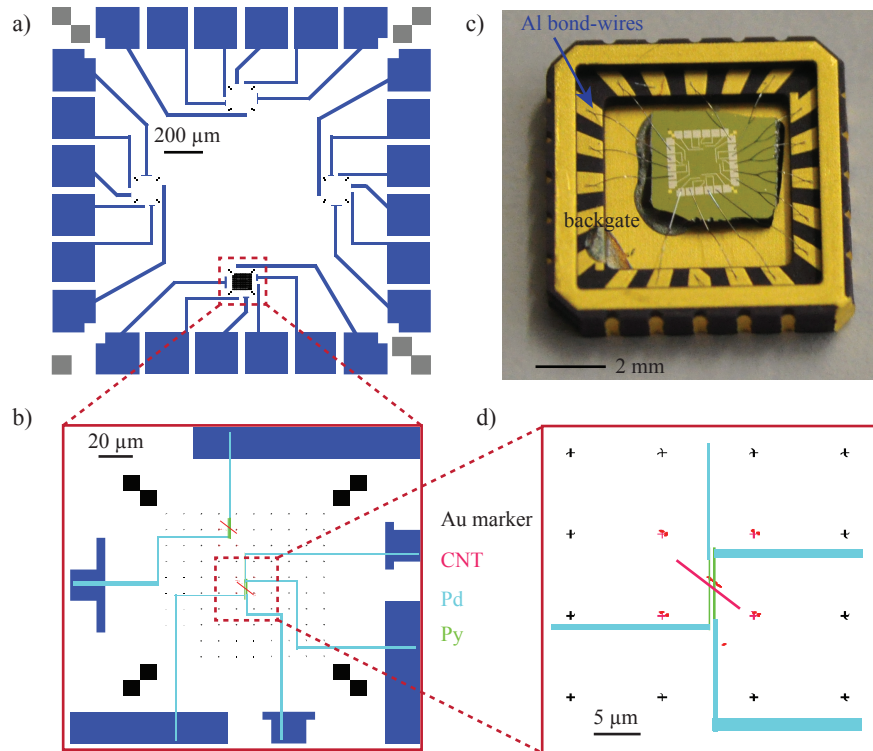


Figure 3.2: a) Schematic of the design files with bond-pads b) Alignment grid and contacts to the nanotube (zoom in). c) Device glued in a chip carrier. Al bond wires connect the bond pads of the device with bidirectional Au pads of the chip carrier.

air between every lithography step, which can lead to oxide formation on the metal surfaces, especially of Py. Therefore an argon sputtering step is done before the Pd deposition to remove the oxide of Py in-situ.

On each wafer piece four structures depicted in fig.3.2a are fabricated in parallel. This allows for contacting at least 16 nanotubes in one fabrication process. Afterwards the wafer is cut into 4 pieces ($4 \times 4 \text{ mm}^2$) and glued with silver paint onto a so-called chip carrier (see fig.3.2c). The gluing with silver paint provides the electrical contact to the backgate. The chip carrier bridges the fabricated nanostructure with the macroscopic measurement set-up. They consist of 20 bidirectional Au contact pads. One side is connected to the nanostructure with aluminum wires done in a commercial ultra sonic wire bonder. The chip carrier is mounted on a chip carrier socket which connects the other side of the chip carrier with further contacts. These further contacts are soldered to the measurement lines.

3.2 Measurement Set-Up

In the first place the samples are tested with a needle prober at room temperature (RT). For this an AC voltage of $100 \mu\text{V}$ is applied between the two contacts and the two terminal resistance of the device is measured with a lock-in amplifier³. The criteria for a working device at RT is the observation of a two terminal resistance below $1 \text{ M}\Omega$, since devices with higher resistances are often fully depleted at low temperatures and do not become conducting anymore. In case the criteria is fulfilled the device is transferred to a low temperature measurement set-up. A schematic of a typical set-up is depicted in fig,3.3. Cryogenic temperatures are needed to resolve the single electron levels of a quantum dot.

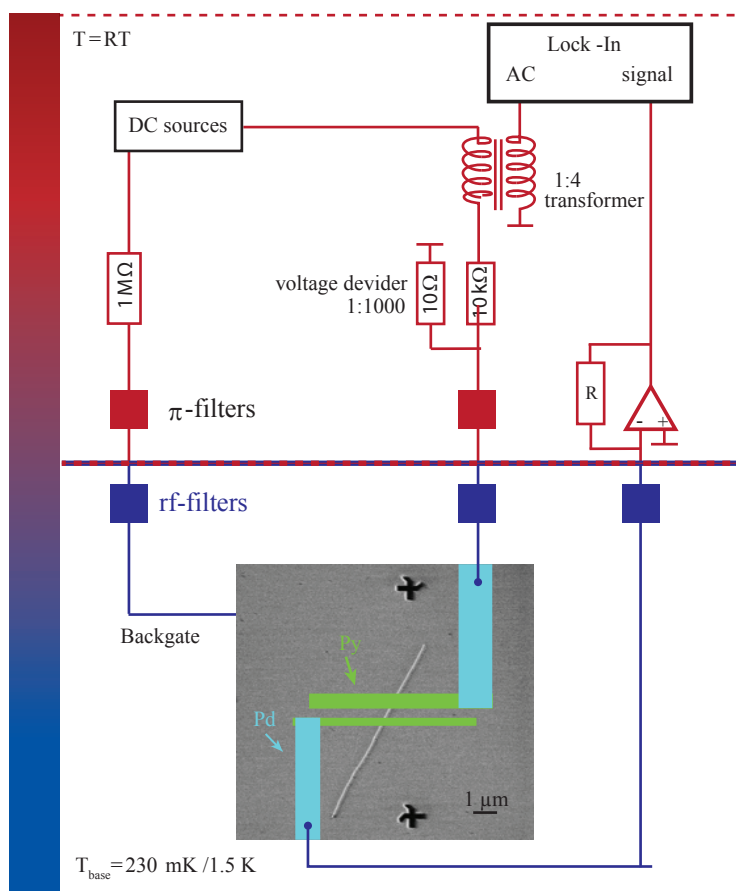


Figure 3.3: Schematical illustration of a typical low temperature measurement set-up. The set-up offers voltage biased differential conductance measurements via lock-in technique. Blue parts are placed inside the cryostat while red parts are at RT under ambient conditions.

³Stanford SR 830

Therefore it is crucial that the temperature $k_B T$ is lower than for example the charging energy $U \sim \text{meV}$ and the level spacing $\delta E \sim \text{meV}$. For achieving sufficient low temperatures cryostats are used. For this thesis mainly two cryostats were used based on different liquid helium (He) isotopes. One with ^4He where temperatures ~ 1.5 K can be reached and one with ^3He with temperatures ~ 230 mK. Liquid ^4He has a temperature of 4.2 K. For achieving lower temperatures one can remove evaporated ^4He particles by pumping. The removal of latent heat leads to further cooling down of the liquid to ~ 1.5 K. The helium isotope ^3He has a higher vapor pressure yielding a lower boiling point. Pumping on a ^3He bath yields temperatures ~ 230 mK. Since ^3He is quite rare and therefore expensive, so-called ^3He cryostats provide a closed ^3He cycle surrounded by a ^4He bath. The evaporated ^3He can be collected in a charcoal sorbtion pump (sorb). Heating up the sorb to 30 K for releasing the collected helium one can condensate the ^3He back again with a controlled cooling by evaporating ^4He .

For transport measurements at low temperatures the device has to be placed in such a cryostat and connected to the read out electronics at RT. The measurement lines connecting the cold device with the RT set-up usually contains heat leaks caused by insufficient precooled cables or electromagnetic radiation. A good thermal anchoring of the cables and strong filtering of high frequency radiation (e.g a frequency of 2 GHz = Tk_B/h correspond to a temperature of ≈ 100 mK) is required. Therefore, the device is shielded by a Faraday-cage and radiation baffles are installed along the insert. Specifically designed so-called tape-worm filters (rf-filters) [67] are installed at cryogenic temperatures consisting of twisted wire pairs packed into copper foils and commercial π -filters from Syfer at RT. The cut off frequencies are $f > 10$ MHz for the tape-worm filters and $f > 1$ MHz for the π -filters.

The measured devices can exhibit resistances up to several M Ω and therefore voltage biasing of the sample is the choice for performing transport measurements. To do so the device is biased with a DC voltage⁴ $\sim 0 - 10$ mV superimposed by a small AC excitation voltage⁵ $\sim 10 - 100$ μV with a typical frequency of ~ 77 Hz, see fig.3.3. I/V-converters (typical gain of 10^7) convert the generated AC current into an AC voltage which is then measured by a lock-in amplifier. To keep the noise level as low as possible the I/V converter is placed close to the cryostat. Additionally a second DC voltage source is connected to the backgate of the sample with a resistance in series to protect the device from accidentally occurring leakage currents. The set-up and read out of the data is controlled by Labview programs and a general purpose interface bus (GPIB).

⁴Low noise DC voltage source: Yokogawa YK 7651.

⁵Provided from a lock-in amplifier: Stanford SR 830.

THE ORIGIN OF INSTABILITIES IN MR MEASUREMENTS

* * *

The observation of a gate dependent magneto-resistance in carbon nanotube quantum dots contacted by ferromagnetic leads in 2005 by S. Sahoo [4] demonstrated the possibility of an electrical control of spin transport. These devices paved the way for multi-functional spintronic devices. However, the implementation of ferromagnetic contacts in nanoelectronic devices has proven to be a challenging task due to the complex nature of ferromagnets and interfaces, where oxidation, surface roughness and mesoscopic details may induce uncontrolled instabilities in transport measurements.

For example, it turned out that palladium nickel (PdNi) contacts used in ref. [4] have, due to the formation of multi domains, unfavorable magnetic properties [68]. The preferred direction (magnetic easy axis) of the magnetization in narrow (~ 250 nm) and long (~ 5 μ m) PdNi strips is transverse to the strip, leading to less control over the coercive field H_C by a magnetic field applied parallel to the strip. In contrast recent experiments have shown that e-beam evaporated permalloy (Py, Ni₈₀Fe₂₀) strips with high aspect ratio provide due to the formation of single domains and the dominant shape anisotropy accurately controllable coercive fields with an easy axis along the strip [69, 66].

Though, the lack of reproducibility in MR measurements can not be solely explained by uncontrolled coercive fields. So-called single switches where only one conductance step occurs in a MR experiment. They lead to different conductances for the two parallel cases ($\uparrow\uparrow$ and $\downarrow\downarrow$) and are observed in many MR measurement on CNT QDs independently of the contact material (Co, Py, CoFe or Fe) and detection method,¹ see for example ref. [65, 70, 71, 3, 43, 72]. A possible mechanism for single switches could be a ferromagnetically pinned strip or the magneto coulomb effect [73, 3]. In addition, changes in the conductance unrelated to magnetic switching fields are observed.

In this thesis the origin of instabilities in MR measurements is traced back to magnetic particles in the case of e-beam evaporated Py and to metallic and magnetic flakes in the case of sputtered Py appearing during the fabrication process. A solution to this problem is found in an improved fabrication pro-

¹Two-terminal (local-) measurements like presented in this thesis or 4-terminal (non-local-) measurements where the current path is spatially separated from the spin-current.

cess for both deposition methods presented in this chapter.

The chapter is organized as follows: In the first section MR measurements on carbon nanotubes contacted with e-beam evaporated Py are presented and the need for an extended measurement scheme is motivated. In the second part several resist systems are introduced followed by the description of the optimized lithography process. The third section shows MR measurements on devices with sputtered Py and optimized lithography. The last part of this chapter reports on the improved sputter deposition process. MR measurements on devices with increased stability due to the fabrication with optimized recipe are discussed in chapter 5.

4.1 The Necessity for an Extended MR Measurement Scheme

The device for performing MR measurements presented in this chapter consists of two 25 nm thick Py contacts placed on a carbon nanotube as schematically illustrated in fig.4.1. The two contacts are 10 μm long, 200 nm and 400 nm wide and separated by 300 nm. For the fabrication of the two Py strips a 600 nm thick PMMA resist layer and an acceleration voltage of 30 kV is used for the lithography step and the metal deposition is done by e-beam evaporation (deposition rate $\sim 0.2 \text{ \AA/s}$). The characterization at RT obtained a two terminal resistance of $\sim 700 \text{ k}\Omega$.

For measurements at low temperatures of $\sim 230 \text{ mK}$ the starting point is always the electrical characterization of the quantum dot. In fig.4.2a the conductance G is plotted for a large backgate voltage V_{BG} interval showing a pronounced four-fold symmetry pattern. The observation of a four-fold pattern is a sign for a defect free carbon nanotube QD [74]. The almost perfect four-fold pattern can be seen more clearly in fig.4.2b where the spacing between two peaks is plotted in terms of addition energy, E_{add} as a function of V_{BG} . A regular pattern is visible where three data points with almost the

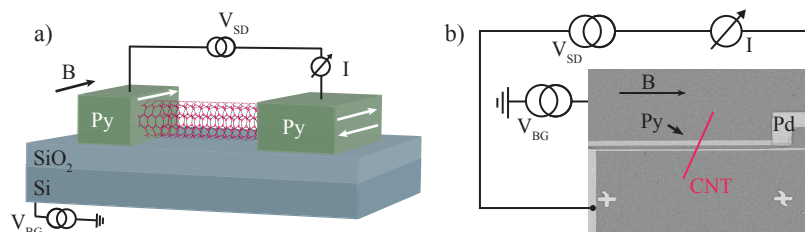


Figure 4.1: a) Schematic of a nanotube contacted by two 25 nm thick Py contacts. The contacts are 10 μm long and 200 nm/400 nm wide. For setting the magnetization an external magnetic field can be applied parallel to the strips. b) Scanning electron micrograph of a typical device with measurement set-up.

same addition energy of 4.1 meV, which is given by the charging energy U , are followed by one data point with significant larger addition energy $E_{add} \approx 6.9$ meV given by $E_{add} = \delta E + U$. From this one finds an energy level spacing of $\delta E = 2.8$ meV for the QD. Since the peak conductance $G \sim 10^{-3} e^2/h$ is quite low one can conclude an asymmetric coupling between Py contacts and QD. For completeness in fig.4.2c the energy stability diagram of the QD is plotted. The pattern of three small diamonds enclosed by two larger diamonds reflects again the four-fold symmetry. The height of the small diamonds refers to the charging energy and the height of the large ones to $\delta E + U$. The values obtained from the energy stability diagram matches the one extracted from fig.4.3b. Additional lines parallel to the slopes of the diamonds correspond to excited state transitions whereas the lines of the diamond itself correspond to ground states. Such stable (in time) QDs with very regular four-fold conductance pattern are the perfect basis for performing MR measurements.

The standard way to perform MR measurements is to tune the QD to the desired state by V_{BG} and measure the magnetic field B dependence of the conductance G at fixed backgate voltage V_{BG} . Here an extended measurement scheme is introduced where a Coulomb peak is mapped while sweeping the magnetic field.

For this, the conductance is measured as a function of the backgate voltage and the external magnetic field, resulting in two-dimensional color scale plots as shown in fig.4.3a for a magnetic field sweep from negative values to positive ones (up-sweep). The horizontal red/yellow line corresponds to one Coulomb resonance peak indicated as additional white line (vertical cross section of the conductance map) in the color plot. Increasing the magnetic field, starting from negative values, beyond $B = 0$ a first sharp change of the conductance

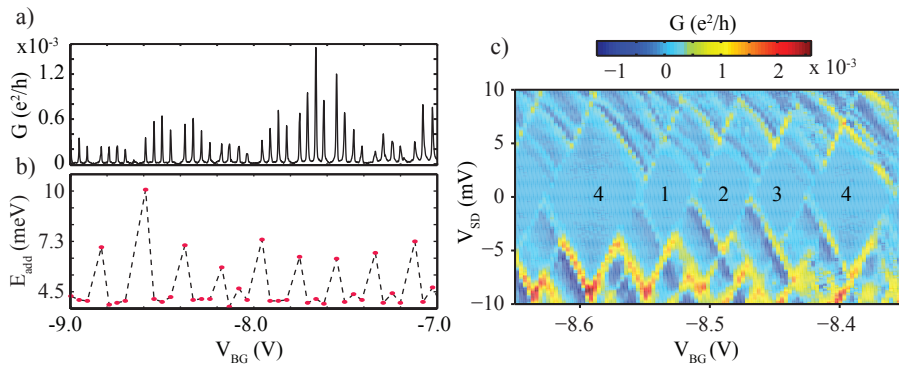


Figure 4.2: Electrical characterization of the QD measured at low temperature ~ 230 mK. a) Differential conductance G of the CNT as a function of V_{BG} a nice four-fold pattern is visible. b) The distance between two Coulomb peaks is plotted in terms of energy as function of V_{BG} . c) Energy stability diagram of the QD.

pattern occurs at $B_1 = 20$ mT followed by a second change at $B_2 = 30$ mT. Both magnetic fields B_1 and B_2 correspond to the expected coercive fields [66] for a 400 nm and 200 nm wide strip, respectively. At B_1 mainly two things happen: on the one hand, a large shift of the peak position by ~ 4 mV and on the other hand, an increase of the amplitude by almost a factor of 2. At B_2 the peak position shifts back roughly to the same position like for $B < B_1$ but the amplitude does not change back to the former value. For comparison with standard MR measurements two horizontal cross sections for slightly off-resonance backgate voltages, indicated by dashed lines, are plotted on top/below the main figure in fig.4.3a corresponding to magnetic field sweeps at fixed V_{BG} .

The shape of the curves are similar to measurements introduced in chapter 2.3. On one side of the resonance peak a positive MR of $\sim 70\%$ is observed and on the other side a negative MR of $\sim 80\%$. The MR step is almost solely caused by the large shift of the peak position. Sweeping the magnetic field from positive to negative values (down-sweep) the change of the conductance pattern is completely different and reflects the issue of instabilities in MR measurements, see fig. 4.3b. Only at one magnetic field $B_3 \approx 20$ mT, a significant change can be observed. The peak position shifts again, but the amplitude changes only slightly. In addition a change of the peak width takes place. Cross sections at the same backgate voltages like in fig.4.3a show a behavior of single switches and are again mainly caused by shifting the peak. Since the magnetic

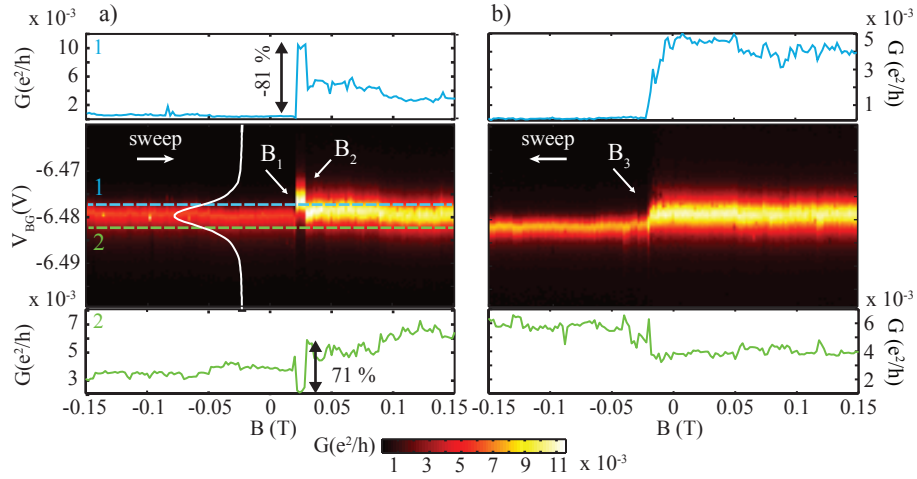


Figure 4.3: The differential conductance G is plotted as function of backgate voltage V_{BG} and external magnetic field B for increasing a) and decreasing b) magnetic field. The red/yellow horizontal line corresponds to one Coulomb peak indicated as additional white line (vertical cross section of the color plot). For comparison with conventional MR measurements horizontal cross section (dashed lines) are taken (top and bottom panel) corresponding to B -field sweeps at fixed gate voltage.

configuration can affect all characteristic features like position, amplitude and width of a Coulomb resonance peak in an irreproducible manner, it is highly recommended to perform MR measurements with an extended measurement scheme.

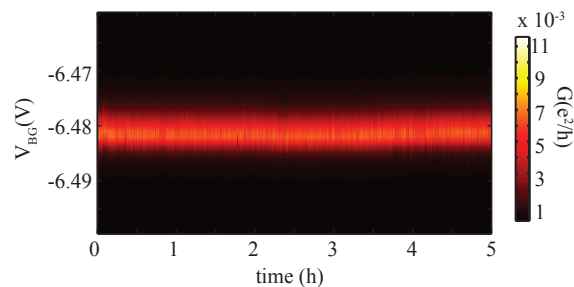


Figure 4.4: The same Coulomb resonance peak from fig.4.3 is mapped as function of time. Within five hours no gate jump or other instabilities could be detected and suggests a magnetic origin of the instabilities.

Measuring with the extended scheme is quite time consuming. For example the color plots in fig.4.3 took approximately 1 h each, which requires stable devices in time. Surface impurities on the SiO_2 substrate may cause gate-dependent or temporal charge rearrangements where the conductance may change abruptly. To exclude charge rearrangements in MR measurements the Coulomb peak in fig.4.3 is additionally mapped with zero applied magnetic field over a long time period. The measured result in fig.4.4 shows no instabilities within 5 hours. From this one can conclude that the instabilities are solely of magnetic origin. For tracing the origin of these instabilities the device is imaged by a scanning electron microscope (SEM).

In fig.4.5 the SEM picture of the investigated device is shown.² Two main features are noteworthy:

- A dark shaded area (black arrow) around and between the two Py strips corresponding to PMMA residues. The residues are identified by the lower contrast in the SEM image. These PMMA residues are primarily responsible for typical low yields of devices fulfilling the two terminal resistance criteria $R < 1 \text{ M}\Omega$ at RT.
- Small particles with large contrast are identified as metallic. These particles can be magnetic (e.g. Py) with uncontrollable behavior in an external magnetic field. Especially they are visible in the zoom-in

²In this SEM picture the secondary electrons are detected and not the backscattered electrons (BSE). A carbon nanotube is better visible in the SEM used in this thesis if one detects the BSE [75].

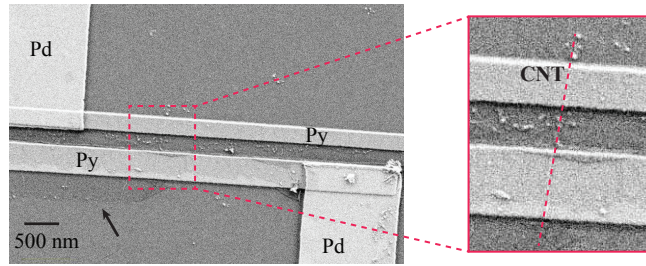


Figure 4.5: SEM picture of the measured device. Dark shaded areas (black arrow) are visible around and between the two Py strips corresponding to PMMA residuals. Additionally small bright Py particles are visible close to the CNT (red dashed line in the zoom in).

picture close to the carbon nanotube (marked as red dashed line) and may affect the MR measurements.

These fabrication problems can be avoided by optimizing of the fabrication process. The way to an optimized fabrication recipe is reported in the following section.

4.2 Optimized E-Beam Lithography

For the first devices fabricated during this project a resist layer structure consisting of a 100 nm PMMA/MA³ layer and a 200 nm PMMA⁴ layer was used for the e-beam lithography step following the recipe from [66]. For the lithography an acceleration voltage of 20 kV and an aperture of 10 μm was used and the Py was deposited via e-beam evaporation. The yield of devices with a two-terminal resistance at RT was very low $< 5\%$ and none of these devices worked at low temperature. The reason for this low yield may be polymer resist residuals. This problem was already mentioned in an earlier PhD project [43]. In general this is a well known issue from semiconductor technologies and can in principle be solved by an oxygen plasma ash or by UV-ozon cleaning [76]. Another possibility to remove the resist residuals is an argon-plasma etch step before the metallization, see fig.4.6. However all of these cleaning procedures can damage or even remove the carbon nanotube as well, for example no intermediate argon plasma etch rate could be found for removing the residuals while the CNT stays alive.

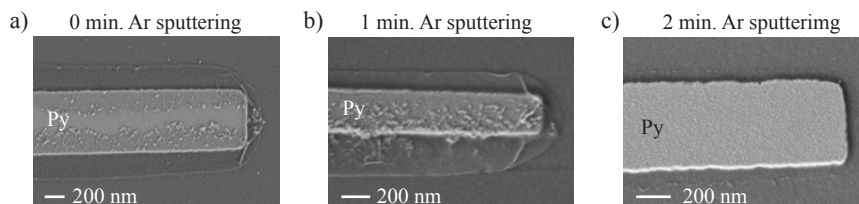


Figure 4.6: SEM pictures of fabricated Py test strips where an additional argon plasma etch step was done before the metal deposition.

For solving this problem one approach was the use of a single PMMA layer and to try different thicknesses, acceleration voltages and apertures [43]. In fig.4.7a) the result of a Py strip fabricated with 600 nm PMMA, 30kV acceleration voltage and 30 μm aperture is shown. No residuals and disturbing magnetic particles are visible.

Therefore, a sample batch following this recipe was fabricated. Measurements on the resulting device are presented in the previous section 4.1. Obviously from the SEM picture of this device (fig.4.5) the Py strips are not as clean as predicted from the test strip in fig.4.7. It is assumed that this test was a lucky shot due to a coincident overexposure of the resist in a non-reproducible manner. It is known that an overexposure may reduce residuals [77]. Since the fabrication of the "real" device could not reproduce clean Py strips further resist studies were performed.⁵ For this another test sample following the same recipe was fabricated, dipped in liquid nitrogen (for a better breaking

³PMMA/MA = polymethyl methacrylat-methacrylic, AR-P 617 33 %, Allresist.

⁴PMMA = ployethyl methacrylat 671.09 950 K, Allresist, diluted in chlorbenzene.

⁵Done by a team colleague: Jörg Gramich.

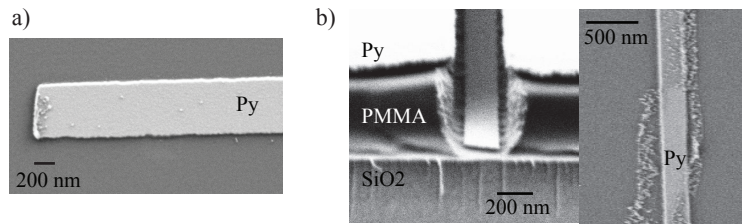


Figure 4.7: SEM picture of a test Py strip fabricated by using 600 nm PMMA, 30 kV acceleration voltage and $30\mu\text{m}$. No resist residuals and disturbing Py particles are visible. b) SEM pictures: tilted side view of a test Py strip after metal deposition and of the resulting Py strip after lift-off fabricated with the same recipe like in a). The undercut is V-shaped leading to a deposition of material on the side walls and resulting in a bad lift-off.

edge) and cleaved into two pieces after the metal deposition. This allows for a tilted side view of the resist profile, see fig.4.7b. Due to the high acceleration voltage the undercut profile of the resist is V-shaped which supports a metal deposition on the side walls as well leading to remaining disturbing particles next to the Py strip after lift-off. In addition, residuals from the resist are still visible. It is possible to improve the resist profile by lowering the acceleration voltage, but the issue of resist residuals remains.

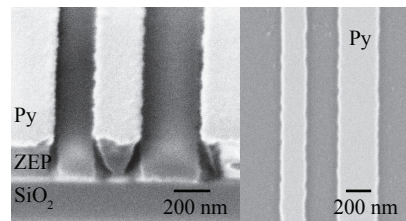


Figure 4.8: Side view of the ZEP resist profile after metal deposition. An almost perfect undercut is visible. The Py strip after the lift-off is well defined and no disturbing magnetic particles and resist residuals are visible.

The use of the high-sensitive copolymer ZEP 520A (ZEP)⁶[78] as resist brought the solution. Here a 300 nm ZEP resist layer, an acceleration voltage of 10 kV and a typical dose of $\sim 34 \mu\text{C}$ is used for the lithography. A 60 s development took place in n-Amylacetate, stopped in a 9:1 solution of MIBK an IPA and finally rinsed in pure IPA. After the metallization the lift-off is done in a 70°C hot NMP⁷ bath. Fig.4.8 shows the test result for this recipe. An almost perfect undercut profile is visible with a narrow opening at the top of the resist film and clean residual free Py strips can be obtained. For devices fabricated

⁶ZEP, composed of 11% methyl styrene and chloromethyl acrylate copolymer, solved in 89% anisol, ZEON corporation.

⁷NMP = n-mythyl-2-pyrrolidone

with the new recipe a significantly increased contact resistance yield could be observed. 50% of these devices fulfill the RT criteria of a two-terminal resistance $R < 1 \text{ M}\Omega$.

4.3 MR Measurements on Devices with Sputtered Py Strips

Parallel to the e-beam lithography optimization a new UHV magnetron sputter machine⁸ was launched. The physical vapor deposition (PVD) method of depositing thin films of the desired material (target) by sputtering provides a much higher degree of versatility in comparison to e-beam evaporation. Sputtering is in principle a bombardment of the target with ions provided by a plasma (e.g an argon plasma). An incident ion initiates a collision cascade inside the target and when this cascade reaches back to the surfaces with a kinetic energy larger than the surface binding energy an atom can leave the target. The main advantages of sputter deposition are:

- Deposition of materials with very high melting points, e.g niobium.
- Stoichiometric deposition of multicomponent materials.
- Better adhesion due to larger kinetic energies ~ 2 eV on the substrate.
- No hot parts at the sputtering source (water cooling).
- Compatible with reactive gases like oxygen or nitrogen.
- Easy access for fabricating multilayer systems like ferromagnetic exchange bias layers or synthetic antiferromagnets (SAF).

The drawback of sputter deposition is the difficulty of combining with lift-off technique since the material transport from target to sample is due to the argon gas pressure less directional. Another disadvantage may be the large kinetic energies of the deposited material since this can damage delicate substrate materials. For example it is known that sputter deposition on graphene causes disorder in the graphene sheet [79].

Since the new fabrication recipe introduced in the previous section was developed in parallel first devices with sputtered Py strips where fabricated following the new recipe for the e-beam lithography step. A device (sample # 2) with two Py contacts (200nm and 400 nm width) separated by 300 nm was designed. For the sputter deposition step an argon pressure of 5 mTorr and a power of 35 W was used. It has to be mentioned that the sputter machine used for the deposition provides 7 sputter sources arranged in a circle while the sample holder is placed above the sources but in the center of this circle. This implies a large angle $\sim 40^\circ$ between sputter gun and device. The deposition of ferromagnetic materials under an incident angle induces a magnetic

⁸Commercially available Orion-8-UHV, AJA, USA.

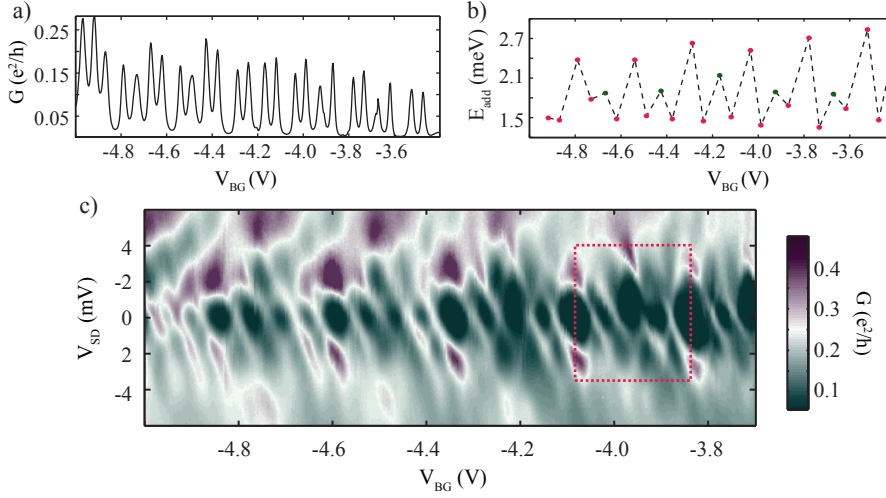


Figure 4.9: Electrical characterization of the CNT QD with sputtered Py contacts. a) Backgate V_{BG} sweep of the conductance G . A four-fold periodicity superimposed by a two-fold symmetry is visible. b) The addition energy E_{add} as a function of V_{BG} . The energy for the second electron (green data points) exceeds those for the first and third electron. c) Energy stability diagram. The highlighted package of four Coulomb resonances is chosen for MR measurements.

anisotropy axis [80]. For avoiding this the sample was rotated while sputtering.

The device yield fulfilling the RT criteria of a two terminal resistance below $1 \text{ M}\Omega$ increased slightly in comparison to devices fabricated with e-beam evaporation. A device with $40 \text{ k}\Omega$ at RT was cooled down to 1.5 K for spin transport measurements. The electrical characterization of the QD is plotted in fig.4.9a. The Coulomb peaks oscillate with a 4-fold periodicity. In contrast to the data from fig.4.2 the four-fold pattern is superimposed by a two-fold periodicity. This means that the four-fold degeneracy of the QD energy levels is slightly lifted with an energy separation of $\sim 0.4 \text{ meV}$. This can be read from fig.4.9b where the addition energy is plotted a function of backgate voltage. This generally observed behavior [81, 74, 82, 83, 84] may be caused by a disorder induced coupling of the K, K' states [82, 85] leading to a splitting by $\Delta_{KK'}$ of the energy spectrum into two spin-degenerate orbitals. Another possibility for lifting the energy degeneracy is the recently observed spin orbit coupling Δ_{SO} induced by the curvature of the CNT [86, 87]. Both mechanism may be present leading to a total splitting of $\Delta = \sqrt{\Delta_{KK'}^2 + \Delta_{SO}^2}$.

However, for MR measurements a package of four resonances indicated in fig.4.2c as red rectangular is chosen. The result for the magnetic field sweep (up and down) mapping these four peaks is shown in fig.4.10. Again, like in the MR data from the previous device (fig.4.3) the measurement is dominated

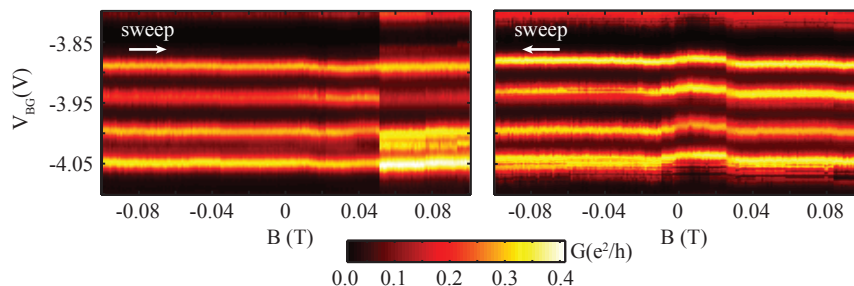


Figure 4.10: MR color map for four Coulomb peaks. Like in the MR measurements from section 4.1 the conductance pattern is dominated by random changes.

by random changes of amplitude, peak position and peak width. In addition the significant changes of the conductance pattern take place at magnetic fields which do not correlate with the expected coercive fields for 200 nm and 400 nm wide Py strips [66].

Therefore anisotropy magneto-resistance (AMR) measurements on these two strips were performed to determine their coercive fields. AMR is an effect which causes a resistance dependence on the orientation of the magnetization of a ferromagnetic material relative to the direction of the current due to the interplay of magnetization and spin orbit interaction [88, 89].

For this the two terminal resistance R of a single Py strip is measured as a function of the magnetic field applied parallel to the strip. This is schematically illustrated in the SEM picture of the device, see fig.4.11a. When sweeping the magnetic field and reaching the coercive field of such a Py strip the magnetization of the strip changes abruptly by 180° . Since the magnetic field is never perfectly aligned with the strip axis the magnetization of the strip does not change in one 180° step and is usually for a short moment during the switching perpendicular to the current direction resulting in a small resistance change. Therefore AMR measurements are the perfect tool to state the coercive field of single Py strips. The results of these measurements from the 400 nm wide and 200 nm wide strip are plotted in fig.4.11c and fig.4.11d respectively. The up and down sweep for the 400 nm wide strip results in a resistance change asymmetric around zero magnetic field. This is caused by a 4 mT offset of the magnet. Taking this into account one finds a coercive field of ± 10 mT well matched with values obtained in ref.[66] for a 400 nm wide strip. In contrast the 200 nm wide strip switches in a non reproducible manner. Two up/down sweeps are plotted taken one after another with completely different shapes. A closer look at the SEM picture (fig.4.11a) of the measured device sheds light on this issue.

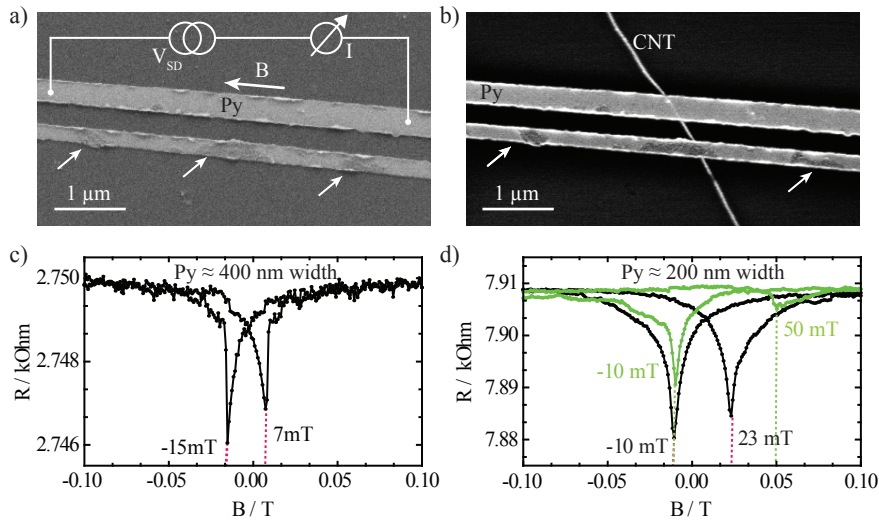


Figure 4.11: a) SEM image (secondary electrons) of the device with an illustration of the measurement scheme for AMR measurements. In addition large Py flakes are visible lying on top of the narrow strip (white arrows). b) The same SEM picture (backscattered electrons). AMR measurements of the 400 nm wide c) and the 200 nm wide d) Py strip.

In fig.4.11b the same device is shown but for making the carbon nanotube visible an SEM image of the backscattered electrons is shown instead of an image of the secondary electrons. In both images one can see large flakes consisting of Py (indicated with white arrows) lying on top of the narrow Py strip while the wide Py strip looks much cleaner. Together with the AMR measurements one can conclude that these flakes affect the magnetic properties of the narrow Py strip. In some devices one could also observe flakes lying on top of the nanotube. For tracing back the origin of these flakes a test sample was fabricated, dipped in liquid nitrogen and cleaved after the metal deposition to look at the undercut profile, see fig. 4.12a. Not surprisingly the undercut is due to the less directional sputter deposition completely filled with the deposited Py including a Py deposition on the sidewalls of the resist layer. In fig.4.12b the corresponding Py strip after lift-off is shown. The edges

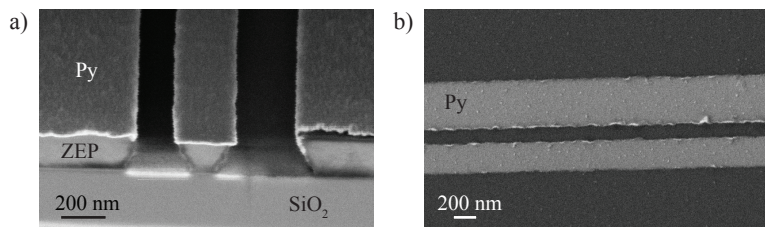


Figure 4.12: SEM image for test devices with Py deposited via sputtering a) side view before lift-off. b) The Py strips after lift-off.

of the strips are very rough and partly small flakes are visible. The filling of the undercut with the deposited Py makes the lift-off not reproducible. A worst case scenario is shown in fig.4.13. Here massive Py flakes are standing perpendicular to the strip with a height of ≈ 300 nm corresponding to the resist thickness.

In the following section an optimized sputter deposition process is reported.

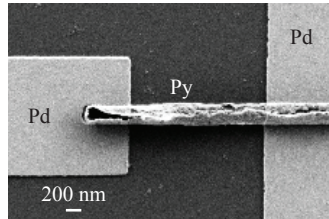


Figure 4.13: SEM image of a worst case scenario of a failed lift-off.

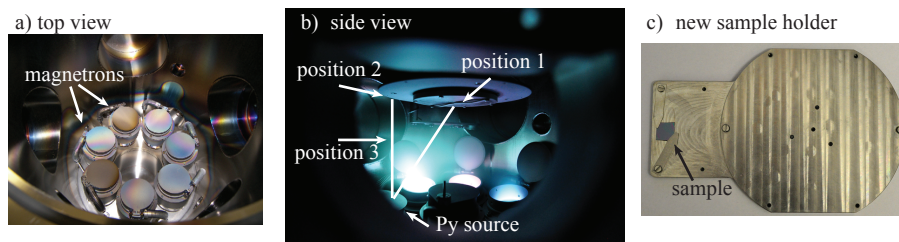


Figure 4.14: a) Top view of the sputter chamber. b) Side view of the sputter chamber. 3 different positions for locating the sample are indicated. c) The new sample holder with an additional side arm

4.4 Optimized UHV Magnetron Sputter Deposition

For optimizing the sputter deposition it is reasonable to have a closer look at the sputter machine used for the deposition. In fig.4.14 a top view of the inside of the sputter chamber is shown. 7 magnetron sputter sources are arranged in a circle. The sample holder is mounted above the sources in the center of this circle. Labeled as position 1 in fig.4.14 which shows a side view of the chamber. For this situation the material deposited at the sample arrives under an angle of $\sim 40^\circ$. The possibility of rotating the sample holder may compensate the deposition at an angle of incidence. In addition the platform where the sample holder is mounted can be moved up and down. For more versatility a new sample holder was built with an additional side arm to have the possibility for localizing the sample vertically aligned to the sputter source, see fig.4.14c.

For optimizing the sputter deposition process cross sections of test strips, fabricated with different sputter parameters at 3 distinct sample positions indicated in fig.4.14c, are investigated.

Position 1

At position 1 three different test samples were fabricated:

- Ar pressure: 5 mTorr, Ar gas flow: 35 sccm, power: 35 W, rotating the sample (parameters from the measured device in the previous section).
- Ar pressure: 0.7 mTorr, Ar gas flow: 23 sccm, power 50 W, rotating the sample. This was the lowest achievable pressure.
- Ar pressure: 0.7 mTorr, Ar gas flow: 23 sccm, power 50 W.

The first idea tried out was lowering the argon pressure to reduce scattering events of the deposited material with gas particles on the way from target to sample. By reducing the Ar gas flow from 35 sccm to 23 sccm and increasing the power from 35 W to 50 W an Ar pressure of 0.7 mTorr with stable plasma

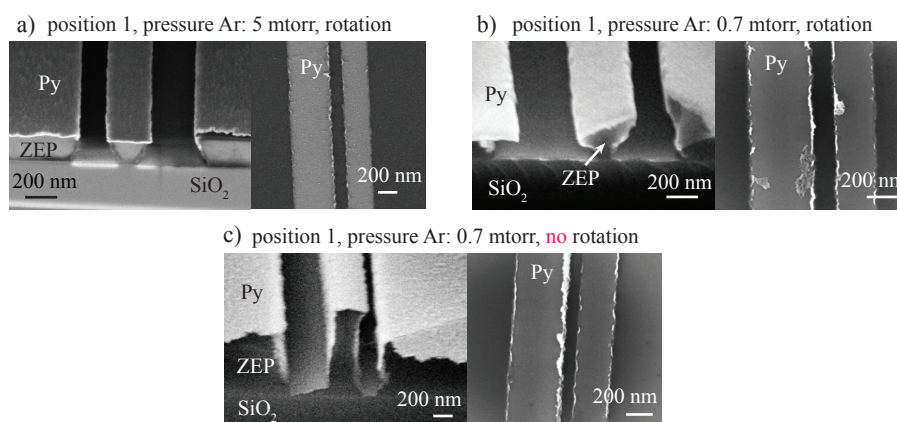


Figure 4.15: Sputter test for position 1. SEM pictures of cross section before lift-off and SEM pictures of test strips after lift-off. The Py strips are fabricated with different parameters, indicated at each SEM picture. In all cases the undercut is filled with deposited material leading to rough edges of the Py strip and a contamination with Py flakes coming from the sidewalls of the resist.

could be achieved. For the deposition of ferromagnetic materials it is crucial not to induce an unwanted magnetic easy axis. Therefore the sample was rotated during the deposition. The result is shown in fig.4.15b. The undercut is still completely filled with deposited Py resulting in Py strips contaminated with flakes. For a test sample with the same low pressure parameters but switched off rotation the same result was observed, see fig.4.15c. With the new sample holder the possibility arises to place the sample on top of the Py magnetron source for avoiding a deposition under an angle (position 2). In first place the distance between sample and sputter source was chosen as large as possible ~ 20 cm because of the fear to destroy the carbon nanotube.

Position 2

For sputter test at position 2 two test samples with different sputter parameters were fabricated:

- Ar pressure: 5 mTorr, Ar gas flow: 35 sccm, power: 35 W.
- Ar pressure: 0.7 mTorr, Ar gas flow: 23 sccm, power 50 W.

The results are shown in fig.4.16. For 5 mTorr argon pressure the undercut is completely filled and the Py strip exhibit rough edges with additional flakes. Additionally one can see in the zoom in that the grown film is less uniform and the Py forms columns. It is hard to say, if this is a consequence of the position and the sputter parameters used since the resolution in most of the SEM pictures is due to charging up of the resist not high enough. In general the uniformity of a thin film depends strongly on the sputter parameters

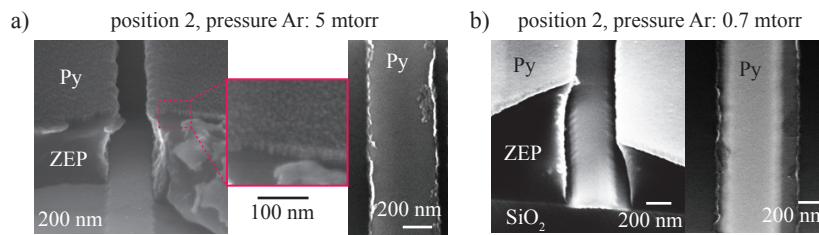


Figure 4.16: Results for position 2. a) For 5 mTorr Ar pressure the undercut is still completely filled resulting in bad Py strips after lift-off. Zoom-in: The deposited Py does not form a uniform film but grows with a column texture. b) Sputtering with an Ar pressure of 0.7 mTorr shows a first improvement since the major deposited material fill the undercut only partly. But still a small amount of Py fills the undercut

[90]. The columns develop due to a self-shadowing effect where the incoming atoms are captured by atoms already incorporated into the deposited material [91, 92]. The formation of columns may cause an increase of the resistivity. Additionally they may induce due to shape anisotropy a perpendicular easy axis when the deposited material reaches a finite thickness. For example rotating the sample, while sputtering, reduces this self-shadowing effect [93, 91]. The test strip fabricated with an argon pressure of 0.7 mTorr yields first improvements. In fig.4.16b most of the deposited material fills the undercut only partly corresponding to the size of the opening at the top of the resist layer. But still a small amount of Py fills the whole undercut. The Py strip after lift-off reflects this behavior. A thick well defined Py strip is visible with thinner material deposited at the edges. The final test step is a decrease of the distance between sample and sputter source.

Position 3

The following sputter parameters were used for fabricating the last batch of test samples:

- Ar pressure: 5 mTorr, Ar gas flow: 35 sccm, power: 35 W.
- Ar pressure: 2 mTorr, Ar gas flow: 35 sccm, power: 35 W.
- Ar pressure: 0.7 mTorr, Ar gas flow: 23 sccm, power 50 W.

A significant improvement of the Py strip could be achieved by decreasing the distance between sample and sputter source from ~ 20 cm to ~ 10 cm. In fig.4.17 one can see well defined Py strips for argon pressures of 5 mTorr and 2 mTorr. The widths of the resulting strips are still slightly wider than the opening of the resist and for achieving Py strips with 200 nm and 400 nm width one has to design 180 nm and 350 nm wide strips respectively. In addition only parts of the deposited material reaches the bottom of the resist

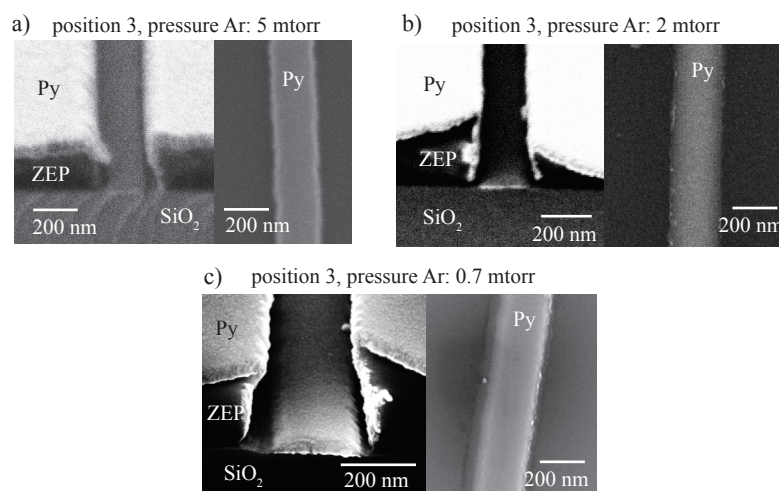


Figure 4.17: Sputtering at position 3 where the sample is placed 10 cm above the sputter source a significant improvement of the fabricated Py films is achieved. a) For an argon pressure of 5 mTorr a well defined Py strip is the result. b) As well for 2 mTorr. c) The result for 0.7 mTorr.

trench, and for fabricating a 200 nm wide strip of 25 nm thickness one has to deposit a 60 nm thick film. The thickness depends on the width of the strip and depositing 60 nm of Py gives a thickness of 30 nm for a 400 nm wide strip. Another feature observed is that the incoming material deposits preferentially at the edge of the resist opening which shrinks the width of this opening during the Py position. Therefore the Py strip has no longer a perfect rectangular shape but rounded edges. This is for example visible in fig.4.17c. For an argon pressure of 0.7 mTorr the Py deposits at the bottom of the trench are slightly asymmetric with respect to the undercut. This leads to a connection between strip and the right side wall and to a small amount of deposited material beside the main strip on the left side of the strip. This results in a rough edge on the right side of the Py strip and a very smooth left side after the lift-off. The positioning of the sample on top of the sputter source is done with limited precision based on visual judgment only. This misalignment probably causes the asymmetric deposition of the Py for 0.7 mTorr argon pressure.

However sputter parameters for well defined and clean Py strips were found. The Py strips are of the same visual quality like Py strips fabricated with e-beam evaporation. For further fabrications of "real" samples where a nanotube is connected with two Py strips an argon pressure of 5 mTorr and a power of 35 W is chosen for the sputter deposition. Before going on with MR measurements on hast to verify that the visual improvement of the Py strips goes along with an improvement of the magnetic properties. Especially for the narrow 200 nm wide strip. For this AMR measurements are performed.

In fig.4.18 the result of an AMR measurement for an 200 nm wide strip is plotted and a coercive field B_C of ± 40 mT is found. For comparison with e-beam evaporated Py strips the measured coercive fields are plotted in fig.4.18 as a function of the strip width for Py strips fabricated with different recipes. From this plot one can conclude that Py strips fabricated with optimized sputter deposition (red data points) are of the same high magnetic quality as strips fabricated via e-beam evaporation (black⁹ and blue¹⁰ data points). Py strips fabricated with the not optimized sputter parameters (green data points) show significant lower coercive fields.

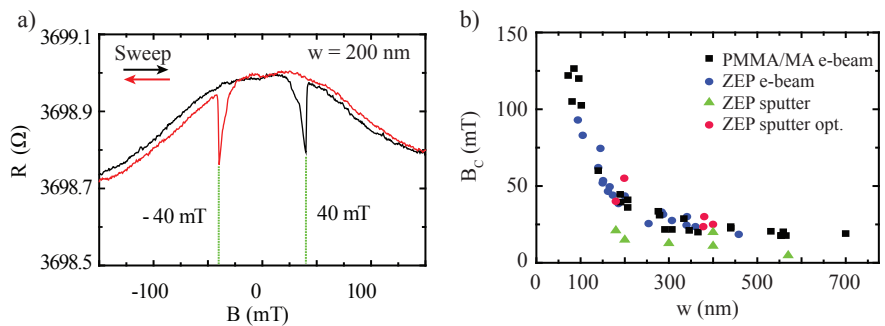


Figure 4.18: a) AMR measurement for a 200 nm wide Py strip. A coercive field of ± 40 mT can be extracted. b) Coercive field B_C as a function of strip width for Py strips fabricated with different recipes. Py strips fabricated with optimized sputter parameters exhibit the same high degree of control over the coercive field by the width of the strip.

⁹from [66]

¹⁰Done by Jörg Gramich

MR EXPERIMENTS ON STABLE DEVICES

* * *

The gate-dependence of the MR in carbon nanotube QDs [4], especially the observation of negative MR values, is not fully understood so far. Theoretical models [56, 54] based on an effective Zeemann splitting of the QD energy levels, predict major contributions to the MR from shifts of the Coulomb peaks. Taking into account the four-fold degeneracy of each energy level, both models predict a $\text{MR}(V_{BG})$ pattern dependent on the occupation of the dot. MR measurements on devices exhibiting a clear four-fold conductance pattern have not been reported up to now.

MR measurements suffer mainly from a lack of reproducibility. Some irreproducibilities in the MR could be traced back in chapter 4 to disturbing magnetic particles or flakes appearing during the fabrication process. In devices fabricated based on the optimized recipe reported in chapter 4, improved reproducibility and magnetic and electrical contact properties could be achieved. This chapter discusses MR measurements on two independently fabricated stable devices which exhibit a clear four-fold periodicity. These measurements seem not to be compatible with the theoretical models reported in ref. [56, 54].

5.1 Negative Magneto Resistance over Set of Four Coulomb Peaks

The first device presented in this chapter is fabricated following the optimized recipe (see chapter 4) with sputtered ($p_{Ar} = 0.5$ mTorr. $P = 35$ W) Py for the ferromagnetic electrodes. For this device a two-terminal resistance of 50 $k\Omega$ was obtained at RT. The differential conductance G measured as a function of backgate voltage V_{BG} at low temperature (~ 230 mK) is plotted in fig.5.1a. The Coulomb blockade oscillations and the corresponding distances between two peaks in terms of energy, plotted in fig.5.1b, as a function of backgate voltage V_{BG} show a clear four-fold periodicity consistent with the spin and valley degeneracy. The four-fold degeneracy is slightly lifted by $\Delta = 0.9$ meV. From the energy stability diagram shown in fig.5.1c one can extract the following parameters:

- Lever arm of the backgate to the QD $\alpha = 0.14$
- Charging energy $U \sim 4.5$ meV.
- Level spacing $\delta E \sim 4$ meV.

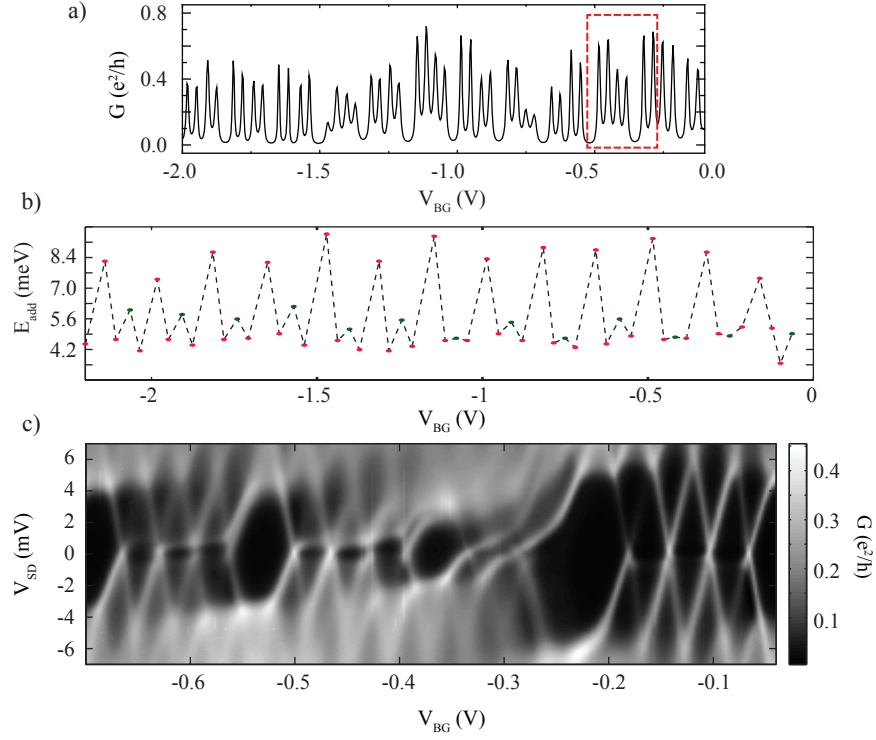


Figure 5.1: Electrical characterization of the carbon nanotube quantum dot formed at low temperature ~ 230 mK. a) The conductance G of the QD spin valve is plotted as a function of backgate V_{BG} . A clear four-fold periodicity is visible reflecting the spin and orbital degeneracy of the QD energy levels. b) The distance between two corresponding peaks in a) is plotted in terms of energy levels versus backgate. c) Energy stability diagram of the QD.

- Source capacitance $C_S \approx 23.6$ aF.
- Drain capacitance $C_D \approx 6.3$ aF.
- Backgate capacitance $C_{BG} \approx 4.9$ aF

The average width of the Coulomb peaks is $\Gamma \sim 2.4$ meV which is much larger than the broadening by temperature (for $T = 230$ mK ~ 0.02 meV). From this one can assume a lifetime broadening of the QD energy levels dominated by the coupling to the contacts. This ($k_B T \ll \Gamma$) allows for a description of the intrinsic line shape of such a QD resonance by:

$$G_i = G_{max}^{(i)} \frac{\Gamma_i^2}{(E - E_i)^2 + \frac{\Gamma_i^2}{4}}. \quad (5.1)$$

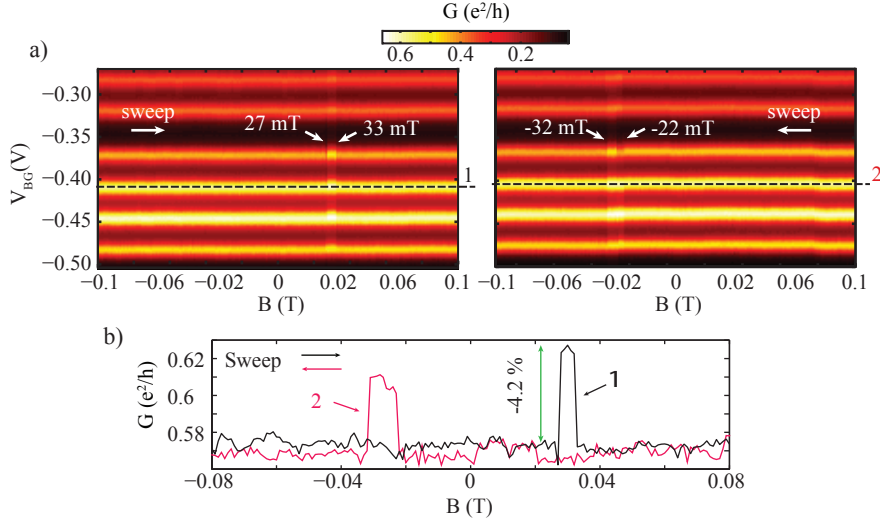


Figure 5.2: a) Conductance G as a function of backgate voltage V_{BG} and external magnetic field B . Clear conductance variations are visible in the up (left) and down (right) sweep at magnetic fields corresponding to the coercive field of the Py strips. b) Horizontal cross sections at fixed backgate from the conductance maps (indicated by dashed lines). Sharp switchings occur at the coercive fields of the Py strips and lead to a negative MR $\sim -4\%$.

$E - E_i \propto \alpha \Delta V_{BG}$ describes the detuning of the Coulomb peak position. For a four-fold degenerate CNT the maximum of a conductance peak is given by

$$G_{max} = \frac{4e^2}{h} \frac{\Gamma_S \Gamma_D}{(\Gamma_S + \Gamma_D)^2}. \quad (5.2)$$

From this one finds a maximum of the conductance peak $G_{max} \sim 0.5 \frac{e^2}{h}$ and the tunnel couplings¹ to source $\Gamma_S \approx 2.0$ meV a drain $\Gamma_D \approx 0.4$ meV, which gives a quite symmetric tunnel coupling $\frac{\Gamma_S}{\Gamma_D} \approx 5$.

For the MR measurements a set of four peaks is chosen indicated with a red rectangle in fig.5.1a. The conductance G is mapped as a function of backgate voltage and external magnetic field applied parallel to the Py strip and plotted in fig.5.2a. The two color plots refer to up sweep (increasing B field from negative values) and down sweep (decreasing B field from positive values). Each yellow/red horizontal line corresponds to one Coulomb resonance peak. On top of these lines one can see intensity variations in the magnetic field range where it is expected (from AMR measurements) that the magnetic strips switch their magnetization. In the up sweep an increase of the conductance G occurs at $B = 27$ mT and when reaching $B = 33$ mT the conductance changes back to the original value. This small field range $27 \leq B \leq 33$ mT is identified as the antiparallel magnetic configuration. In the down sweep

¹The larger value is chosen as Γ_S .

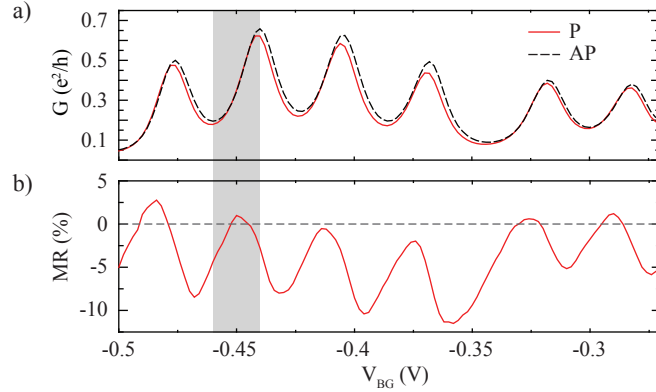


Figure 5.3: a) Conductance G as a function of backgate voltage V_{BG} for parallel (red solid line) and antiparallel (black dashed line) magnetic configuration. b) Corresponding MR. The MR oscillates with the backgate voltage.

the change of the conductance to larger values occurs at $-32 \leq B \leq -22$ mT. Almost no additional features, like random shifts or changes in the conductance are visible. For comparison with the common way for performing MR measurements where the magnetic field is swept up and down for fixed backgate voltage horizontal cross sections in the color plot (indicated as by dashed lines) are plotted in fig.5.2b. Sharp switches of the conductance at the coercive fields of the Py strips are visible. The change of the conductance between parallel and antiparallel magnetic configuration corresponds to a negative MR of $\sim -4\%$.

The amplitude, position and width of the conductance feature in such devices can depend on the magnetic configuration. For further analysis vertical cross sections are taken from fig.5.2a. Two of them taken at -80 mT (parallel configuration P) and 29 mT (antiparallel configuration AP) are plotted in fig.5.3a. The two curves differ significantly. Higher amplitudes for the antiparallel case are visible and in addition the peak positions are slightly shifted with respect to each other. In fig.5.3b the corresponding MR is plotted as a function of backgate voltage V_{BG} . The MR oscillates with the backgate voltage. Maxima in the MR occur at the left slopes of each Coulomb peak and minima at the right slopes, which is a strong indication for a MR mainly caused by the shift of the peak positions.

For a quantitative analysis the data are fitted by multiple Lorentzians (eg. 5.1). This allows for extracting the amplitude, peak position and width of each peak. As an example, the fit (orange solid line) for one conductance curve of the AP configuration (dashed line) is plotted in fig.5.4a. Each Lorentzian is plotted as green line. The results are shown (of the third peak highlighted

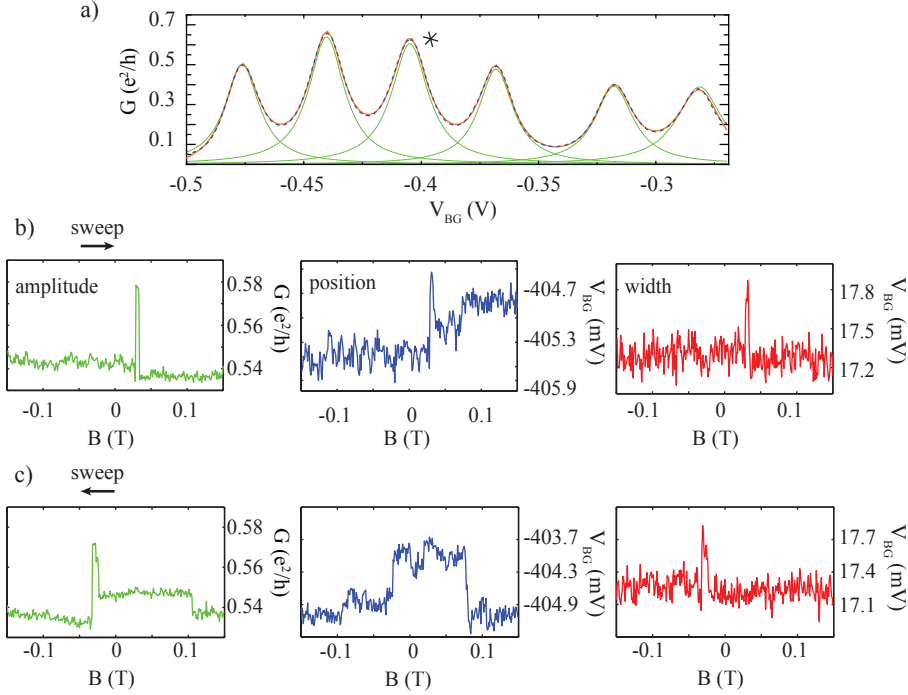


Figure 5.4: a) The conductance G for the antiparallel configuration as a function of backgate voltage V is fitted with multiple Lorentzian. The sum (orange line) over these six Lorentzian is well matched with the data. Each single Lorentzian is plotted as green lines in addition. This allows for extracting the amplitude, peak position and width of each Coulomb peak. The Results of the extracted parameters for the third peak highlighted with an asterisk are plotted as a function of magnetic field B for the up sweep b) and the down sweep c). Similar results for the other peaks are obtained and can be found in appendix B.

by an asterisk) for the amplitude, peak position and peak width as a function of magnetic field in fig.5.4b for the up sweep and in fig.5.4c for the down sweep.

The results for all other peaks can be found in appendix B. The amplitude increases in both sweeps for the antiparallel magnetic configuration by $\sim 4\%$ relative to the parallel one. The peak position shifts about 1.0 mV ($\sim 140\mu\text{eV}$) which is $\sim 6\%$ of the peak width. In the down sweep an instability is visible at $B \approx 100$ mT affecting the amplitude and at $B \approx 80$ mT the peak position. These small additional features could come from charge rearrangements. In contrast the width of the peak is not affected by instabilities and shows solely an increased value of 4.5% in the antiparallel configuration. Similar behaviors could be found for all other peaks as well (see appendix B). The peaks are all shifted by the same value within experimental errors.

This allows for investigating the respective impact on the MR by correcting the relative shift of the conductances curves between parallel and antiparallel

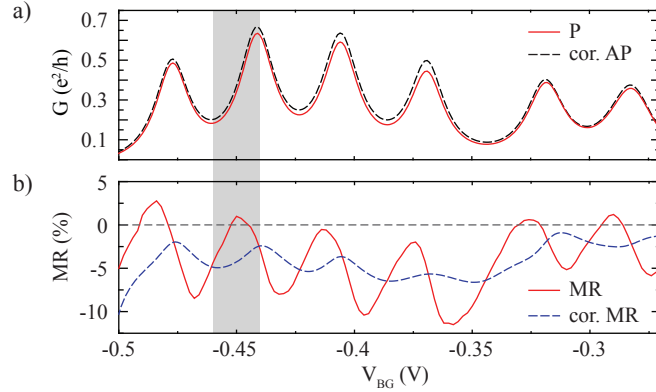


Figure 5.5: a) Conductance G as function of backgate voltage V_{BG} for the measured conductance in the parallel configuration (red line) and the for the shift corrected conductance in the antiparallel configuration (black dashed line). b) Magneto-resistance for the original case (red line) and the corrected case (blue dashed line).

alignment of the Py strips. In fig.5.5a the original conductance curve for the parallel alignment and the shift-corrected curve for the antiparallel alignment are plotted. From this one can calculate the corrected MR shown in fig.5.5b as blue dashed line, together with the original MR for comparison. The corrected MR exhibits a remaining modulation of 3% and maxima occur at backgate voltages corresponding to the Coulomb peak maxima. The remaining modulation can tentatively be attributed to changes in widths of the peaks for parallel and antiparallel configuration. In addition, the resulting MR is negative for all backgate voltages in contrast to the standard TMR picture.

The observation of a global shift of the Coulomb peak positions and a complete negative MR over a set of four peaks is in contradiction to the two existing theories introduced in chapter 2.3. An effective Zeeman splitting of the energy levels of any origin would lead to energy shifts of pairs of Coulomb peaks, each with opposite directions. In addition these models predict that the amplitudes dependent on the occupation of the dot and can lead either to an increased or decreased amplitude when the magnetic configuration changes from parallel to antiparallel. It has to be mentioned that the assumed regimes of the QD in both theories differ from the regime of the QD presented here. In particular, in ref.[56] the assumed tunnel rates $\Gamma_S = 0.0725U$ and $\Gamma_D = 0.0043U$ are much lower than the observed tunnel rates of $\Gamma_S = 0.4U$ and $\Gamma_D = 0.09U$ for the QD in this thesis. Due to the weak tunnel coupling in this work, higher order tunnel processes are neglected. In ref.[54] similar small tunnel couplings are assumed and a thermal broadening is assumed.

A global shift in the antiparallel configuration could be caused by another mechanism: the magneto-Coulomb effect (MCE) [94, 73, 95]. The MCE de-

scribes a situation where the density of states at the Fermi energy for spin up and spin down electrons in the ferromagnetic contacts is shifted by the Zeeman energy $\Delta E_Z = \pm \frac{1}{2}g\mu_B B$ caused by an external magnetic field. Since the number of total electrons has to stay constant the electrons rearrange between the two spin subbands, leading to a change of the electrochemical potential $\Delta\mu$. In the case of a ferromagnet capacitively coupled to a small island like a QD, this change in the electrochemical potential induces an additional charge onto the QD and acts like an additional gate, resulting into a shift of the Coulomb peak positions. This gating effect has to be compensated by the backgate voltage ΔV_{BG} . This shift in an external magnetic field can be described by

$$\Delta V_{BG} = \frac{1}{2e} \frac{C_S + C_D}{C_{BG}} P g \mu_B B. \quad (5.3)$$

Since the slope of the shifts depend on the magnetic configuration additional step like changes are expected when changing the orientation. For estimating the MCE shift in the presented device a polarization of $P = 0.8$ of the ferromagnet is used as an upper limit. The Landé g-factor is 2.1 for thick (> 15 nm) Py films [96]. With the data obtained above on source, drain and backgate capacitances one obtains a MCE shift of $\Delta V_{BG}/B \approx 300 \mu\text{V}/\text{T}$. This negligible slope of the peak position is consistent with the one observed in fig.5.4b. Sweeping the magnetic field beyond both coercive fields of the two Py strips connected to the QD a total change in position of $\Delta V_{BG} = 15 \mu\text{V}$ would be expected by the MCE. This is far too small for explaining the observed shift of 1.0 mV. In principle it is still possible that this shift is caused by a small instability for example at the interface between Py and CNT. The optimized fabrication process led to cleaner devices with increased stability.

For the observation of an overall negative MR two possible reasons will be discussed in the following. First: A negative MR was also observed in conventional magnetic tunnel junctions with Py as ferromagnetic electrodes. Especially in ref. [97] it was demonstrated that the sign of the TMR signal depends on the tunnel barrier material (e.g. Ta_2O_5 , Al_2O_3) and the bias voltage (in case of a Ta_2O_5 tunnel barrier). The underlying mechanism of these observations is based on evanescent Bloch waves decaying due to different symmetries with different rates in the tunnel barrier (see chapter 2.1 for more details).

The second possibility for observing negative MR is based on the fact that the surface of Py may become oxidized when exposed to air. In ref.[98] a lateral spin valve with a similar structure like for the presented devices but with a silver (Ag) nanowire instead of a CNT was investigated. They imaged the cross section of the interface between the 25 nm thick and 80 nm wide Py strip and the 100 nm wide Ag strip with a scanning transmission electron microscope, see fig.5.6a,b. After exposing the device to air under ambient con-

ditions for 7 days they found a completely oxidized Py interface, see fig.5.6c,d. As introduced in chapter 2.1 the natural oxide of Py exhibits an additional spin filtering effect. However, for observing negative MR, one Py strip has to be completely oxidized while the other one is only partly oxidized. This may tentatively be explained by the different widths since the oxygen has to diffuse from the sides of the strips for affecting the interface. These mechanisms could explain a sign reversal of the MR but not the shifts of the peak at the coercive field of the two Py strips.

Another possibility is discussed in the next section where energy stability diagrams are investigated for different magnetic orientations. There the occurrence of co-tunneling events close to zero bias are taken into account.

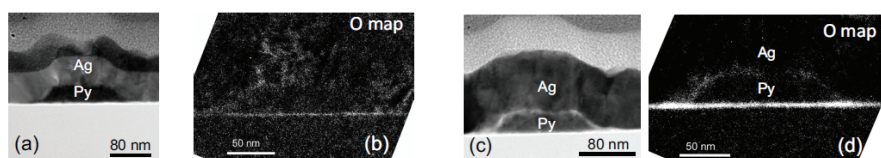


Figure 5.6: a) STEM image of a Py/Ag junction in an as-grown device. b) Corresponding oxygen-map image obtained by energy filtered transmission electron microscopy (EFTEM). c) STEM image of a Py/Ag junction exposed to air for seven days. d) Corresponding oxygen-map. Pictures are taken from [98].

5.2 Stability Diagrams for Different Magnetic Configurations

Further investigations of MR are performed at finite DC bias. In the energy stability diagram shown in fig.5.1c, additional conductance lines inside of the small Coulomb diamonds are visible. Since sequential (first order) tunneling is blocked due to the Coulomb blockade in such a diamond, these lines are due to higher order tunneling processes so-called co-tunneling events [99]. In this case transport takes place via virtual intermediate states within the uncertainty time $\tau \approx \hbar/U$. Depending on the total energy of the QD after the tunnel event one distinguishes between elastic- the energy before and after the tunnel event stays the same and inelastic co-tunneling, where the final QD energy differs from the one before the tunnel event.

A specific effect based on spin-flip co-tunneling events is the Kondo effect [100]. The Kondo effect describes the situation of an increased resistance in metals containing localized magnetic impurities. A QD tuned to a state with an odd number of electrons allows for a treatment of the QD as an artificial magnetic impurity connected to leads. Virtual tunneling events which may effectively flip the spin on the dot lead to the spin-1/2 Kondo effect in QDs [101, 102]. These successive spin-flip processes screen the localized spin on the dot, leading to the formation of an additional conductance channel at zero-bias $V_{SD} = 0$. In the case of a QD connected to ferromagnetic leads, recent experiments [103, 104, 59, 105] found on the one hand that the Kondo resonance peak may become enhanced when the magnetic configuration changes from parallel to antiparallel. On the other hand, the QD becomes spin polarized by a local exchange field, leading to a tunneling induced spin splitting of the Kondo resonance. Especially the enhancement of the Kondo resonance at zero-bias may affect the MR measurement.

Energy stability diagrams for the two magnetic configurations have been measured. The one for the parallel configuration is plotted in fig.5.7a and the one for the antiparallel case in fig.5.7b. Already in these two plots, a change in the conductance is apparent. Pronounced features are indicated by white arrows. For a better visibility of the conductance changes, the difference ΔG of the data is plotted in fig.5.7c. To make sure that the conductance change is really coming from the two magnetic orientations and not from the change of the QD with time, the energy stability diagrams for the two parallel configurations ($\uparrow\uparrow, \downarrow\downarrow$) are subtracted from each other as well and plotted in fig.5.7d. The difference between the two parallel cases $\Delta G = G_{\downarrow\downarrow} - G_{\uparrow\uparrow}$ should be close to zero within the noise level, which is the case. The plot of $\Delta G = G_{\downarrow\downarrow} - G_{\downarrow\uparrow}$ differs significantly. In particular, parts with increased conductance in the antiparallel configuration (indicated by black arrows) leading to negative ΔG

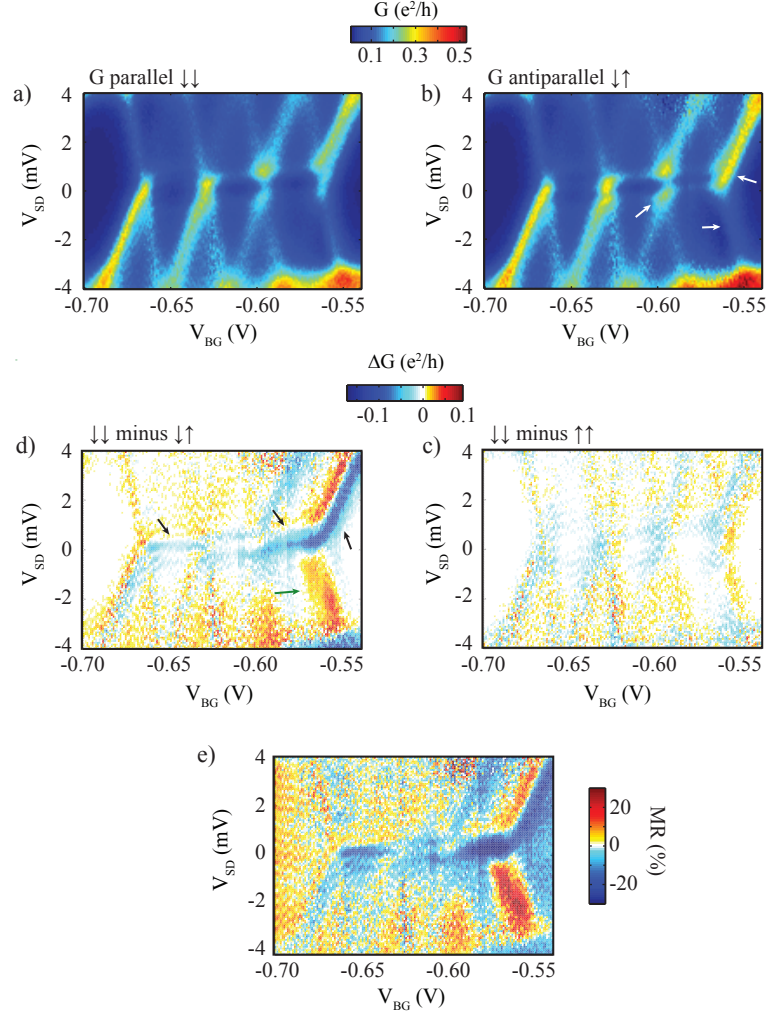


Figure 5.7: Energy stability diagrams for parallel a) and antiparallel b) magnetic configuration. Changes in the conductance are visible, especially at places marked with white arrows. c) The conductance difference $\Delta G = G_{\downarrow\downarrow} - G_{\uparrow\uparrow}$ between parallel and antiparallel configuration is plotted as function of bias V_{SD} and backgate V_{BG} . d) ΔG for the two parallel ($\uparrow\uparrow, \downarrow\downarrow$) magnetic configurations. e) The calculated MR as a function of bias and backgate.

values are visible. Especially the obtained negative values at zero bias are consistent with the MR measurements shown in section 5.1. Increased amplitudes were obtained for the antiparallel configuration leading to an overall negative MR. In addition, parts at finite bias with decreased conductance in the antiparallel configuration (indicated by green arrows) with positive ΔG values can be seen. For completeness the calculated MR plotted in fig.5.7e. Here it has to be mentioned that due to technical reasons the device warmed up between the MR measurements presented in section 5.1

and the measurement of the energy stability diagrams. Due to this, the QD

changed slightly and one has to be careful with comparing these two measurements since the measured conductance peaks are not the same.

The interval of the pronounced MR effect at the large right diamond was recorded with a higher resolution. The energy stability diagram for the antiparallel alignment is plotted in fig.5.8a (the stability diagram for the parallel alignment can be found in appendix C). In fig.5.8b the conductance difference $\Delta G = G_{\downarrow\downarrow} - G_{\downarrow\uparrow}$ between parallel and antiparallel configuration is plotted. In the stability diagram for the parallel configuration a charge rearrangement occurred at $V_{BG} \approx -0.507$ V so that the values for the difference ΔG can only be compared for backgate voltages $V_{BG} < -0.507$ V. Again, parts with negative and positive values are visible.

Especially negative values (indicated by black arrows) occur at

- left slopes of the diamonds at positive bias.
- right slopes of the diamonds at negative bias.
- close to zero-bias within the small diamonds.

In contrast positive values (indicated by green arrows) occur at

- right slopes of the diamond at positive bias.
- left slopes of the diamond at negative bias.

Whenever the conductance difference becomes negative, a positive value can be observed next to it which suggests shifts of the resonances with respect to each other. For excluding shifts, several cross sections are taken (indicated by white dashed lines in fig.5.8a) for the parallel and antiparallel configuration and plotted in fig.5.8 c-f. In all cases the peaks occur at the same values and are shifted neither in bias- nor in backgate-direction.

Cross Section 1

In cross section 1 no significant shifts with the backgate are visible. Peaks marked with black arrows exhibit large amplitudes in the antiparallel configuration. In addition, the two peaks become narrower which may explain the positive values at the slope of these peaks. For the other peaks no significant changes in amplitude or position occur.

Cross Section 2

For the same peaks (black arrows), like in cross section 1, no shifts with the bias are obtained. Sharper peaks are visible with a clear larger amplitude and for the antiparallel alignment.

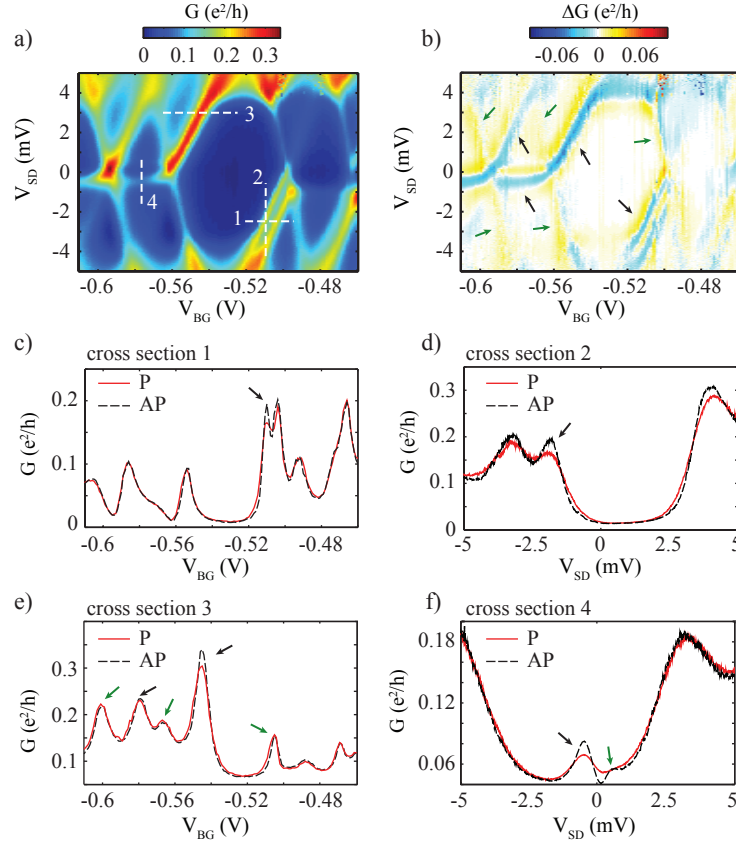


Figure 5.8: a) Energy stability diagram for the antiparallel configuration (for the parallel configuration see appendix C). b) Conductance difference $\Delta G = G_{\downarrow\downarrow} - G_{\downarrow\uparrow}$, parts with positive and negative values are visible. c)-f) Cross sections taken at fixed bias or backgate voltages indicated with white dashed lines in a) for the parallel and antiparallel magnetic configuration. No significant shifts are visible in all cross sections in bias or backgate direction and positive/negative ΔG values are solely caused by the change in amplitude and the shape of the peaks.

Cross Section 3

For all peaks, a change in the amplitude can be obtained. For peaks marked with black arrows, the amplitudes becomes larger in the antiparallel configuration while the amplitude becomes smaller for the one marked with green arrows. This is consistent with the observation made above for left and right slopes of a diamond at positive bias. The conductance changes with different signs when the magnetization is switched from parallel to antiparallel.

Cross Section 4

In this cross section a broad and small peak is visible in the parallel magnetic configuration close to zero bias. In the antiparallel configuration, this peak

changes significantly. The amplitude becomes larger and the peak is much sharper (black arrow). Thus a second small peak marked with a green arrow can be resolved.

All preliminary results presented in this section have been constrained due to the limited lifetime of the device and thus limited number of measurements. Further investigations are proposed. The energy stability diagrams for the same peaks, like those chosen for the gate dependent MR measurements (in chapter 5.1), should be measured for obtaining a direct comparison. Moreover, applying high (several Tesla) magnetic fields or temperatures could help in verifying whether the co-tunnel conductance lines close to zero bias observed in cross section four are related to the Kondo effect or not.

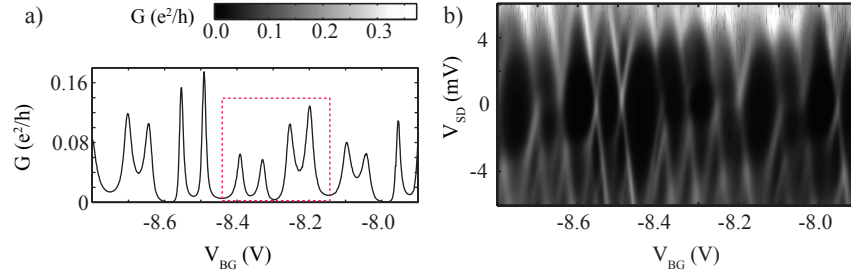


Figure 5.9: a) Backgate V_{BG} sweep of the conductance G at 1.5 K. A clear two-fold periodicity is visible. For the MR measurements four Coulomb peaks are chosen indicated with a red rectangle. b) Energy stability diagram of the QD with a charging energy of $U \sim 4$ meV and a level spacing of $\delta E \sim 3.8$ meV.

5.3 Indications for a MR depended on the Occupation of the QD

A second device has been fabricated independently from the one presented in section 5.1 by using the same fabrication recipe. For this device the same high degree of reproducibility in the MR signal could be observed. The device exhibits a RT resistance of $R \approx 50$ k Ω . The data from the electrical characterization of the QD at low temperature (~ 1.5 K) is plotted in fig.5.9. The four-fold degeneracy of the QD energy levels is slightly visible superimposed by a two-fold periodic conductance pattern. From the energy stability diagram (fig.5.9b) one can extract a charging energy of $U \sim 4$ meV and a level spacing of $\delta E \sim 3.8$ meV. These values comparable to the ones from the QD presented in section 5.1 and fits to a QD of ~ 300 nm size corresponding to the distance between the two Py strips. With the lever arm $\alpha = 0.07$ one obtains an average Coulomb peak width of ~ 1.75 meV.

For the MR measurements four peaks are chosen, indicated by a red dashed rectangle in fig.5.9a. The corresponding conductance G is plotted as a function of backgate voltage V_{BG} and magnetic field B in fig.5.10a for the up (upper panel) and down (lower panel) sweep. At magnetic fields $B \sim \pm 40$ mT and $B \sim \pm 20$ mT conductance changes are visible, in agreement with the coercive fields of a 200 nm and a 400 nm wide Py strip, respectively.

As in the previous section, multiple Lorentzians are fitted to the data for extracting the amplitude, Coulomb peak position and peak width as a function of magnetic field. Due to the comparative high temperature of $T = 1.5$ K the Peaks exhibit no Lorentzian shape (see appendix D)². The fit does not match the data between two Coulomb peaks and therefore the width of the peaks can only be taken as a rough approximation. No clear features, due to

²The temperature of 1.5 K is for this dot corresponds to an intermediate regime and is too low for treating the Coulomb peaks as purely temperature broadened.

electrical instabilities, are visible in the magnetic field dependence of the peak position and width (see appendix D). This section focuses on the magnetic field dependence of the amplitude of each Coulomb peak.

In fig.5.10b The amplitude extracted for each peak is plotted as a function of magnetic field (up and down sweep). For a clearer presentation they are plotted with individual offsets. The labeling with numbers (1-4) corresponds to the labeling in fig.5.10a. Clear step like changes of the amplitude occur at magnetic fields related to the parallel and antiparallel magnetic configuration of the Py strips. A reproducible MR of 3-5% is obtained. Remarkable is the magnetic field dependence of Coulomb peak number 1. The sign of the MR is inverted yielding a positive MR of $\sim 5\%$. In addition, for peak number 2 the MR is superimposed by a single switch. These are first indications that the MR may depend on the chosen Coulomb resonance, as predicted by theories on spin transport in CNT QDs introduced in chapter 2.3. For tracing back the origin of MR in carbon nanotube quantum dots further investigations are proposed. MR measurements in different QD regimes should be made. In particular, MR measurements on Coulomb resonances with strong overlap (conductance in the blockade does not completely decrease to zero) or exhibiting Kondo resonances and on Coulomb resonances well separated from each other. Moreover measurements of MR in QDs weakly/intermediate/strong coupled to the ferromagnetic leads are proposed.

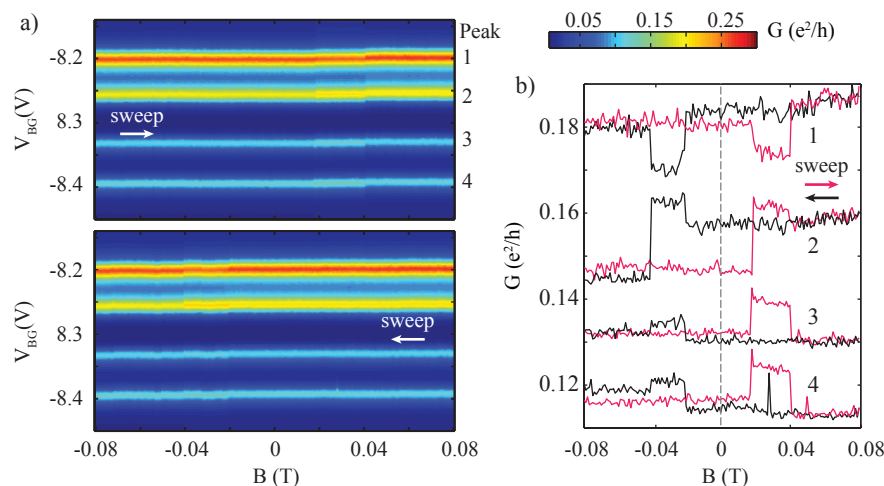


Figure 5.10: a) Conductance G as a function of backgate voltage V_{BG} and magnetic field B . The upper panel shows the up and the lower panel the down sweep. b) Extracted amplitudes of each peak from a multiple Lorentzian fit as a function of magnetic field for up (black line) and down (red line) sweep. For a better reading the four MR measurements are plotted with individual offset.

BEYOND COLLINEAR MR MEASUREMENTS

* * *

A pair of entangled particles - so-called EPR (Einstein-Podolky-Rosen) pair [106] - play a major role in quantum information. A natural source of entangled electron pairs are, for example, Cooper pairs in a s-wave superconductor which occur in a spin-singlet state [107]. Recent research demonstrated the possibility of a controlled spatial splitting of such Cooper pairs in semiconducting nanowires [108] and carbon nanotubes [109, 110]. In a so-called Cooper pair splitter (CPS) a s-wave superconductor is connected to two quantum dots. These QDs enforce the splitting of the Cooper pairs in the two arms of the splitter by Coulomb repulsion. Up to now only charge correlations have been probed and the confirmation of the degree of spin-entanglement is still a challenging task. One approach for the detection of spin entanglement are spin projection measurements which can be realized by using ferromagnets as spin detectors [6].

Ferromagnetic contacts as spin detectors project the spin state to the direction of magnetization of the ferromagnet. The design of long and narrow Py strips contacted to CNTs as discussed in chapter 5 allows only for a parallel and antiparallel magnetic configuration. Such an experiment is not able to distinguish between a two particle product state, in which one spin is up and the other down, and an entangled state. The proof of entanglement necessitates to perform non-collinear spin projection experiments in different directions [6, 111]. For realizing a versatile tunable spin-filter one can replace one rectangular shaped Py strip by a circular shaped Py contact. The circular shape allows for setting the magnetization in any desired direction. The drawback of a single circular shaped ferromagnetic layer is a huge stray-field. For reducing the stray-fields one approach is to replace the single ferromagnetic layer by a circular shaped synthetic antiferromagnet (SAF) [112] stack, for example consisting of alternating Py and ruthenium (Ru) layers. Two Py layers are strongly antiferromagnetically coupled through the thin (7-9 Å) Ru layer by RKKY-exchange interaction¹ (see fig.6.1a). The antiferromagnetic alignment of the two Py layers reduces the stray-fields. The total energy E_{SAF} of a SAF in an external magnetic field H applied with an angle θ to the axis of the aligned Py layers) layer structure is given by

$$E_{SAF} = -\frac{(M_s H t)^2}{2J} \sin^2(\theta), \quad (6.1)$$

¹RKKY stands for Ruderman-Kittel-Kasuya-Yosida

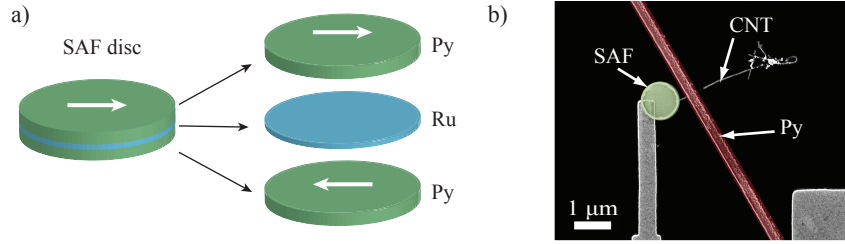


Figure 6.1: a) Schematically illustration of a circular shaped synthetic antiferromagnetic (SAF disc). b) SEM picture of first devices where a carbon nanotube is contacted with a SAF disc and a common Py strip.

where M_s is the saturation magnetization, t the layer thickness and J describes the antiferromagnetic coupling between the two layers. In a large external magnetic field the Py layers nearly align parallel. From eq. 6.1 one sees that for a SAF layer the energy minimizes by rotating its magnetization axis with respect to the external field. When lowering the external field the exchange part becomes dominant and the Py layer end up in an antiparallel magnetized state perpendicular ($\theta = 90^\circ$) to the external field. This is known as a so-called spin flop [113, 114] and is the result of the competition between external magnetic field (trying to align the magnetization in parallel) and exchange coupling (trying to align the magnetizations antiparallel). Contacting for example a carbon nanotube on the one side with a SAF disc and on the other side with a narrow rectangular Py strip, spin transport experiments with tunable spin projections angles are possible.

First test devices have been fabricated in this thesis. The SEM image in fig.6.1b shows the first test device. The sputtered SAF disc consists here in particular of a stack made of $[\text{Py}(5.5 \text{ nm})/\text{Ru}(0.9 \text{ nm})]_4/\text{Ru}(2\text{nm})$. The fabrication of the SAF layer structure has been done in collaboration with the group of Bryan Hickey (School of Physics and Astronomy, Leeds University). The fabricated device fulfilled the criteria of a two-terminal resistance below $1 \text{ M}\Omega$ at RT, but did not work at low temperatures. Since spin transport experiments suffered so far mainly from instabilities the focus of this attempt was first on the development of stable devices. First steps have been done and opens the road for further even more complex experiments which are beyond the scope of this thesis.

CHAPTER 7

SUMMARY

* * *

This thesis presents the investigation of carbon nanotube quantum dots (QD) contacted by ferromagnetic leads. Merging the two topics - quantum dots and spin valves - is a proven challenging task. Electron transport in nanospintronic devices suffers mainly from instabilities in the magneto resistance (MR) and from a low yield $< 5\%$ of electrical contacts to the nanotube. For the ferromagnetic contacts Permalloy (Py, $\text{Ni}_{80}\text{Fe}_{20}$) has been chosen, since a high degree of control over the coercive fields in narrow electron-beam (e-beam) evaporated Py strips was recently demonstrated [66].

In this thesis the origin of instabilities could be attributed to disturbing magnetic particles and flakes appearing during the fabrication process based on either, e-beam evaporated Py or Py deposition by sputtering. For both deposition methods an improved fabrication process has been developed resulting in clean and well defined Py strips with a significantly improved electrical contact yield.

In particular it is demonstrated that close to ideal polymer mask cross sections exhibiting almost no resist residuals could be achieved by processing with the low-density polymer ZEP 520 A. This yields in a significantly reduced occurrence of magnetic particles and improved electrical contact properties for thermally evaporated Py.

An even higher electrical contact yield $\sim 60\%$ was found for Py strips fabricated by sputter deposition. In addition, by improving the directionality of the sputter deposition the occurrence of flakes and rough edges of the sputtered Py strips could be avoided. This allows for the fabrication of sputtered Py strips of the same high quality like e-beam evaporated ones.

It is shown that an enhanced reproducibility in MR measurements for devices with sputtered Py strips can be achieved with the optimized fabrication process. This enabled first MR measurements on carbon nanotube QDs exhibiting a clear four-fold shell-filling conductance pattern.

With a measurement scheme where the conductance is mapped as function of backgate voltage and magnetic field it could be demonstrated that all characteristics of a conductance feature like amplitude, Coulomb peak position and

peak width depend on the magnetic configuration. A specific data analysis allowed even for a separate investigation of the magnetic field dependence for amplitude, position and width.

The observed MR for a package of four peaks is characterized by equal shifts of the Coulomb peaks for the first device. In addition, larger amplitudes for the antiparallel case are obtained. This leads in total to an oscillating $\text{MR}(V_{BG})$ with negative offset which is not fully consistent with common theories for spin transport in such structures. These theories [56, 54] predict a $\text{MR}(V_{BG})$ pattern dependent on the occupation of the QD, which is not seen in the first device.

However, first indications for the predicted dependence are found in a second device. For the second device the different Coulomb peaks show an increased and decreased amplitude for the antiparallel configuration. Because of a higher noise level no conclusions can be derived from the shift behavior.

Preliminary results on energy stability diagrams for the two different magnetic configurations are shown. It is highly recommended to take them into account for interpreting MR values, especially for QDs in an intermediate coupling regime, since additional zero-bias features like the Kondo effect may depend on the magnetic configuration as well.

The time-consuming investigation of energy stability diagrams is limited by electrical instabilities like gate-dependent or temporal charge rearrangements. It would be very interesting to combine the improved fabrication process presented in this thesis with recently demonstrated devices where the QD is electro-statically defined by bottom-gates [50]. These devices exhibit the characteristics of ultraclean QDs even after standard electron beam lithography steps for designing the electrical contacts and thus promising electrical stability.

The new fabrication recipe developed in the frame of this thesis resulting in stable devices with sputtered Py strips paves the way for more elaborated applications. The use of two rectangular narrow Py strips allows only for a parallel and antiparallel magnetic configuration. By replacing one rectangular Py strip by a sputtered synthetic antiferromagnet [112] shaped to a disc enables the possibility for spin projection measurements into any desired direction. First test devices for these non-collinear MR measurements have been fabricated. The development of these advanced versatile spin detectors offers for example the possibility for detecting spin entanglement.

BIBLIOGRAPHY

- [1] S. Datta and B. Das. Electronic analog of the electro-optic modulator. *Appl. Phys. Lett.*, 56:665, 1990.
- [2] D. Loss and D. DiVincenzo. Quantum computation with quantum dots. *Phys. Rev. A*, 57:120, 1998.
- [3] N. Tombros, C. Jozsa, M. Popinciuc, H. T. Jonkman, and B. J. van Wees. Electronic Spin Transport and Spin Precession in Single Graphene Layers at Room Temperature. *Nature*, 448(7153):571–574, Aug 2007.
- [4] S. Sahoo, T Kontos, J. Furer, C. Hoffmann, M. Gräber, A. Cottet, and C. Schönenberger. Electric field control of spin transport. *nature physics*, 1:99, 2005.
- [5] H. T. Man, I. J. Wever, and A. F. Morpurgo. Spin-dependent quantum interference in single-wall carbon nanotubes with ferromagnetic contacts. *Phys. Rev. B*, 73:241401, 2006.
- [6] S. Kawabata. Test of Bell’s Inequality using the Spin Filter Effect in Ferromagnetic Semiconductor Microstructures. *J. Phys. Soc. Jpn.*, 70:1210, 2001.
- [7] Edmund C. Stoner. Collective Electron Ferromagnetism. II. Energy and Specific Heat. *Proc. R. Soc. London A*, 169, 1939.
- [8] N. Mott. The Electrical Conductivity of Transition Metals. *Proc. R. Soc. London A*, 153:699, 1963.
- [9] A. Fert and I. A. Campbell. Two-Current Conduction in Nickel. *PRL*, 21(16):1190–1192, Oct 1968.
- [10] I. A. Campbell, A. Fert, and R. Pomeroy. Evidence for Two Current Conduction in Iron. *PhilMag*, 15(137):977–983, May 1967.
- [11] M. Julliere. Tunneling between ferromagnetic Films. *Phys. Lett. A*, 45:3, 1975.
- [12] J.S. Moodera, L.R. Kinder, T.M. Wong, and R. Meservey. Large Magnetoresistance at Room Temperature in Ferromagnetic Thin Film Tunnel Junctions. *Phys. Rev. Lett.*, 74:3273, 1995.
- [13] T. Miyazaki and N. Tezuka. Giant Magnetic Tunneling Effect in Fe/Al₂O₃/Fe Junction. *J. Magn. Magn. Mater.*, 139:L231, 1995.

- [14] Stuart S. P. Parkin, Christian Kaiser, Alex Panchula, Philip M. Rice, Brian Hughes, Mahesh Samant, and See-Hun Yang. Giant Tunnelling Magnetoresistance at Room Temperature with MgO (100) Tunnel Barriers. *Nature Materials*, 3(12):862–867, Dec 2004.
- [15] S. Yuasa, T. Nagahama, A. Fukushima, Y. Suzuki, and K. Ando. Giant room-temperature magnetoresistance in single-crystal Fe/MgO/Fe magnetic tunnel junctions. *Nature Materials*, 3:868–871, 2004.
- [16] Ph. Mavropoulos, N. Papanikolaou, and P.H. Dederichs. Complex Band Structure and Tunneling through Ferromagnet /Insulator /Ferromagnet Junctions. *Phys. Rev. Lett.*, 85:1088, 2000.
- [17] W.H. Butler, X. G. Zhang, and T.C. Schulthess. Spin-dependent tunneling conductance of Fe/MgO/Fe sandwiches. *Phys. Rev. B*, 63:054416, 2001.
- [18] M. Miao, G.-X. and Muenzenberg and J.S. Moodera. Tunneling path toward spintronics. *Rep. Prog. Phys.*, 74:036501, 2011.
- [19] N. Mueller, W. Eckstein, and W. Heiland. Electron Spin Polarization in Field Emission from EuS-Coated Tungsten Tips. *Phys. Rev. Lett.*, 29:25, 1972.
- [20] J. S. Moodera, X. Hao, G. A. Gibson, and R. Meservy. Electron-Spin Polarization in Tunnel Junctions in Zero Applied Field with Ferromagnetic EuS Barriers. *Phys. Rev. Lett.*, 61:5, 1988.
- [21] M.G. Chapline and S. X. Wang. Room-temperature spin filtering in a $\text{CoFe}_2\text{O}_4/\text{MgAl}_2\text{O}_4/\text{Fe}_3\text{O}_4$ magnetic tunnel barrier. *Phys. Rev. B*, 74:014418, 2006.
- [22] A.V. Ramos, M.-J. Guittet, J.-B. Moussy, C. Deranlot, F. Petroff, and C. Gatel. Room temperature spin filtering in epitaxial cobalt-ferrite tunnel barriers. *Appl. Phys. Lett.*, 91:122107, 2007.
- [23] R. Grau-Crespo, A.Y Al-Baitai, I. Saadoune, and N. H De Lewuw. Vacancy ordering and electronic structure of γ - Fe_2O_3 (maghemite): a theoretical investigation. *J. Phys. Condens. Matter*, 22:255401, 2010.
- [24] M.R. Fitzsimmons, T.J. Silva, and T.M. Crawford. Surface oxidation of Permalloy thin films. *Phys. Rev. B*, 73:014420, 2006.
- [25] G. Binach, P Grünberg, F. Saurenbach, and W. Zinn. Enhanced magnetoresistance in layered magnetic structure with antiferromagnetic interlayer exchange. *Phys. Rev. B*, 39:7, 1989.

- [26] M. N. Baibich, J.M. Broto, A. Fert, F. Nguyen Van Dau, and F. Petroff. Giant Magnetoresistance of (001)Fe/(001)Cr Magnetic Superlattices. *Phys. Rev. Lett.*, 61:21, 1988.
- [27] I. Mertig. Transport properties of dilute alloys. *Rep. Prog. Phys.*, 62:237, 1999.
- [28] L. Piraux, J. M. George, J. F. Despres, C. Leroy, R. Legras, K. Ounadjela, and A. Fert. Giant magnetoresistance in magnetic multilayered nanowires. *Appl. Phys. Lett.*, 65:2484, 1994.
- [29] A. Fert and L. Piraux. Magnetic nanowires. *J. Magn. Magn. Mater.*, 200:338, 1999.
- [30] Mark Johnson and R. H. Silsbee. Coupling of Electronic Charge and Spin at a Ferromagnetic-Paramagnetic Metal Interface. *PRB*, 37(10):5312–5325, Apr 1988.
- [31] P. C. van Son, H. van Kempen, and P. Wyder. Boundary Resistance of the Ferromagnetic-Nonferromagnetic Metal Interface. *PRL*, 58(21):2271–2273, May 1987.
- [32] G. Schmidt, D. Ferrand, L. W. Molenkamp, A. T. Filip, and B. J. van Wees. Fundamental Obstacle for Electrical Spin Injection from a Ferromagnetic Metal into a Diffusive Semiconductor. *PRB*, 62(8):R4790–R4793, Aug 2000.
- [33] A. Fert and H. Jaffrès. Conditions for Efficient Spin Injection from a Ferromagnetic Metal into a Semiconductor. *PRB*, 64(18):184420, Oct 2001.
- [34] E. I. Rashba. Theory of Electrical Spin Injection: Tunnel Contacts as a Solution of the Conductivity Mismatch Problem. *PRB*, 62(24):R16267–R16270, Dec 2000.
- [35] Christian Ertler, Sergej Konschuh, Martin Gmitra, and Jaroslav Fabian. Electron Spin Relaxation in Graphene: The Role of the Substrate. *PRB*, 80(4):041405, Jul 2009.
- [36] K. S. Novoselov, A. K. Geim, S. V. Morozov, D. Jiang, Y. Zhang, S. V. Dubonos, I. V. Grigorieva, and A. A. Firsov. Electric Field Effect in Atomically Thin Carbon Films. *Science*, 306(5696):666–669, Oct 2004.
- [37] A. K. Geim. Graphene: Status and Prospects. *Science*, 324:1530, 2009.
- [38] A. H. Castro Neto, F. Guinea, N. M. R. Peres, K. S. Novoselov, and A. K. Geim. The Electronic Properties of Graphene. *RMP*, 81(1):109–162, Jan 2009.

- [39] J. Schindele. *Observation of Cooper Pair Splitting and Andreev Bound States in Carbon Nanotubes*. PhD thesis, University of Basel, 2014.
- [40] P. R. Wallace. The Band Theory of Graphite. *PR*, 71(9):622–634, May 1947.
- [41] S. G. Lemay, J. W. Janssen, M. van den Hout, M. Mooij, M. J. Bronikowski, P. A. Willis, R. E. Smalley, L. P. Kouwenhoven, and C. Dekker. Two-dimensional imaging of electronic wavefunctions in carbon nanotubes. *Nature*, 412:617, 2001.
- [42] J.C. Charlier, X. Blase, and S. Roche. Electronic and transport properties of nanotubes. *Rev. Mod. Phys.*, 79:2, 2007.
- [43] H. Aurich. *Carbon Nanotube Spin-Valve with Optimized Ferromagnetic Contacts*. PhD thesis, University of Basel, 2012.
- [44] J. Svensson and E.B. Campbell. Schottky barriers in carbon nanotube-metal contacts. *J. Appl. Phys.*, 110:111101, 2011.
- [45] S. Ilani and P. L. McEuen. Electron Transport in Carbon Nanotubes. *Annu. Rev. Condens. Matter Phys.*, 1:1, 2010.
- [46] D. L. Klein, P. L. McEuen, J.E. Bowen Katari, R. Roth, and A. P. Alivisatos. An approach to electrical studies of single nanocrystals. *Appl. Phys. Lett.*, 86:2574, 1996.
- [47] L. P. Kouwenhoven, D. G. Austing, and S. Tarucha. Few-electron quantum dots. *Rep. Prog. Phys.*, 64:701, 2001.
- [48] M. T. Björg, C. Thelander, A.E. Hansen, L. E. Jensen, M. W. Larsson, L. Reine Wallenberg, and L. Samuelson. Few-Electron Quantum Dots in Nanowires. *Nano Letters*, 4:9, 2004.
- [49] C. Dekker. Carbon Nanotubes as Molecular Quantum Wires. *Physics Today*, 52:22, 1999.
- [50] M. Jung, J. Schindel, S. Nau, M. Weiss, A. Baumgartner, and C. Schönenberger. Ultraclean Single, Double and Triple Carbon Nanotube Quantum Dots with Recessed Re Bottom Gates. *Nano*, 13:9, 2013.
- [51] S. Heinze, J. Tersoff, R. Martel, V Derycke, J Appenzeller, and Ph Avouris. Carbon Nanotubes as Schottky Barrier Transistors. *Phys. Rev. Lett.*, 89:106801, 2002.
- [52] T. Ihn. *Semiconductor Nanostructures: Quantum States and Electronic Transport*. Oxford University Press, 2010.

- [53] A. Cottet, T Kontos, W. Belzig, C. Schönenberger, and C Bruder. Controlling spin in an electronic interferometer with spin-active interfaces. *Europhysics Letters*, 74:320, 2006.
- [54] S. Koller, M. Grifoni, and J. Paaske. Sources of negative tunneling magnetoresistance in multilevel quantum dots with ferromagnetic contacts. *Phys. Rev. B*, 85:045313, 2012.
- [55] Ya. M. Blanter and M. Büttiker. Shot noise in mesoscopic conductors. *Phys. Rep.*, 336:1, 2000.
- [56] A. Cottet and M.-S. Choi. Magnetoresistance of a quantum dot with spin-active interfaces. *Phys. Rev. B*, 74:235316, 2006.
- [57] Y. Meir and P. A. Wingreen, N. S. and Lee. Transport through a Strongly Interacting Electron System: Theory of Periodic Conductance Oscillations. *Phys. Rev. Lett.*, 66:23, 1991.
- [58] J. R. Hauptmann, J Paaske, and P. E Lindelof. Electric-field-controlled spin reversal in a quantum dot with ferromagnetic contacts. *Nature Physics*, 4:373, 2008.
- [59] L Hofstetter, A. Geresdi, M. Aagesen, J. Nygard, C. Schönenberger, and S. Csonka. Ferromagnetic proximity effect in a ferromagnet-quantum-dot-superconductor device. *Phys. Rev. Lett.*, 104:246804, 2010.
- [60] J. Martinek, Y. Utsumi, H. Imamura, J. barnas, S. Maekawa, J. König, and G. Schön. Kondo Effect in Quantum Dots Coupled to Ferromagnetic Leads. *Phys. Rev. Lett.*, 91:127203, 2003.
- [61] J. Martinek, M. Sindel, L. Borda, J. Barnas, R. Bulla, J. König, G. Schön, S. Maekawa, and J. von Delft. Gate-controlled spin splitting in quantum dots with ferromagnetic leads in the Kondo regime. *Phys. Rev. B*, 72:121302, 2005.
- [62] H. Schoeller and G. Schön. Mesoscopic quantum transport: Resonant tunneling in the presence of strong Coulomb interaction. *Phys. Rev. B*, 50:18436, 1994.
- [63] J. Furer. *Growth of Single-Wall Carbon Nanotubes by Chemical Vapor Deposition for Electrical Devices*. PhD thesis, University of Basel, 2006.
- [64] X. Li, X. Tu, S. Zaric, K. Welsher, W. S. Seo, W. Zhao, and H. Dai. Selective synthesis combined with chemical separation of single-walled carbon nanotube for chirality selection. *J. Am. Chem. Soc.*, 129:15770, 2007.

- [65] W. Kim, A. Javey, R. Tu, J. Cao, Q. Wang, and H. Dai. Electrical contacts to carbon nanotubes down to 1nm in diameter. *Appl. Phys. Lett.*, 87:173101, 2005.
- [66] H. Aurich, A. Baumgartner, F. Freitag, A. Eichler, J. Trbovic, and C. Schönenberger. Permalloy-based carbon nanotube spin-valve. *Appl. Phys. Lett.*, 97:153116, 2010.
- [67] H. Bluhm and K. A. Moler. Dissipative cryogenic filters with zero dc resistance. *Review of Scientific Instruments*, 79:014703, 2008.
- [68] D. Steininger, A. K. Hüttel, M. Ziola, M. Kiessling, M. Sperl, G. bayreuther, and Ch. Strunk. Transversal magnetic anisotropy in nanoscale PdNi-strips. *Journal of Applied Physics*, 113:034303, 2013.
- [69] D. Preusche, S. Schidmeier, E. Pallecchi, Ch. Dietrich, A. K. Hüttel, J. Zweck, and C. Strunk. Characterization of ferromagnetic contacts to carbon nanotubes. *Journal of Applied Physics*, 106:084314, 2009.
- [70] A. Jensen, J.R. Hauptmann, J. Nygard, and P. E Lindelof. Magnetoresistance in ferriferromagnetic contacted single-wall carbon nanotubes. *Phys. Rev. B*, 72:035419, 2005.
- [71] H. Yang, M. E. Itkis, R. Moriya, C. Rettner, J.-S. Jeong, D. S. Pickard, R. C. Haddon, and S. P. Parkin. Nanotubes transport in single-walled carbon nanotube networks. *Phys. Rev. B*, 85:052401, 2012.
- [72] Mark Elkin. *Ferromagnetically Contacted Carbon Nanotube Quantum Dots*. PhD thesis, University of Leeds, 2012.
- [73] S. van der Molen, N. Tombros, and B. J. van Wees. Magneto-Coulomb effect in spin-valve devices. *Phys. Rev. B*, 73:220406, 2006.
- [74] D. H. Cobden and J. Nygard. Shell Filling in Closed Single-Wall Carbon Nanotube Quantum Dots. *Phys. Rev. Lett.*, 89:046803, 2002.
- [75] T. Brintlinger, Y. F. Chen, E. Dürkop, T. Cobas, M. S. Fuhrer, J. D. Barry, and J. Melngailis. Rapid imaging of nanotubes in insulating substrates. *Appl.*, 81:2454, 2002.
- [76] D. S. Macintyre, O. Ignatova, S. Thoms, and I. G. Thayne. Resist residues and transistor gate fabrication. *J. Vac. Sci. Technol. B*, 27(6):2597, 2006.
- [77] I. Maximov, A. A. Zakharov, T. Holmqvist, L. Montelius, and I. Lindau. Investigation of polymethylmethacrylate resist residues using photoelectron microscopy. *J. Vac. Sci. Technol. B*, 20(3):1139, 2002.

- [78] T. Nishida, M. Notomi, R. Iga, and T. Tamamura. Quantum Wire Fabrication by E-beam Lithography Using High-Resolution and High-Sensitivity E-Beam Resist ZEP-520. *Jpn. J. Appl. Phys.*, 31:4508, 1992.
- [79] B. Dlubak, P. Seneor, A. Anane, C. Barraud, C. Deranlot, d. Deneuve, B. Servet, R. Mattana, F. Petroff, and A. Fert. Are Al_2O_3 and MgO tunnel barriers suitable for spin injection in graphene? *Appl. Phys. Lett.*, 97:092502, 2010.
- [80] E. W. Pugh, E. L. Boyd, and J. F. Freedmann. Angle-of-Incidence Anisotropy in Evaporated Nickel-Iron Films. *IBM Journal*, page 163, 1960.
- [81] M. Liang, W. Bockrath and H. Park. Shell filling and exchange coupling in metallic single-walled carbon nanotubes. *Phys. Rev. Lett.*, 88:126801, 2002.
- [82] P. Jarillo-Herrero, J. Kong, HS. van der Zant, C. Dekker, L. P. Kouwenhoven, and S. De Franceschi. Electronic transport spectroscopy of carbon nanotubes in a magnetic field. *Phys. Rev. Lett.*, 94:156802, 2005.
- [83] A. Makarovski, I. An, J. Liu, and G. Finkelstein. Persistent orbital degeneracy in carbon nanotubes. *Phys. Rev. B*, 74:155431, 2006.
- [84] S. Moriyama, M. Fuse, T. Suzuki, Y. Aoyagi, and K. Ishibashi. Four-electron shell structure and an interacting two-electron system in carbon nanotube quantum dots. *Phys. Rev. Lett.*, 94:186806, 2005.
- [85] Y. Oreg, K. Byczuk, and B. Halperin. Spin configurations of a carbon nanotube in a nonuniform external potential. *Phys. Rev. Lett.*, 85:365, 2000.
- [86] F. Kuemmeth, S. Ilani, D. Ralph, and P. McEuen. Coupling of spin and orbital motion of electron in carbon nanotubes. *Nature*, 452:448, 2008.
- [87] T. S. Jespersen, K. Grove-Rasmussen, J. Paaske, K. Muraki, T. Fujisawa, J. Nygard, and K. Flensberg. Gate-dependent spin-orbit coupling in multielectron carbon nanotubes. *Nature Physics*, 7:348, 2011.
- [88] W. Thomson. On the electro-dynamic qualities of metals: Effects of the magnetization on the electric conductivity of nickel and iron. *Proceedings of the Royal Society of London*, 8:546, 1856.
- [89] I. A. Campbell and A. Fert. *Transport Properties of Ferromagnets*. Ferromagnetic Materials, Vol. 3, 1982.
- [90] S. Craig and Harding G. L. Effects of argon pressure and substrate temperature on the structure and properties of sputtered copper films. *J. Vac. Sci. Technol.*, 19:205, 1981.

- [91] H. J. Leamy and A. G. Dirks. Microstructure and magnetism in amorphous rareearth-transitionmetal thin films. ii. Magnetic anisotropy. *J. Appl. Phys.*, 50:2871, 79.
- [92] O. P. Karpenko, J.C. Bilello, and S. M. Yalisove. Growth anisotropy and self-shadowing: A model for the development of in-plane texture during polycrystalline thin film growth. *J. Appl. Phys.*, 82:1397, 1979.
- [93] M. M. Henneberg, D. J. Pocker, and M. A. Parker. Effects of rotation and ion incidence angle on sputter depth resolution in thin film of nife/ta. *Surface and Interface Analysis*, 19:55, 1992.
- [94] H. Shimada, K. Ono, and Y. Ootuka. Magneto-Coulomb Oscillation in Ferromagnetic Single Electron Transistors. *J. Phys. Soc. Jpn*, 67:1359, 1998.
- [95] F. A. Zwaneburg, D. W. van der mast, H. B. Heersche, and L. P. Kouwenhoven. Electric Field Control of Magnetoresistance in InP Nanowires with Ferromagnetic Contacts. *Nano Letters*, 9:2704, 2009.
- [96] J. P. Nibarger, R. Lopusnik, Z. Celinski, and T. J. Silva. Variation of magnetization and the Landé g factor with thickness in Ni-Fe films. *Appl. Phys. Lett.*, 7:93, 2003.
- [97] M. Sharma, S. X. Wang, and J. H. Nickel. Inversion of Spin Polarization and Tunneling Magnetoresistance in Spin-Dependent Tunneling Junctions. *Phys. Rev. Lett.*, 82:616, 1999.
- [98] G. Mihajlovic, D. K Schreiber, Y. Liu, J. E. Pearson, S. D. Bader, A. K. Petford-Long, and A. Hoffmann. Enhanced spin signals due to native oxide formation in Ni₈₀Fe₂₀/Ag lateral spin valves. *Appl. Phys. Lett.*, 97:112502, 2010.
- [99] S. De Franceschi, S. Sasaki, J. M. Elzermann, W. G. van der Wiel, S. Tarucha, and L. P. Kouwenhoven. Electron Cotunneling in a Semiconductor Quantum Dot. *Phys. Rev. Lett.*, 86:878, 2001.
- [100] J. Kondo. Resistance Minimum in Dilute Magnetic Alloys. *Progress of Theoretical Physics*, 32:37, 1964.
- [101] D Goldhaber-Gordon, H. Shtrikman, D. Abusch-Magder, U. Meirav, and M. A. Kastner. Kondo effect in a single-electron transistor. *Nature*, 391:156, 1998.
- [102] S. M. Cronenwett, T. H. Oosterkamp, and L. P. Kouwenhoven. A Tunable Kondo Effect in Quantum Dots. *Science*, 281:540, 1998.

- [103] J. R. Hauptmann, J. Paaske, and P. E Lindelof. Electric-field-controlled spin reversal in a quantum dot with ferromagnetic contacts. *Nature Physics*, 4:373, 2008.
- [104] A. N. Pasupathy, R. C. Bialczak, J. Martinek, J. E. Grose, L. A. K. Donev, P. L. McEuen, and D. C. Ralph. The Kondo Effect in the Presence of Ferromagnetism. *Science*, 306:86, 2004.
- [105] M. Gaas, A. K. Hüttel, K. Kang, I. Wymann, J. von Delft, and C. Strunk. Universality of the Kondo Effect in Quantum Dots with Ferromagnetic Leads. *Phys. Rev. Lett.*, 107:176808, 2011.
- [106] A. Einstein, B. Podolsky, and N. Rosen. Can Quantum-Mechanical Descripton of Physical Reality Be Considered Complete. *Phys. Rev.*, 47:777, 1935.
- [107] J. Bardeen, L. N. Cooper, and J. R. Schrieffer. Theory of Superconductivity. *Phys. Rev.*, 108:1175, 1957.
- [108] L Hofstetter, S. Csonka, J. Nygard, and C. Schönenberger. Cooper pair splitter realized in a two quantum-dot Y-junction. *Nature*, 461:961, 2009.
- [109] L. G. Herrmann, F. Portier, A. Roche, P. Levy Yeyati, T. Kontos, and C. Strunk. Carbon Nanotube as Cooper-Pair Beam Splitters. *Phys. Rev. Lett.*, 104:026801, 2010.
- [110] J. Schindele, A. Baumgartner, and C. Schönenberger. Near-Unity Cooper Pair Splitting Efficiency. *Phys. Rev. Lett.*, 109:157002, 2012.
- [111] J. S. Bell. On the einstein podolsky rosen paradox. *Physics*, 1:195, 1964.
- [112] S. S. P. Parkin and D. Mauri. Spin engineering: Direct determination of the Rudermann-Kittel-Kasuya-Yosida far-field range function in ruthenium. *Phys. Rev. B*, 44:7131, 1991.
- [113] H. C. Tong, C. Qian, L. Miloslavsky, S. Funada, X. Shi, F. Liu, and S. Dey. The spin flop of synthetic antiferromagnetic films. *J. Appl. Phys.*, 87:5055, 2000.
- [114] J. G. Zhu. Spin Valve and Dual Spin Valve Heads with Synthetic Antiferromagnets. *IEEE Trans. Magn.*, 35:655, 1999.

APPENDIX A

FABRICATION RECIPES

* * *

Wafer Cleaning

- Cutting highly doped Si wafer into $1 \times 1 \text{ cm}^2$ small pieces.
 - Dopant: p, Boron
 - Resistivity: 0.003 - 0.005 Ωm
 - Capping layer: 400 nm thermally grown SiO_2
- 15 min. sonication in acetone.
- 15 min. sonication in isopropanol (IPA), blow dry.
- 1 h UV-ozon cleaning (Model: 42-220, Jelight Company, USA).

CVD Catalyst

- Sonication of the stock solutions for 2 h.
 - 30 mg Al_2O_3 dissolved in 20 ml IPA
 - 93 mg $\text{Fe}(\text{NO}_3)_3 \cdot 9\text{H}_2\text{O}$ dissolved in 20 ml IPA
 - 48 mg $\text{RuCl}_3 \cdot \text{H}_2\text{O}$ dissolved in 20 ml IPA
- 0.5 ml of each solution is mixed + 38 ml IPA.

This Ru-solution is produced in-house for stock and this fabrication step has only to be done from time to time.

CVD Growth

- 1.5 h sonication of the Ru-solution in high-power sonicator to break up the catalyst clusters.
 - Power: 100
 - Pulse duration: 0.5 s
 - Pause: 0.5 s
- 1-2 droplets of Ru-solution on cleaned, already spinning wafer (4000 rpm).

- Placing the wafer in the quartz tube of the CVD reactor.
- Heating up the furnace under Ar flow (104 l/h = 1500 sccm) to 850° C.
- Replacing Ar, flow with CH₄ (44.7 l/h = 1000 sccm) and H₂ (8 l/h = 500 sccm) for 10 min.
- Replacing the CH₄ flow with Ar flow and switching off the furnace.
- At T < 550° C switching of the H₂ flow.
- At T < 250° C switching of the Ar gas flow and taking out the wafer.

It is recommended to grow 3-4 wafers in parallel since the amount and density of CNTs can vary from wafer to wafer.

E-Beam Lithography

During the duration of this Phd project several resist systems are tried out. Only the most suitable recipe for the fabrication of CNT spin valves is listed in the following

- Spinning of 300 nm ZEP (520A, Zeon Cooperation) diluted in Anisol.
 - Ramp: 4 s
 - Speed: 4000 rpm
 - Time: 40 s
- Baking on hot plate at 180° for 3 min.
- Exposure with standard e-beam lithography (Zeiss Supra 40).
 - Acceleration voltage: 10 kV
 - Area dose: 34 $\mu\text{C}/\text{cm}^2$
 - Working distance: 9 mm
 - Aperture: 10 μ for the small write field (100 μm) and 120 μm for the coarse write field (2000 μm)
- Development
 - 60 s in n-Amylacetate
 - 10 s in 9:1 solution of MIBKA and IPA to stop the development
 - Rinsing in pure IPA, blow dry

Metalization

Recipes for the metalization depend strongly on material and system (three different systems have been used). Therefore detailed parameters are not listed. Before the Pd deposition on top of Py an Ar plasma etching for 2 min is done to remove possible oxides on the surface

Lift-Off

- 15 min. in n-methyl-2-pyrrolidone (NMP) at 70°.
- 30 min. in acetone at 50°.

APPENDIX B

ADDITIONAL DATA TO CHAPTER 5.1

* * *

This appendix shows the magnetic field dependence of the amplitude, peak position and peak width for all the other peaks. In figB.1 the conductance is plotted (black dashed line) as a function of backgate voltage for the antiparallel magnetic configuration. In addition, the fit of multiple Lorentzians is shown, the sum as orange line and each single Lorentzian as green lines. For peak #1, #2, #4 the amplitude, peak position and peak width are extracted as a function of magnetic field and plotted for up and down sweeps in fig.B.2-fig.B.4, respectively.

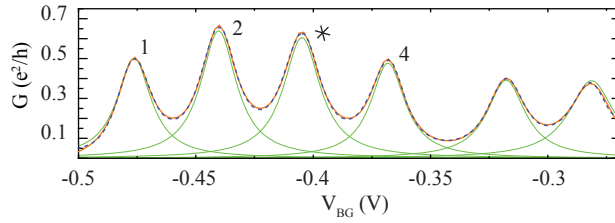


Figure B.1: Conductance as function of backgate voltage for the antiparallel magnetic configuration. The orange line represents the sum of 6 fitted Lorentzians. Each single Lorentzian is plotted as additional green lines.

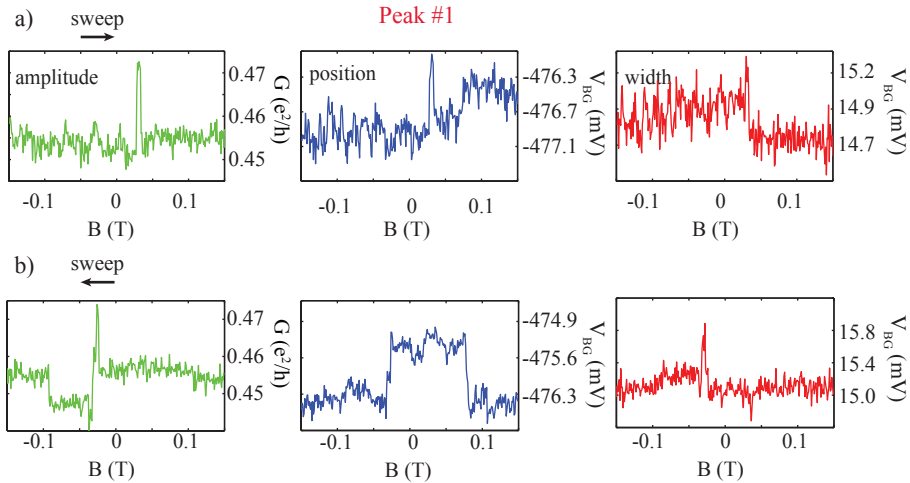


Figure B.2: Magnetic field dependence of the amplitude, peak position and width of Peak 1 for up a) and down b) sweep.

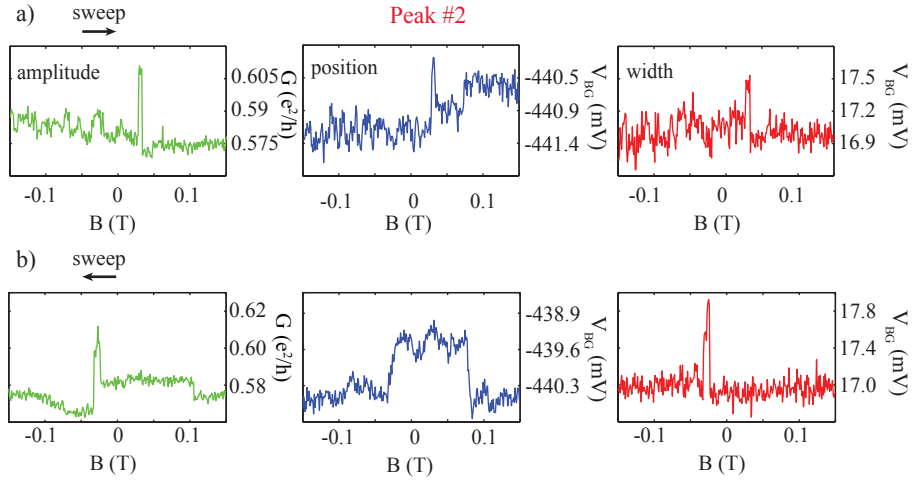


Figure B.3: Magnetic field dependence of the amplitude, peak position and width of Peak 1 for up a) and down b) sweep.

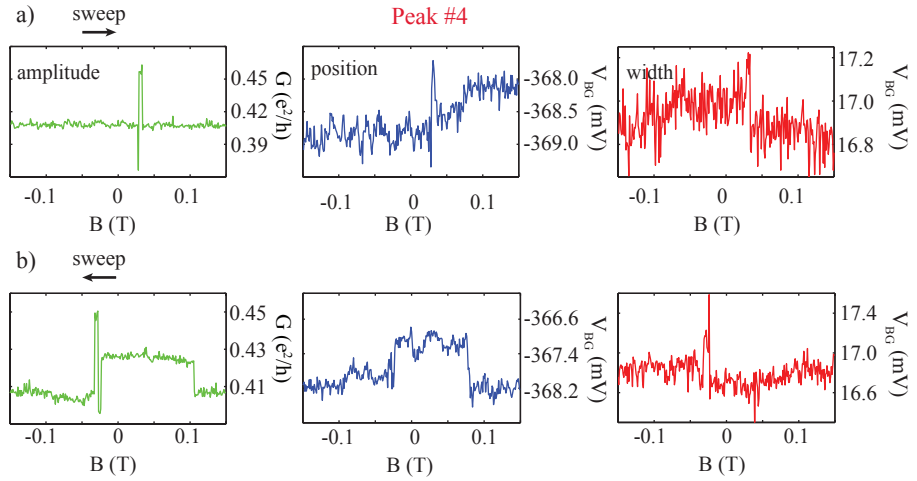


Figure B.4: Magnetic field dependence of the amplitude, peak position and width of Peak 1 for up a) and down b) sweep.

In all cases the same qualitatively behavior could be observed, especially all peaks shift about the same value within experimental errors.

APPENDIX C

ADDITIONAL DATA TO CHAPTER 5.2

* * *

For completeness the energy stability diagram for the parallel magnetic configuration is plotted in fig.C.1a and for a better comparison the stability diagram for the antiparallel case is plotted in fig.C.1b. For the parallel stability diagram small gate-jumps are observed at backgate voltages indicated as white arrows.

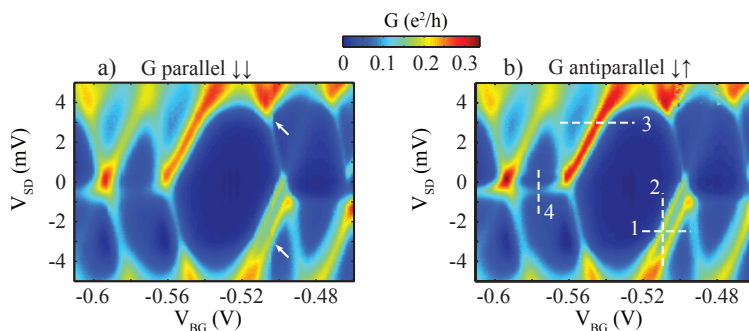


Figure C.1: Energy stability diagrams for the parallel a) and antiparallel b) magnetic configuration.

APPENDIX D

ADDITIONAL DATA TO CHAPTER 5.3

* * *

This appendix contains additional data to chapter 5.3. In fig.D.1a the conductance G of the QD for the parallel magnetic configuration is plotted as function of backgate voltage V_{BG} . In addition the fit of multiple Lorentzians (red line) and the corresponding single Lorentzians (green line) are plotted. As an example the extracted peak position and peak width are plotted for one peak as a function of magnetic field in fig.D.1b and fig.D.1c respectively. No significant features are visible.

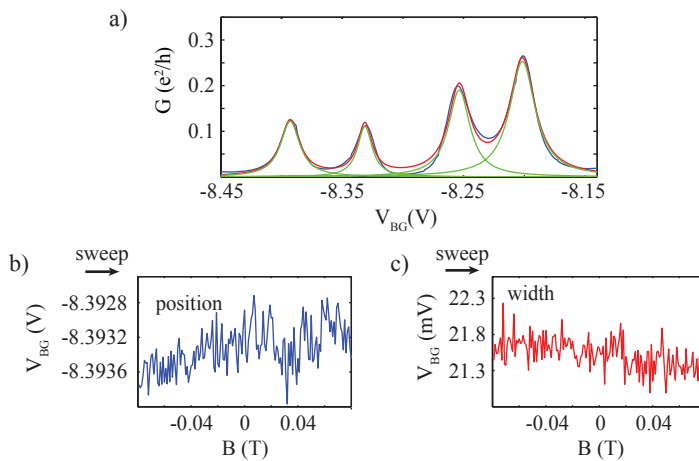


Figure D.1: a) Conductance versus backgate voltage. The fit on the data of multiple Lorentzians is plotted in addition (red line: sum, green line: single peaks).

CURRICULUM VITAE

* * *

Julia Samm

Born 26 October 1980 in Aachen (Germany)

Education

- | | |
|-----------------|--|
| 06/2000 | Abitur (High School Diploma); Städtisches Gymnasium Eschweiler |
| 10/2000-09/2001 | Studies of math at the University of Aachen |
| 10/2001-11/2009 | Studies of physics at the University of Aachen |
| 11/2009 | Diploma in physics at University of Aachen Diploma thesis in the group of Prof. G. Güntherodth: "Investigation of Spin Transport and Spin Precession in Graphen spin-valves" |
| 2010–2014 | PhD in experimental Physics at the University of Basel PhD thesis in the group of Prof. C. Schönemberger: "Investigation of Carbon Nanotube Quantum Dots Connected to Ferromagnetic Leads" |

Positions

- | | |
|-----------------|---|
| 11/2007-08/2009 | Teaching assistant at the <i>Physikalisches Institut</i> Aachen |
| 12/2009–03/2010 | Research assistant at the <i>Physikalisches Institut</i> Aachen |
| 2010–2014 | Teaching assistant for physics at the University of Basel |

PUBLICATIONS

* * *

Publications

- *Observation of long spin-relaxation times in bilayer graphene at room temperature,*
T.Y. Yang, J.Balkrishnan, F. Volmer, A. Avsar, M. Jaiswal, J. Sann, S.R. Ali, A. Pachoud, M. Zheng, M. Popinciuc, G. Güntherodt, B. Beschoten, B. Özyilmaz
Physical Review Letter, **107**, 047206 (2011)
- *Optimized fabrication and characterization of carbon nanotube spin valves,*
J. Sann, J. Gramich, A. Baumgartner, H. Aurich, M. Weiss, C. Schönenberger
Journal of Applied Physics, **115**, 174309 (2014)

Talks

- *Spin transport in nano-structures,*
German Conference of Women in Physics (Deutsche Physikerinnen Tagung).
November 2010
- *Spin transport in carbon based nanoelectronic devices*
Seminar talk in the Group of Prof. Charles Marcus at Harvards Center for Nanoscale Systems, USA, April 2010

Poster Contributions

- *Permalloy contacts for carbon-based spintronics,*
J. Sann, H. Aurich, J. Rebling, P. Rickhaus, M. Elkin, B. J. Hickes, M. Weiss, A. Baumgartner, Schönenberger
Joint European Magnetic Symposium (JEMS), Parma, Italy, 2012
- *Permalloy contacts for carbon-based spintronics,*
J. Sann, J. Gramich, M. Weiss, A. Baumgartner, Schönenberger
Next nano Stars event, Basel, Switzerland, 2013

- *Permalloy contacts for carbon-based spintronics*,
J. Samm, J. Gramich, M. Weiss, A. Baumgartner, C. Schönenberger
Frontiers in Quantum Engineered Devices Conference, Obergurgel Austria, 2013
- *Permalloy contacts for carbon-based spintronics*,
J. Samm, J. Gramich, M. Weiss, A. Baumgartner, C. Schönenberger
Swiss Nano Convention, Basel, Switzerland, 2013
- *Fabrication and characterization of carbon-based spintronic devices*
J. Samm J. Gramich, M. Weiss, A. Baumgartner, C. Schönenberger
International Winterschool on Electronic Properties of Novel Material,
Kirchberg Austria, March 2014

Awards

- Poster prize, Conference: Joint European Magnetic Symposium (JEMS),
Parma, Italy, 2012